Numerical modeling of electromagnetic coupling effects for phase correction in borehole EIT measurements

Dissertation

zur

Erlangung des Doktorgrades (Dr. rer. nat.)

der

Mathematisch-Naturwissenschaftlichen Fakultät

der

Rheinischen Friedrich-Wilhelms-Universität Bonn

vorgelegt von

Yulong Zhao

aus

Xinxiang, China

Bonn 2016

Angefertigt mit Genehmigung der Mathematisch-Naturwissenschaftlichen Fakultät
der Rheinischen Friedrich-Wilhelms-Universität Bonn

1. Gutachter: Prof. Dr. Andreas Kemna
2. Gutachter: Prof. Dr. Johan Alexander Huisman
Tag der Promotion: 13.01.2017
Erscheinungsjahr: 2017

IN DER DISSERTATION EINGEBUNDEN:

Zusammenfassung

Abstract

Spectral Electrical Impedance Tomography (EIT) allows obtaining images of the complex electrical conductivity for a broad frequency range (mHz to kHz). It has recently received increased interest in the field of near-surface geophysics and hydrogeophysics because of the relationships between complex electrical properties and hydrogeological and biogeochemical properties and processes observed in the laboratory with Spectral Induced Polarization (SIP). However, these laboratory results have also indicated that a high measurement accuracy is required for the phase angle of the complex electrical conductivity because many soils and sediments are only weakly polarizable and show small phase angles between 1 and 20 mrad only. It is challenging to achieve this phase accuracy in a broad frequency range for EIT measurements in the field. In the case of borehole EIT measurements, electrode chains with a length of 10 meters or more are typically used. This may lead to undesired inductive coupling between the electric wires used for current injection and potential measurement and capacitive coupling between the electrically conductive cable shielding and the soil. Depending on the measured transfer impedances, both coupling effects can cause large phase errors that have typically limited the frequency bandwidth of field EIT measurements to the mHz to Hz range. So far, potentially useful information from the high frequency range (up to kHz) could not be reliably measured in the field using EIT.

Within this context, the aim of this PhD thesis was to develop correction procedures for inductive and capacitive coupling effects in borehole EIT measurements to enable more accurate phase measurements in the kHz frequency range. Throughout the thesis, an enhanced field EIT measurement system with 40 channels was used. In addition, custom-made electrode chains with eight electrode modules with a spacing of 1 m and a cable length of 25 m were initially used to develop the correction methods. Each electrode module of the electrode chain was equipped with a brass ring electrode, an integrated amplifier for potential measurement, and an integrated switch for current injection. In general, borehole EIT measurements can be divided into two different cases according to the electrode arrangement. In the first case, EIT

measurements are performed in a single borehole. Here, a correction procedure was developed to determine the inductive coupling between the wires (i.e. the mutual inductance) in a single electrode chain using a calibration measurement. In this calibration measurement, all electrodes of the chain were short-circuited and the shield was used as the return line, so that the pure mutual inductance between the wire pairs could be measured indirectly. In the second case, EIT measurements are performed in two boreholes. Here, a correction procedure was developed that combines calibration measurements to determine the mutual inductance between wires close to each other (i.e. inside one electrode chain) with model-based estimates of the mutual inductances between wires far from each other (i.e. in two different electrode chains). In addition, a pole-pole matrix formulation was developed to efficiently describe mutual inductances inside and between electrode chains. To separate parasitic inductances associated with the grounding wire and the wire used for short-circuiting the electrodes in the calibration measurement from the mutual inductance associated with the electrode chains, a second calibration measurement with both electrode chains was used. This second calibration was required because these parasitic inductances cannot be compensated in the calculation of the mutual inductance when two electrode chains are used. A correction procedure was also developed to remove the effects of capacitive coupling. Since a priori correction of borehole EIT measurements as in the case of inductive coupling was not possible, this correction procedure relies on the integration of discrete capacitances in the electrical forward model describing the borehole EIT measurements.

The developed correction methods for inductive and capacitive coupling were successfully verified with test measurements under controlled conditions. For EIT measurements with a single electrode chain, a phase accuracy of better than 1 mrad was achieved for frequencies up to 10 kHz. In the case of EIT measurements with two electrode chains, a phase accuracy of 1 mrad was achieved up to 1 kHz. A field evaluation of borehole EIT measurements at the Krauthausen test site also showed a considerable improvement of the phase accuracy by applying the correction methods. Here, it was observed that inductive coupling had a much stronger effect on the phase measurement than capacitive coupling. The complex electrical resistivity determined from 1D inversions of the borehole EIT measurements matched well with the general stratigraphy of the test site.

The correction procedures outlined above were developed specifically for the custom-made EIT system and electrode chains. In a final step, the applicability of the

correction procedures to commercially available electrode chains was explored. In particular, the possibility of performing accurate borehole EIT measurements using passive unshielded and shielded electrode chains was evaluated. In addition to the inductive and capacitive coupling, the use of this type of electrode chains requires the consideration of the capacitive load of the cables. It was shown that the phase errors due to the internal structure of the passive shielded electrode chains can be estimated using electrical circuit simulation. It was found that the phase error of the passive shielded electrode chains was about 1.5 mrad bigger as for the custom-made active electrode chains due to different capacitances between the electrode chains and the soil (in a conductive environment). Therefore, borehole EIT measurements with passive shielded electrode chains resulted in a reasonable phase accuracy of 3 mrad at 1 kHz. Finally, it was also confirmed that unshielded electrode chains are not suitable for accurate phase measurements at high frequencies because the induced phase errors cannot be predicted.

Although the results presented in this thesis are promising, there still is room to further improve the correction procedures. In this study, the electromagnetic response of the underground was neglected because of the small size of the electrode layouts in the field measurements and the used frequencies (up to 1 kHz). If a further expansion of the frequency range is required or when longer electrode arrays will be used, this effect will also need to be considered. The modeling of capacitive effects can also be improved. In particular, the spatial resolution of the meshes used for finite element modeling was limited by available computational resources, which could have caused a certain degree of inaccuracy in the modeling. Furthermore, the calibration procedure to determine the additional parasitic inductance of the short-circuiting wires by using a calibration measurement on two nearly identical electrode chains was complex and should be simplified.

Overall, it can be concluded that the developed correction methods for borehole EIT measurements resulted in a high phase accuracy (about 1 mrad at 1 kHz) when the custom-made EIT measurement system was used with active electrode chains. It was also shown that the correction methods to account for inductive and capacitive coupling can be applied to passive shielded electrode chains with a significant improvement in accuracy (about 3 mrad at 1 KHz). Therefore, this work opens up new research avenues where broadband EIT measurements can be used for improved characterization of hydrogeological and biogeochemical properties and processes in the field.

Danksagung

Zuerst möchte ich mich bei allen bedanken, die mich bei der Anfertigung dieser Arbeit unterstützt haben.

Mein ganz besonderer Dank geht an meinen Betreuer, Herrn Dr. Egon Zimmermann, der mir während meiner Promotion immer mit Rat und Tat zur Seite stand. Seine wertvollen Anregungen und Ratschläge habe ich immer geschätzt. Ohne seine zielgerichtete Betreuung wäre die Arbeit in dieser Form nicht möglich gewesen.

Ein weiterer besonderer Dank gilt meinem Doktorvater, Herrn Prof. Dr. Andreas Kemna, für die Bereitstellung des Themas dieser Dissertation, die Förderung und Durchsicht der Arbeit sowie seine Unterstützung und seinen fachlichen Rat.

Herrn Prof. Dr. Johan Alexander Huisman danke ich für die Bereitschaft die Arbeit zu begutachten und vor allem für das Korrekturlesen und viele konstruktiven Anregungen und Vorschläge zu dieser Arbeit.

Herrn Prof. Dr. Clemens Simmer und Herrn Prof. Dr. Jochen Garcke danke ich für die Begutachtung der Arbeit.

Meinen Kollegen aus der Arbeitsgruppe vom ZEA-2, insbesondere Herrn Bernd Wolters, Herrn Joachim Berwix, Herrn Walter Glaas, Herrn Heinrich Meier und Herrn Dr. Achim Mester danke ich für die Bereitstellung des EIT-Feldsystems und die hilfreichen Vorschläge und interessanten Ideen während meiner Promotion, die wesentlich zum Gelingen der Arbeit beigetragen haben.

Meinen Kollegen vom IBG-3, insbesondere Frau Andrea Treichel, Frau Odilia Esser, Herrn Dr. Sadam Al-Hazaimay, Herrn Matthias Kelter, und Herrn Dr. Franz-Hubert Hägel danke ich für die gute Zusammenarbeit, die Mithilfe bei den Feld- und Labormessungen und die vielen hilfsreichen Diskussionen.

Zu guter Letzt danke ich meiner Frau Ru und meinen Eltern. Ohne ihre Unterstützung und Begleitung auf meinem Ausbildungsweg wäre der heute erzielte Abschluss nicht möglich gewesen.（最后我要特别感谢我的妻子王儒和我的父母，如果没有他们对我在求学道路上一如既往的支持和鼓励，我是绝不可能取得今天的成绩的。）

Contents

List of Figures

List of Tables

Symbols

ε^*	complex permittivity
ε_0	vacuum permittivity
ε_∞	high-frequency permittivity
ε_r	relative dielectric permittivity
γ	eddy current constant
μ_0	magnetic field constant
v	saturation exponent
ρ^*	complex electrical resistivity
σ	conductivity
σ^*	complex conductivity
σ'	real part of the complex conductivity
σ''	imaginary part of the complex conductivity
$\lvert\sigma\rvert$	magnitude of the complex conductivity
σ_{el}	electrolytic conductivity
σ_{int}	interfacial conductivity
σ_w	conductivity of pore water
τ_0	relaxation time
φ	phase angle

Φ	porosity
ω	angular frequency
a	proportionality constant
A	area
c	Cole-Cole exponent
C	capacitance
d	thickness
F	formation factor
G	electrical conductance
$h(\sigma_w)$	function of salinity
i	imaginary unit
I	injection current
I(f)	current in frequency domain
j	imaginary unit
K	geometry factor
l	length
L	inductance
$L^0(r)$	earth-return inductance
m	chargeability / cementation exponent
M	mutual inductance
M	matrix of Inductances
n	saturation exponent

$P(r)$	mutual inductance between wires with distance r
$Q(r)$	grounding function
$Q^0(r)$	resistivity of the soil
r	distance
R	radius
S_{por}	specific surface area
S_w	water saturation
T	period
$U(f)$	voltage in frequency domain
$u(t)$	voltage in time domain
Y	admittance
$\boldsymbol{Y}$	admittance matrix
Z	transfer impedance
Z_{CR}	corrected transfer impedance
Z_{ind}	mutual impedance due to inductive coupling
Z_m	measured transfer impedance

1 Introduction

1.1 Background and Motivation

For geophysicists, it is important to understand the electrical conductivity of soils, sediments, and rocks. It is determined by electrical conduction and polarization (charge transport and separation) occurring inside these porous media. While electrical conduction occurs in the electrolytically conductive pore fluid, electrical polarization arises at the interface between mineral grains and the pore fluid (Pelton *et al.* 1978). In order to describe both conduction and polarization processes on a macroscopic scale, the complex electrical resistivity or conductivity expressed with a real and imaginary part (or magnitude and phase) is used.

The proper understanding of the complex electrical resistivity is the basis for geophysical data interpretation in various fields of applied geophysics (engineering or environmental applications; Kemna 2000). For example, direct current (DC) and induced polarization (IP) methods (see e.g. Bertin and Loeb 1976) are routinely used to investigate subsurface electrical conduction and polarization phenomena, respectively. With IP, the magnitude and phase angle of the complex electrical resistivity are obtained for a single frequency (e.g. Hördt *et al.* 2007; Karaoulis *et al.* 2011; Kemna *et al.* 2004). When effective measurements of the frequency-dependent complex electrical resistivity are made in the laboratory across a broad range of frequencies from mHz to kHz, this is commonly referred to as the spectral IP (SIP) method (Binley *et al.* 2005; Leroy *et al.* 2008; Zimmermann *et al.* 2008b; Breede *et al.* 2012). In the last decade, laboratory and field investigations have reported close relations between the complex electrical resistivity and important hydrogeological properties, such as pore geometry, pore fluid chemistry (Lesmes and Frye 2001; Kemna *et al.* 2005), saturation (Ulrich and Slater 2004; Binley *et al.* 2005) and mineral surface properties (see e.g. Vanhala 1997; Slater and Lesmes 2002; Binley *et al.* 2005). These studies have also clearly shown the benefits of broadband measurements of the complex electrical conductivity in the mHz to kHz frequency range. Unfortunately, these studies have also revealed that most soils, sediments and rocks typically show phase angles between 1 and 20 mrad only, which means that a high phase accuracy of the measurement system is required to investigate these low-polarizable porous media.

In recent years, there is increasing interest to combine the diagnostic potential of effective laboratory SIP measurements in a broad range of frequencies with the imaging capability associated with tomographical measurement approaches. This can be achieved using a relatively new method that is referred to as spectral electrical impedance tomography here (spectral EIT, see e.g. Kemna *et al.* 2000). At the start of this thesis, spectral EIT with high phase accuracy could be achieved already in the laboratory. Under optimal conditions, the spectral EIT data acquisition system developed by Zimmermann *et al.* (2008) has obtained a phase accuracy of better than 1 mrad at 1 kHz in the laboratory. The recent work of Kelter *et al.* (2015) illustrates that this advanced laboratory EIT system in combination with state-of-the-art data processing and inversion procedures can provide phase-accurate distributions of the spectral electrical properties within soil and sediment columns in the mHz to kHz frequency range. The reason for the accurate phase measurements with this laboratory EIT system are that a range of errors due to the inner electronics are modeled and removed during post-processing. In addition, the true injection current and the output voltage are measured accurately, and active electrodes with short coaxial cables (< 1.5 m) are used to minimize electromagnetic coupling during the measurements (more details about the EIT measurement equipment is provided in section 2.3).

An important question at the start of this thesis and the main motivation for the presented research is how to transfer spectral EIT measurements from the laboratory to the field without losing the high phase accuracy that has been achieved in the laboratory. Current field measurements using time-domain or frequency-domain IP have been restricted to relatively low frequencies (<100 Hz) due to electromagnetic coupling effects (inductive and capacitive coupling) associated with the use of long electrode cables needed to characterize the subsurface to sufficient depth with a proper resolution (Kemna *et al.* 2000; Zimmermann *et al.* 2010). Several previous studies have attempted to reduce these electromagnetic coupling effects. For example, passive coaxial cables have been used to avoid cross-talking (capacitive and inductive coupling) between cables (Zimmermann *et al.* 2008b, Flores Orozco 2012). In addition, specific electrode configurations (perpendicular electrode array) and cable layouts have been used to minimize the inductive coupling between the cables (Wynn and Zonge 1975, Wynn and Zonge 1977). In these two studies, a modeling approach to predict inductive coupling was also presented. Despite these efforts, the frequency range with sufficiently accurate phase measurements is still limited for spectral EIT measurements in the field. For example, Kemna (2000) presented results up to a frequency of 64 Hz, Flores Orozco (2012) up to 256 Hz, and Zonge and Wynn (1975) up to 110 Hz. Therefore, there is a clear need to develop correction approaches for

electromagnetic coupling effects so that images of the complex electrical resistivity can be obtained in a wide frequency range that extends from mHz to kHz.

1.2 Thesis Objectives and Outline

In order to allow broadband spectral EIT measurements in the field, the laboratory EIT system of Zimmermann et al. (2008) was extended with borehole electrode chains with active electrodes. The aims of this thesis are i) to develop correction procedures to remove phase errors introduced by inductive and capacitive coupling due to the use of electrode chains with active electrodes, and ii) to evaluate whether passive electrode chains can also be used to obtain accurate EIT field measurements in the high frequency range (up to 1 kHz) by using these correction methods.

The remainder of this thesis consists of five parts. In chapter 2, the theoretical background of the electrical properties of soil, sediments and rocks, the measurement principles, and the EIT measurement system used in this thesis is introduced. In chapter 3, inductive and capacitive coupling effects associated with long electrical cables are systematically investigated for borehole EIT measurements in a single borehole. Correction procedures to address both types of coupling effects are presented and validated using measurements under controlled conditions. In addition, the improvement of accuracy is illustrated using 1D inversion results of field EIT measurements obtained in the heterogeneous aquifer of the Krauthausen test site. In chapter 4, inductive and capacitive coupling effects in borehole EIT measurements in two boreholes are investigated. In this case, the inductive coupling is much stronger due to the larger electrical loops and additionally depends strongly on the cable layout in the field. Again, the developed correction methods will be verified with measurements under controlled conditions and EIT inversion results from the Krauthausen test site. Chapter 5 explores whether the developed correction methods can also be applied to passive shielded and unshielded electrode chains. The possible phase errors associated with the additional capacitive load of long wires are analyzed and estimated, and field measurements with both active and passive electrode chains are presented to evaluate remaining phase errors after correction of the inductive coupling. Finally, the main outcomes of the thesis are summarized in chapter 6 and the thesis is concluded with an outlook on possible future applications and some recommendations to further improve the developed phase correction methods.

2 Theoretical Background

2.1 Electrical conductivity

The electrical conductivity σ is a material-specific property that describes the relationship between the current density and the field strength. It can be described by a complex number that can either be expressed by a magnitude and a phase:

$$\sigma^* = |\sigma| e^{i\varphi}, \tag{2.1}$$

or a real and imaginary part:

$$\sigma^* = \sigma' + i\sigma'', \tag{2.2}$$

where *i* is the imaginary unit, $|\sigma|$ is the magnitude, $\varphi = arctan(\sigma''/\sigma')$ is the phase angle, σ' and σ'' are the real and imaginary part of the complex conductivity σ^*, respectively. The inverse of the electrical conductivity σ^*:

$$\frac{1}{\sigma^*} = \rho^* \tag{2.3}$$

is the complex electrical resistivity ρ^*. In the EIT (or SIP) method, the frequency dependency of electrical conduction (charge transport) and polarization (charge separation) expressed by the complex electrical conductivity (or resistivity) is measured in a typical frequency range between 1 mHz and several kHz (Kemna *et al.* 2000; Kemna *et al.* 2012; Kelter *et al.* 2015).

Depending on the composition of soils, sediments and rocks, electrical conduction occurs in three forms: electrolytic conductivity, interfacial conductivity, and electronic conductivity. For materials without semiconductors or metallic conductors, Waxman and Smits (1968) described the total or bulk conductivity as a parallel connection of the electrolytic and interfacial conduction, which are associated with the electrolyte-filled pore space and the boundary surface between the solid and the fluid phase (figure 2.1):

$$\sigma = \sigma_{el} + \sigma_{\text{int}}. \tag{2.4}$$

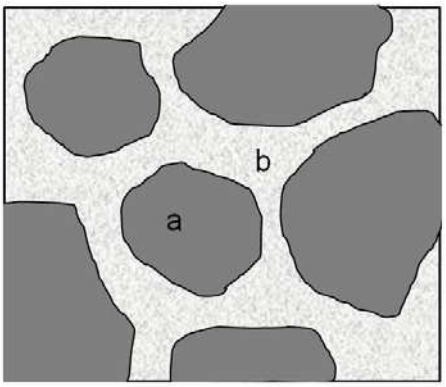

Figure 2.1: Porous rocks filled with electrolyte; a: solid material; b: electrolyte-filled pore space.

The electrolytic conductivity σ_{el} is associated with ion movement in the aqueous solution within the porous media and can be described after Archie (1942):

$$\sigma_{el} = \frac{\Phi^m}{a}\sigma_w S_w^n, \tag{2.5}$$

where Φ is the porosity, σ_w is the conductivity of the pore water, S_w is the water saturation, *m* is the cementation exponent, *n* is the saturation exponent, and *a* is a proportionality constant. A more detailed description of these parameters is given in Schön (1996). Interfacial conductivity depends on the pore surface properties (Börner and Schön 1991) and is associated with so-called electrical double layers at the interface between the negatively charged surface and the pore solution (e.g. see Ward and Fraser 1963). Börner *et al.* (1996) described the complex interfacial conductivity of sedimentary rocks as:

$$\sigma_{\text{int}} = \frac{h(\sigma_w)S_{por}}{F} S_w^{\nu}(1+il), \tag{2.6}$$

where $h(\sigma_w)$ is a function of salinity, S_{por} is the specific surface area, $F=a/\Phi$ is the formation factor (compare to eq. 2.5), S_w is the water saturation, ν is the saturation exponent, and *l* reflects the actual separation of σ_{int} into a real and an imaginary part.

The frequency dependency of the complex electrical conduction is often described by the so-called Cole-Cole model (Cole and Cole 1941), which was originally formulated in terms of dielectric permittivity:

$$\varepsilon = \varepsilon_\infty + \frac{\varepsilon_0 - \varepsilon_\infty}{1+(i\omega\tau_0)^c}, \tag{2.7}$$

where ε is the complex permittivity as a function of frequency, ε_0 is the vacuum permittivity, ε_∞ is the high-frequency permittivity, ω is the angular frequency, τ_0 is the relaxation time and *c* is the Cole-Cole exponent that determines the degree of dispersion. This model was derived to explain experimental observations on various dielectric materials and was

adopted by Pelton *et al.* (1978) to describe the spectral behavior of the complex electrical resistivity of mineralized rocks:

$$\rho = \rho_\infty + \frac{\rho_0 - \rho_\infty}{1 + (i\omega\tau_0)^c}. \tag{2.8}$$

With the following definition of the chargeability

$$m = 1 - \frac{\sigma_0}{\sigma_\infty} \tag{2.9}$$

the Cole-Cole model for the complex specific electrical conductivity is (Binley *et al.* 2005; Slater 2007):

$$\sigma = \sigma_0\left(1 + m\frac{(i\omega\tau)^c}{1 + (i\omega\tau)^c(1-m)}\right). \tag{2.10}$$

2.2 SIP measurements

In SIP or EIT measurements, the magnitude and phase (or real and imaginary components) of the transfer impedance are measured for a range of frequencies. The transfer impedance *Z* of the measurement object is related to the complex resistivity as follows (Knödel *et al.* 2002):

$$\rho = K \cdot Z, \tag{2.11}$$

where *K* is the geometry factor which describes the relative geometrical relations between the electrodes (Broding and Rummerfield 1955). The frequency-dependent transfer impedance in four-point measurements is given by:

$$Z(f) = \frac{U_m(f)}{I_s(f)}, \tag{2.12}$$

where $U_m(f)$ is the measured voltage and $I_s(f)$ is the injected current (figure 2.2).

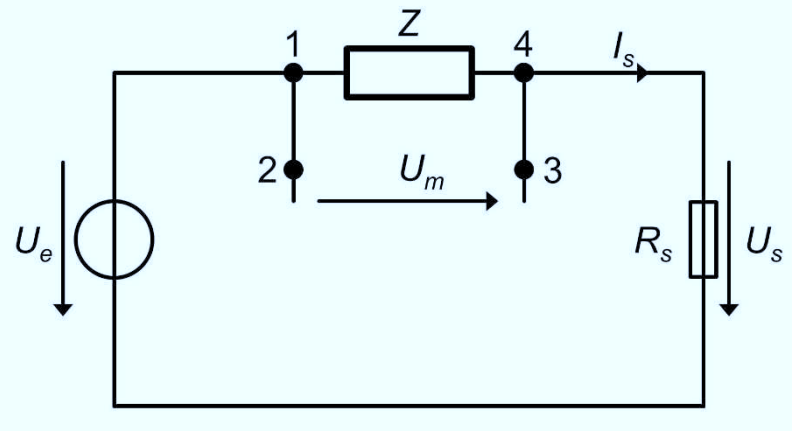

Figure 2.2: Electric circuit for a four-point measurement of the transfer impedance, Z (after Zimmermann *et al.* 2008b).

In figure 2.2, the current is injected through the electrodes 1 and 4, while the voltage is measured at two other electrodes 2 and 3. The shunt resistor is used to determine the injection current $I_s = U_s/R_s$ by measuring the voltage U_s. Thus, the impedance Z can be calculated with the measured U_m and U_s (Zimmermann *et al.* 2008b):

$$Z(f) = R_s \frac{U_m(f)}{U_s(f)}. \tag{2.13}$$

In an actual measurement, both voltages in (2.13) are first measured in the time domain and then converted into the frequency domain using a Fourier transformation (Zimmermann 2011):

$$U(f) = \frac{2}{T}\int_0^T u(t)e^{-i\omega t}dt = \frac{2}{T}\int_0^T u(t)\cos(\omega t)dt - i\frac{2}{T}\int_0^T u(t)\sin(\omega t)dt, \tag{2.14}$$

where $u(t)$ is the measured time series, T is the period, $\omega = 2\pi/T$ is the angular frequency of the excitation, and $U(f)$ stands for the voltages in the frequency domain. In order to make the measurements as accurate as possible and to avoid nonlinear distortion, sinusoidal signals are used as excitation signal. The transfer impedance is estimated sequentially for a number of angular frequencies across the mHz to kHz frequency range in order to obtain a discrete spectrum of impedances.

2.3 EIT measurement system

The EIT40 laboratory system was designed to perform accurate measurement of the spectral induced polarization response of soil and sediment samples. This system has 40 channels that can be used for current injection and potential measurement (figure 2.3). A multi-functional electrode module (UI01 – UI40) that consists of an integrated relay for current injection and an amplifier for potential measurement is connected to each channel (Zimmermann *et al.* 2008).

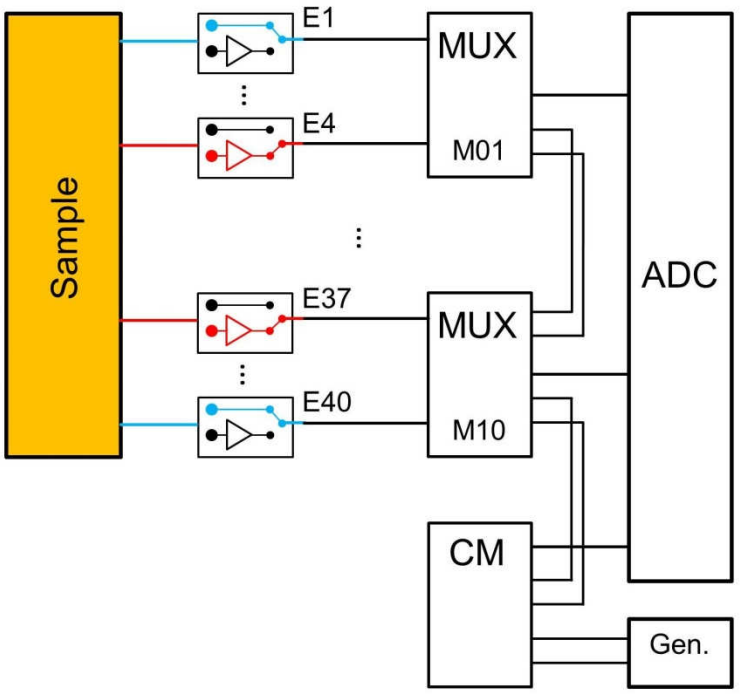

Figure 2.3: Electric circuit of the EIT40 laboratory system (after Zimmermann *et al.* 2010).

For each EIT measurement, two electrodes are selected for current injection and all other electrodes are used for potential measurement. To select the two channels for current injection, multiplexers are used that are controlled by NI-controller (NI-PXI 8108, National Instruments). Each multiplexed card has two ports for voltage sources and two shunt resistors to measure the injection current in the two active current channels using an additional current measurement (CM) card, which also symmetrizes the excitation signal and thus minimizes the leakage currents. All the measured signals are digitized by the 24-bit sigma-delta analog-digital converters (ADC) on the NI data acquisition cards (NI-PXI 4472, National Instruments) and then send to the NI-controller. The measurement program is based on LabVIEW and controls the ADCs and the function generator (Agilent 33220A), which provides the sinusoidal excitation voltage (max. 10 V) with possible frequencies between 1 mHz and 45 kHz. It reads the measurement configuration files provided by the user and stores the time series of all signals for each frequency. The MATLAB-based post-processing software computes the complex voltages $U(f)$ from the measured time series $u(t)$ at each excitation frequencies using (2.14). It also removes drift errors due to the inner electronics and determines the true current injection and the resulting transfer impedances. For more details about the EIT measurement system, the reader is referred to Zimmermann *et al.* (2008). This EIT laboratory system has reached a phase accuracy of better than 1 mrad at 1 kHz for measurements on well-defined test objects.

2.4 Borehole EIT measurement system

For borehole measurements, the laboratory EIT system was extended with active electrode chains built of 25 m long shielded multi-core cables equipped with eight multi-functional electrode modules with integrated amplifiers (Zimmermann *et al.* 2010). The electrode chains are connected to the EIT40 system using an adapter box (more details are provided in section 3.2). The used electrode chains are custom-made and have a complex design with electronics near the electrodes, which results in a relatively large size and problems with the water tightness of the chain. A simple alternative would be the use of passive shielded or unshielded electrode chains, and the feasibility of measurements with these cables is discussed in detail in chapter 5.

3 Broadband EIT borehole measurements with high phase accuracy using numerical corrections of electromagnetic coupling effects *

3.1 Introduction

In order to image the spectral phase response of low-polarizable objects such as soils and rocks (Kemna *et al.* 2011), an advanced spectral EIT data acquisition system was developed (Zimmermann *et al.* 2008). Recently, this system was extended with borehole logging tools and electrode chains for near-surface borehole measurements. Both the logging tool and the electrode chain use long electrical cables to connect the electrodes to the EIT data acquisition system. Faraday's law predicts that such long electrical cables can lead to substantial inductive coupling between the electric loop for current injection and the electric loop for potential measurement. Such inductive coupling could distort the measurement of the complex impedance, especially the imaginary part and thus the phase angle. Besides inductive coupling, the measured imaginary part of the complex impedance may also be affected by capacitive coupling between the cable and the electrically conductive environment (Madden and Cantwell 1967). Capacitive coupling occurs between conductors that have different electric potentials, e.g. the potential difference between the conductive shield of the cable and the environment around it. Depending on the electrical properties of the subsurface and the measured transfer impedances, both inductive and capacitive coupling effects can cause large phase errors that have typically limited the frequency bandwidth of field EIT measurements to the mHz to Hz range.

In this contribution, it is aimed to model inductive and capacitive coupling for borehole EIT measurements in a single borehole in order to derive correction procedures that will allow us to achieve high phase accuracy in the mHz to kHz frequency range. The correction procedures will be validated using measurements under controlled conditions, and the improvement of accuracy that can be achieved by applying the derived corrections will be

* Adapted and modified from Zhao Y, Zimmermann E, Huisman J A, Treichel A, Wolters B, van Waasen S, and Kemna A. 2013. Broadband EIT borehole measurements with high phase accuracy using numerical corrections of electromagnetic coupling effects. *Meas. Sci. Technol.,* **24,** 085005.

illustrated using 1D inversion results of EIT measurements made with a borehole electrode chain with 8 electrodes and an electrode spacing of 1 m.

3.2 EIT Measurement Set-up for Borehole Measurements

We use four electrodes to measure impedance; two electrodes are used for current injection and two electrodes are used for potential measurements. The EIT data acquisition system has 40 channels and operates in the frequency range from 1 mHz to 45 kHz. For more details about system design, we refer to Zimmermann *et al.* (2008). The recently developed borehole logging tool (figure 3.1a) and electrode chain (figure 3.1b) are equipped with dual-functionality electrode modules with integrated amplifiers for electric potential measurements and integrated switches for current injection (Zimmermann *et al.* 2010). Therefore, all electrodes can be used for current injection and potential measurements. The borehole logging tool is equipped with 4 electrode modules with an electrode separation of 16.2 cm. The electrode chain is equipped with eight electrode modules with an electrode spacing of 100 cm. To ensure a good electric contact with the surrounding medium, we used brass ring electrodes with a diameter of 42 mm and a height of 10 mm. The electrode modules are connected to an adapter box close to the EIT data acquisition system using a 25 m long multi-core electrical cable. Single cables are used between the adapter box and the EIT system (Zimmermann *et al.* 2010). Additional electrical wires are used for power supply and control of the electrode modules, but these wires have no effect on inductive coupling.

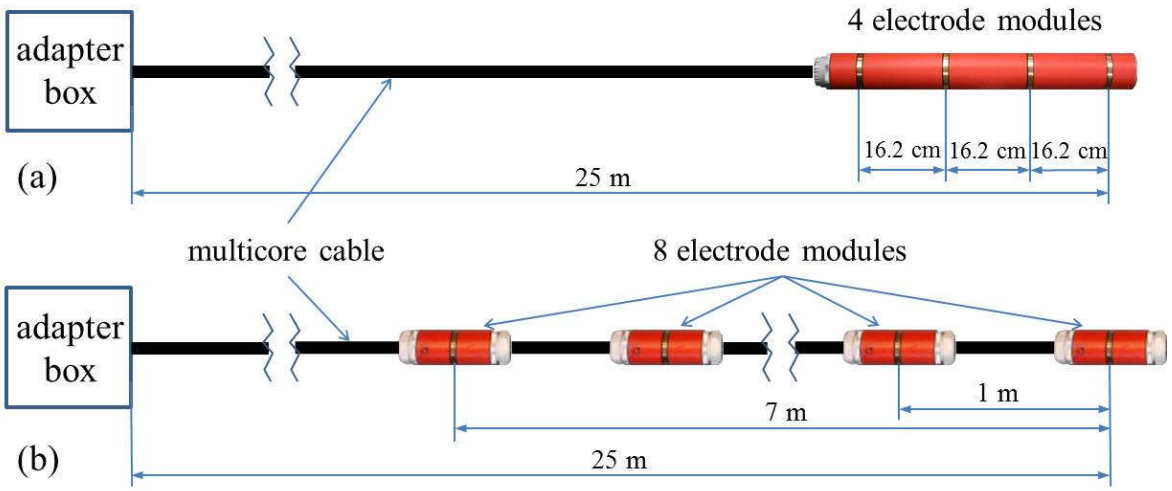

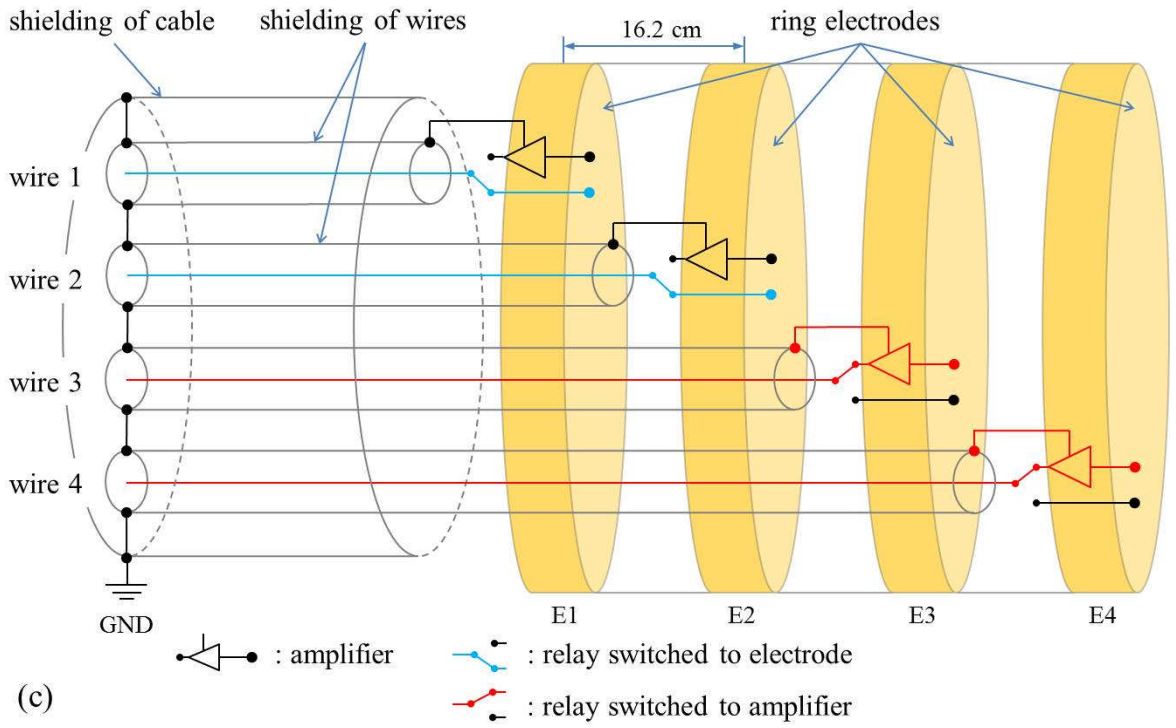

Figure 3.1: (a) Borehole logging tool, (b) Borehole electrode chain, (c) Simplified block circuit diagram of the borehole logging tool.

Figure 3.1c provides a simplified block circuit diagram for the borehole logging tool. The electrodes are numbered from top to bottom with 1, 2, 3 and 4. The electrodes are connected to wires inside the cable bundle with the same numbering. In figure 3.1c, electrodes 1 and 2 are used for current injection (blue lines) and electrodes 3 and 4 are used for potential measurements (red lines). All the shields are connected with each other, so that the electrode potential is measured directly against the reference potential of the shields. The block circuit diagram of the electrode chain is identical, except for the larger number of electrodes.

3.3 Inductive Coupling – Modeling and Correction

Sunde (1968) presented an equation to calculate the mutual impedance Z_m^p of two grounded wires in a horizontal plane (see figure 3.2 for an explanation of the variables):

$$Z_m^p = \int_{C_1}^{C_2} \int_{P_1}^{P_2} \left[\frac{\partial^2 Q(r)}{\partial s \partial S} + P(r) \cos \varepsilon \right] ds dS \tag{3.1}$$

where

$$Q(r) = \frac{1}{2\pi\sigma r} \tag{3.2}$$

$$P(r) = \frac{i\mu_0\omega}{2\pi r}\left[\frac{1-(1+\gamma r)e^{-\gamma r}}{(\gamma r)^2}\right] \tag{3.3}$$

$$\gamma = (i\sigma\mu_0\omega)^{1/2}\,. \tag{3.4}$$

In these equations, *r* is the distance, ε is the angle between the line element *s* and *S*, *i* is the imaginary unit, ω is the angular frequency, γ is the eddy current constant, μ_0 is the magnetic field constant, and σ is the electric conductance. The mutual inductance between the wires *P(r)* and the effect of the subsurface *Q(r)* is considered (see also Wait 1984 and Wynn and Zonge 1977). The inductive component in (3.1) produced by the mutual inductance is given by

$$Z_L = \int_{C_1}^{C_2}\int_{P_1}^{P_2}\left[P(r)\cos\varepsilon\right]dsdS\,. \tag{3.5}$$

If the eddy current constant γ approaches zero (i.e. when the frequency approaches zero), this equation can be simplified to

$$Z_L = \frac{i\mu\omega}{4\pi}\int_{C_1}^{C_2}\int_{P_1}^{P_2}\frac{\cos\varepsilon}{r}dSds\,. \tag{3.6}$$

Z_L is produced by the pure mutual inductance *M* between the electrical wires, which is given by Neumann's integral (see e.g. Henke 2011):

$$M = \frac{\mu}{4\pi}\int_{C_1}^{C_2}\int_{P_1}^{P_2}\frac{\vec{ds}\vec{dS}}{r}\,. \tag{3.7}$$

In the case of EIT measurements in a single borehole, as considered in this study, the distance between the electrodes is typically small and the wires run parallel to each other (figure 3.3). The current i_I in the loop *I* produces a magnetic field B (see figure 3.3). A part of the magnetic flux passes through the conductor loop *II*, where an electric voltage will be induced. This is called mutual induction of two wire pairs, and the mutual inductance *M* can be calculated with Neumann's integral given in (3.7) or with the simplified Neumann's equation (see. e.g. Küpfmüller *et al.* 2008):

$$M = \frac{\mu_0 l}{2\pi}\ln\frac{r_{14}r_{23}}{r_{13}r_{24}}\,. \tag{3.8}$$

where r_{14}, r_{23} etc. describe the radial distances between the wires and *l* is the common length of the wires. Note that the wires should approximately have an infinite length compared to their diameter in this simplified equation. The induced voltage U_{II} between wires 3 and 4 (see figure 3.3) is then given by

$$U_{II} = i\omega M \cdot I_I\,. \tag{3.9}$$

At the measured object (e.g. soil), there also is a voltage U_0, which is given by

$$U_0 = Z_0 \cdot I_I\,. \tag{3.10}$$

where Z_0 is the desired transfer impedance. The measured voltage U_M is the sum of U_0 and U_{II} and thus the total measured transfer impedance is given by

$$Z_M = \frac{U_M}{I_I} = Z_0 + i\omega M \ . \tag{3.11}$$

This is a simplified form of (3.1). Z_M corresponds to Z_m^p, Z_0 corresponds to $Q(r)$, and $i\omega M$ corresponds to the inductive component Z_L in (3.5).

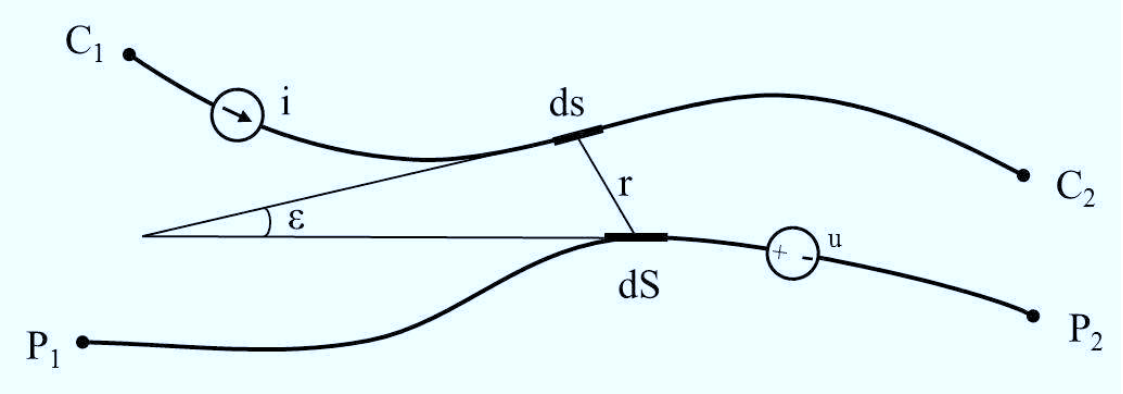

Figure 3.2: Layout of two grounded wires in a horizontal plane (C1 and C2: current electrodes, P1 and P2: potential electrodes), drawn after Wait (1984).

Equation (3.11) implies that the error due to inductive coupling can be removed by subtracting the term $i\omega M$ from the measured transfer impedance. In order to do so, the theoretical mutual inductances need to be calculated. This requires accurate knowledge of the geometry of the individual electric wires in the multi-core cable. Figure 3.4 (left) illustrates the internal structure of the multi-core cable we used (CORDIAL “CMG 16”). The cable consists of 16 twisted wires that are divided in two groups. The outer 11 wires are numbered from 1 to 11 and the inner 5 wires are numbered from 12 to 16. Each cross-section of the cable is identical (figure 3.4, right). However, both groups of wires turn with different slopes so that the outer wires need a longer path than the inner wires to reach the same effective cable length. Therefore, the simplified Neumann’s equation (3.8) does not apply if wires from different groups are used for the calculation of the mutual inductance. If we know the exact internal length of the electrical wires at each position of the twisted cable bundle, the integral form of Neumann’s equation (3.7) could be solved numerically. However, it is very costly and difficult to determine the exact cable geometry. Therefore, we decided to only use the outer wires of the twisted cable bundle for current injection and potential measurements. The inner wires are only used for power supply.

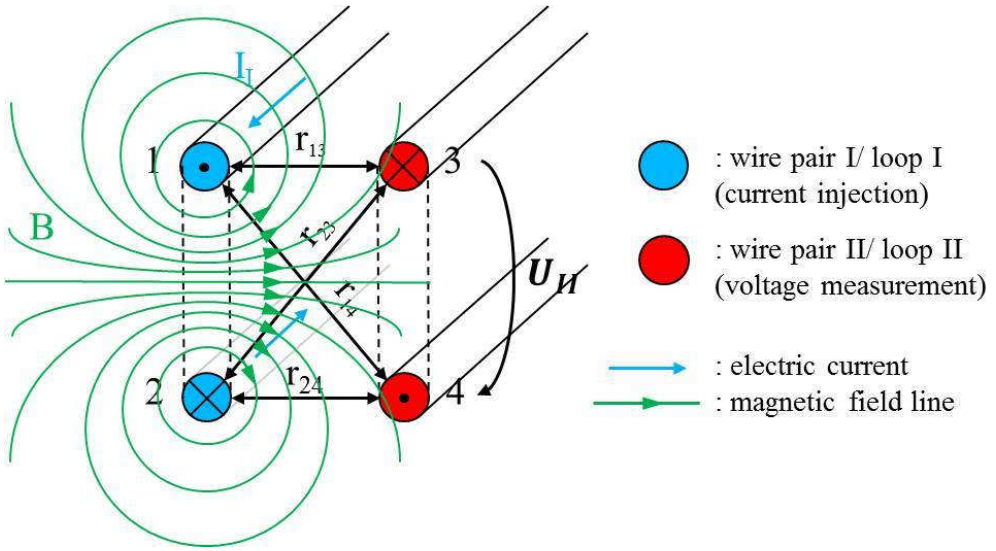

Figure 3.3: Mutual induction between two parallel electrical wire pairs.

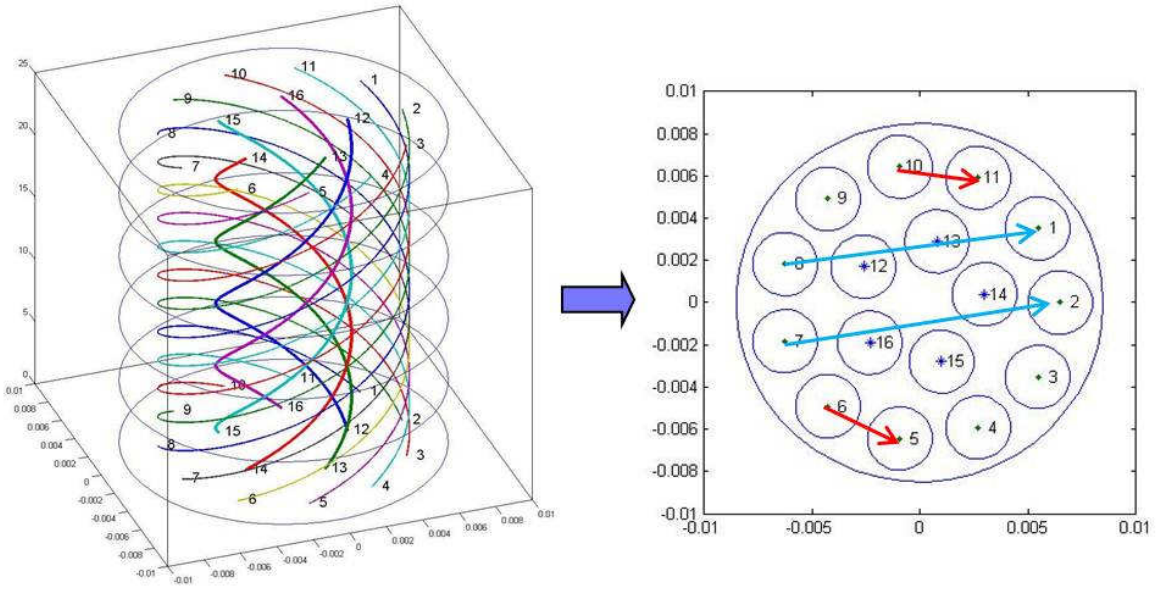

Figure 3.4: Internal structure (left) and one cross-section (right) of the cable.

To evaluate the appropriateness of (3.8) for the calculation of the mutual inductance at 1 kHz, we performed measurements with an impedance analyzer (Wayne Kerr 6500B, Wayne Kerr Electronics, Chichester, UK). In these measurements, two wire pairs of a 50 m long multi-core cable were connected to the impedance analyzer, whereas the other side was short-circuited. Table 3.1 compares the measured values and the calculated values. Each row of the table corresponds with a different combination of wire pairs for current injection and potential measurements. It can be seen that the blue configuration in figure 3.4, right (8 1 7 2) has a much higher mutual inductance than the red configuration (10 11 6 5). This is caused by the bigger overlap in area for the blue configuration. The measured and

calculated values agree very well with each other for the first four configurations with a relative error below 5%. As expected, measured and calculated values do not match when the inner wires (numbers 12 – 16) are used for current injection or potential measurements for reasons outlined above.

Table 3.1: Measured and calculated mutual inductances for different combinations of wire pairs for current injection (i-wires) and potential measurements (u-wires).

mutual inductance in [µH/m] at 1kHz							
i-wires		**u-wires**		**measured**	**calculated**	**deviation**	%
1	3	2	4	0.2048	0.1974	0.0074	3.6
1	4	2	3	0.2721	0.2607	0.0114	4.2
10	11	6	5	0.0177	0.0169	0.0008	4.3
8	1	7	2	0.5301	0.5026	0.0275	5.2
8	1	4	16	0.1370	–0.0298	0.3469	253.1
12	14	16	4	0.1824	0.2484	–0.0661	–36.2
15	16	10	8	0.0251	0.0708	–0.0457	–182.1

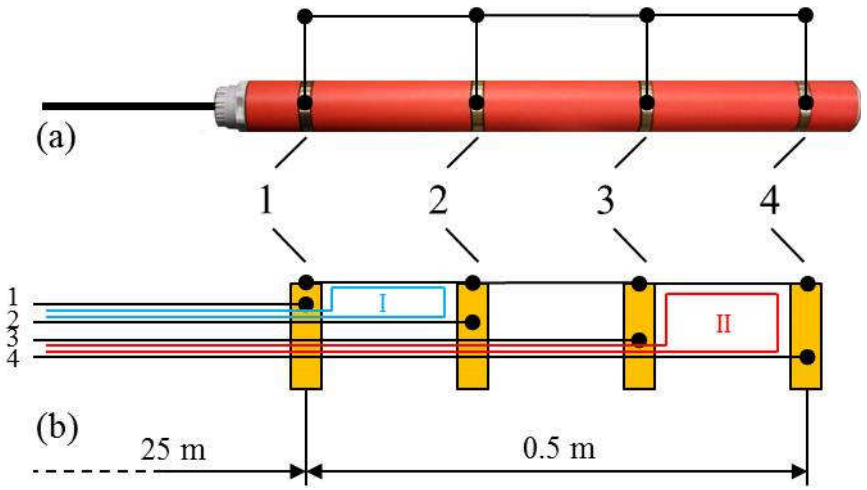

Figure 3.5: (a) Short-circuited borehole logging tool, (b) the associated electric circuit.

In the next step, the mutual inductance values were measured for the borehole logging tool. In order to do so, we short-circuited the electrodes with aluminum foil wrapped around the rod (figure 3.5a) and made measurements with the EIT data acquisition system. Figure 3.5b presents the two electric wire loops (I and II) that occur in the case of a dipole-dipole measurement configuration, which uses wires 1 and 2 for current injection and wires 3 and 4 for potential measurements. In the case of a short-circuited measurement, the current flowing in wire 1, wire 2, and the aluminum foil induces electrical potentials in wires 3 and 4,

which can be measured as a voltage at the wire ends. For such a measurement, the mutual inductance or rather the transfer impedance can be obtained as the quotient of the measured voltage and the injected current.

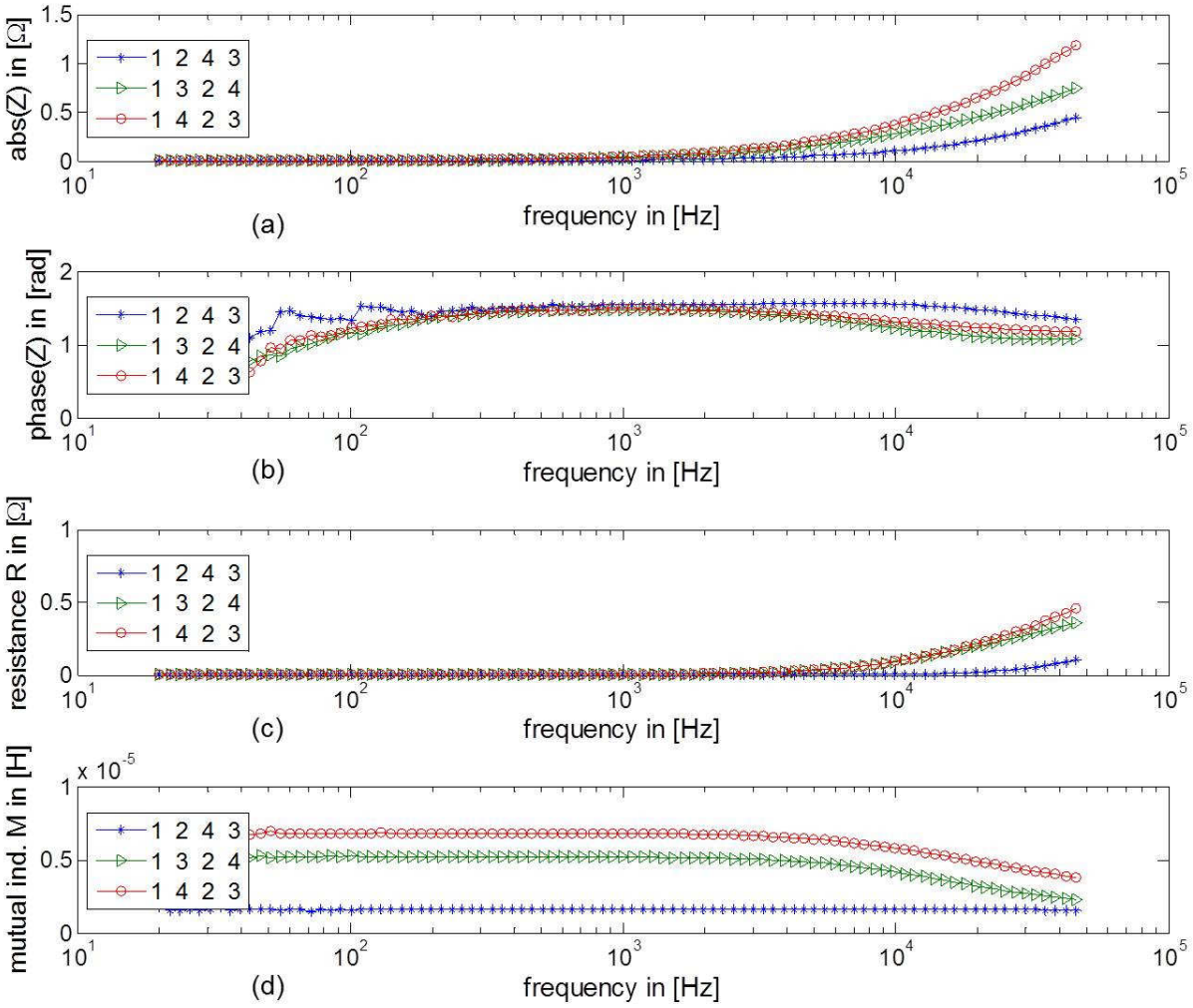

Figure 3.6: Measured transfer impedance for a short-circuited logging tool with a 25 m long multi-core cable for three measurement configurations (first two numbers indicate current injection electrodes, last two numbers indicate electrodes used for potential measurements).

Figure 3.6 shows the measured transfer impedance *Z* (magnitude and phase), the associated resistance *R* and the mutual inductance *M* as a function of frequency obtained using (3.11) for different measurement configurations. The mutual inductance *M* (figure 3.6d) remains almost constant up to about 1 kHz and the value below 1 kHz matches well with the calculated *M* value in table 3.1 for a cable length of 25 m (1 3 2 4: 4.9 µH; 1 4 2 3: 6.5 µH). For frequencies below 100 Hz, some variability in the measured mutual inductance can be observed, which is associated with the accuracy of the complex transfer impedance measurements. Above 1 kHz, the mutual inductance *M* decreases. As predicted by Kaden

(1959), this decrease is associated with an increase in the total resistance of the double line. This frequency dependent behavior is related to eddy currents in the conductive shielding of the multi-core cable at high frequencies (Wolfsperger 2008). These eddy currents cause a current displacement in the shielding, which decreases the available area for the primary magnetic field with increasing frequency (i.e. for high frequencies the resulting magnetic field is contained within the interior of the multi-core cable).

The wire pairs in the cable can be considered as a linear time invariant system (see Vogel 2011), which is minimum-phase in this case. Impedances consisting of such passive minimum phase electrical elements (*R*, *C* or *L*) should obey the Kramers-Kronig relation that relates the real and the imaginary components of the impedance (e.g. Macdonald and Urquidi-Macdonald 1990). The Cole-Cole model (Cole and Cole 1941) is a commonly used model for minimum phase systems and, therefore, it should also satisfy the Kramers-Kronig relation. Hence, we propose to verify the consistency of the measured impedance by fitting a modified Cole-Cole model. The original Cole-Cole model is written as

$$\varepsilon^* - \varepsilon_\infty = \frac{\varepsilon_0 - \varepsilon_\infty}{1 + (i\omega\tau_0)^{1-\alpha}} . \tag{3.12}$$

where ε^* is the complex permittivity, ε_0 is the vacuum permittivity, ε_∞ is the high-frequency permittivity, τ_0 is the relaxation time, and α varies between 0 and 1 depending on the degree of dispersion. If we replace ε by L in (3.12) and rearrange, we obtain

$$L^* = \frac{L_0 - L_\infty}{1 + (i\omega\tau_0)^{1-\alpha}} + L_\infty . \tag{3.13}$$

where L_0 and L_∞ are the inductance values for the low- and high-frequency range, and L^* is the complex inductance that can be calculated from the measured transfer impedance:

$$i\omega L^* = Z = R + i\omega M \ . \tag{3.14}$$

Therefore, the complex inductance equals

$$L^* = M + i \cdot \frac{R}{\omega} . \tag{3.15}$$

This equation shows that the real part of the complex inductance L^* equals the mutual inductance *M*. Figure 3.7 shows the measured data and the fitted Cole-Cole models for several electrode configurations. The measured data were less accurate in the lower frequency range due to the residual resistance of the aluminum foil. Therefore, the Cole-Cole parameters were fitted only for values above 1 kHz. In addition, the real part of L^* received more weight than the imaginary part during fitting. It can be seen that the fitted Cole-Cole model adequately describes the real part of measured L^* (figure 3.7a) in the entire frequency range. This is also true for the measured transfer impedance *Z* (figure 3.7c

and 3.7d). The ability of the Cole-Cole model to describe the measured transfer impedance confirms that the measurements fulfill the requirements of the Kramers-Kronig relation.

As outlined previously, it is sufficient to determine the mutual inductance *M* to correct the measured transfer impedances for inductive coupling according to (3.11). Since the mutual inductance is not constant in the frequency range of interest (figure 3.6d), there are two strategies for correction. First, the measured mutual inductance determined from short-circuit measurements in the laboratory can be used directly. Alternatively, the real part of the fitted Cole-Cole model can be used. In the following, we directly used the measured values to correct the transfer impedance.

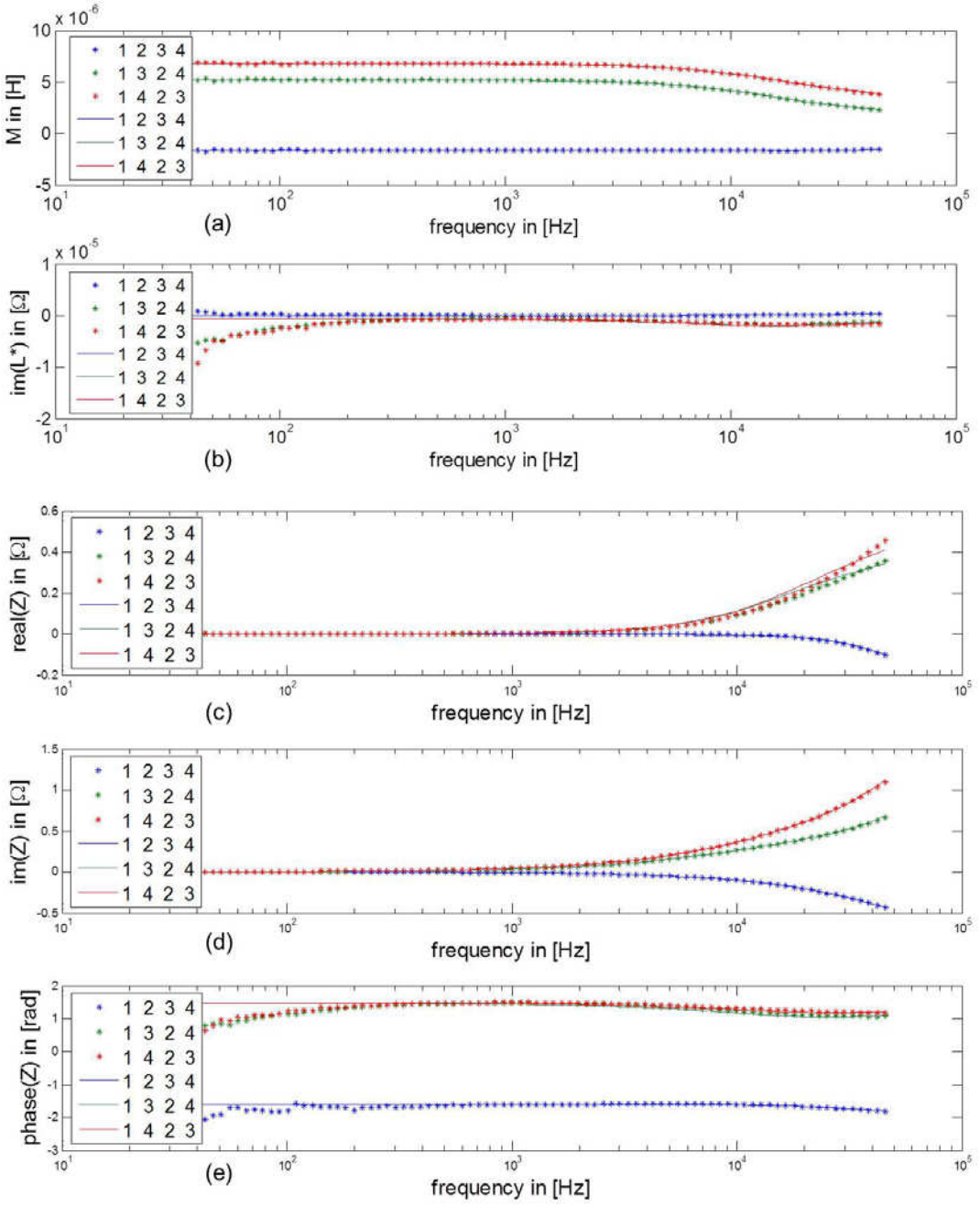

Figure 3.7: Measured transfer impedance for the short-circuited logging tool (asterisks) and the fit of the Cole-Cole model (solid curve).

To verify our proposed correction method, first test measurements were performed under controlled conditions in a water-filled rain barrel. The rain barrel is about 1.37 m high and has a diameter of 0.7 m (figure 3.8). It is made of polyethylene without any metal inside so that no polarization sources are present during the measurement. The borehole logging tool with a 25 m long multi-core cable was fixed in the center of the rain barrel, which was filled with tap water with an electrical conductivity, σ_w, of 0.029 S m^{-1}. The first electrode was located at a depth of 40 cm below the water surface.

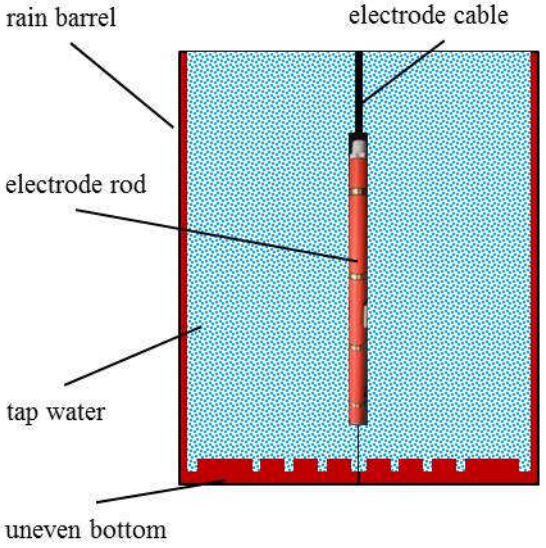

Figure 3.8: Simplified representation of the test measurement in the rain barrel.

The EIT data acquisition system was used to measure the transfer impedance, Z_{RB}, with the logging tool in the rain barrel. In the case of the Wenner measurement configuration (1 4 2 3), high and physically implausible positive phase values of up to 14 mrad were measured at 10 kHz (figure 3.9). After correcting Z_{RB} for inductive coupling using (3.11), the corrected transfer impedance, Z_{CR}, is obtained:

$$Z_{CR} = Z_{RB} - i\omega M \ . \tag{3.16}$$

The results for this correction are also shown in figure 3.9. The phase of the corrected transfer impedance is now negative as expected (figure 3.9c). At a frequency of 10 kHz, the phase of the corrected transfer impedance is –3.9 mrad. The expected phase associated with a measurement in water can be calculated by

$$\varphi = \arctan \frac{\omega \varepsilon_r \varepsilon_0}{\sigma_w} \ . \tag{3.17}$$

where ε_r is the relative dielectric permittivity of water (80.1 at 20°C). Although much improved compared to the uncorrected phase of the transfer impedances, the hatched area in figure 3.9c also indicates that there still is room for further improvement. For example, there is a difference of 2.4 mrad between the measured value and expected value at 10 kHz

(−1.5 mrad). Part of the remaining difference is associated with capacitive coupling effects that have not been considered at this point.

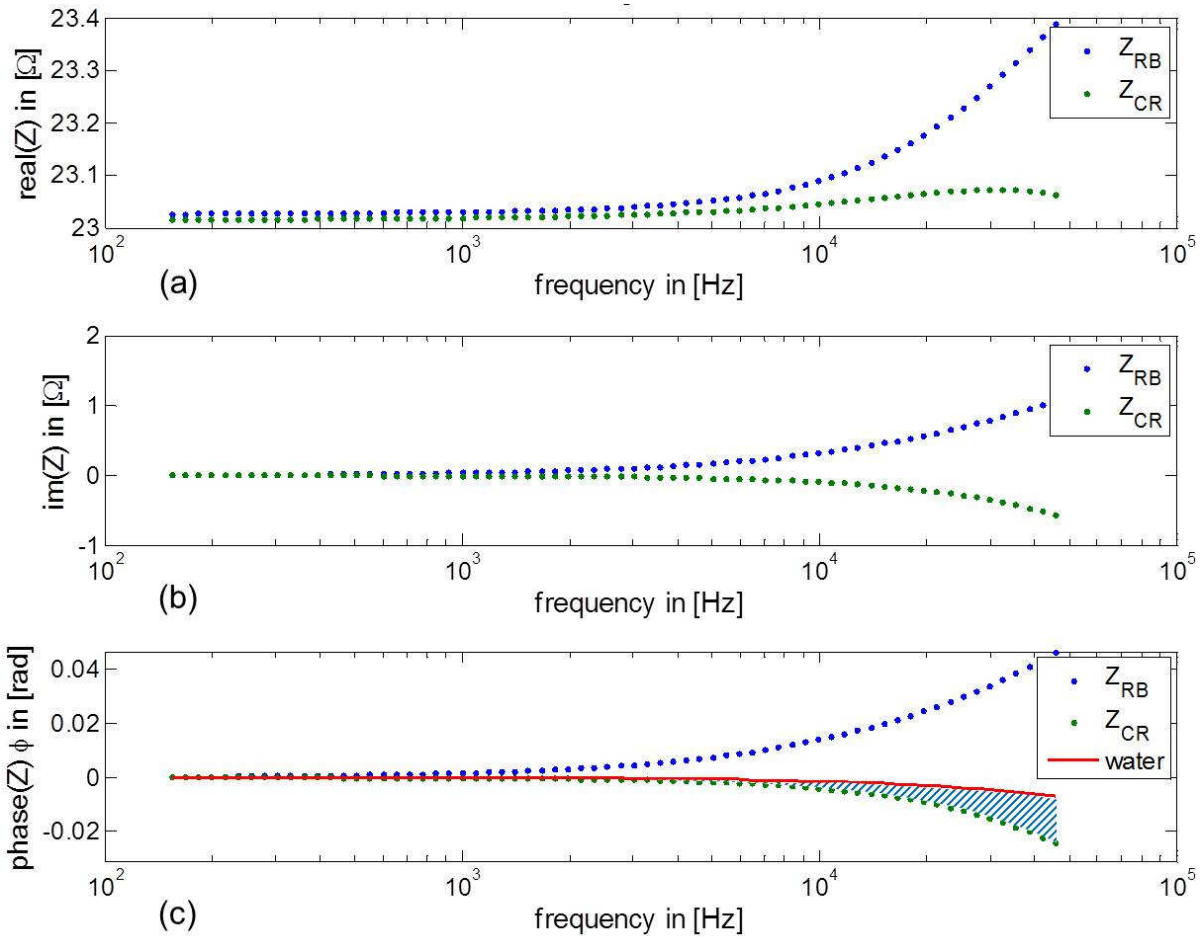

Figure 3.9: Uncorrected measured transfer impedances, Z_{RB}, and corrected transfer impedances, Z_{CR}, for a measurement with the logging tool and a Wenner electrode configuration. The hatched area indicates the difference between the corrected phase of the transfer impedance and the expected phase of the transfer impedance for a measurement in water.

3.4 Capacitive Coupling – Modeling and Correction

Wherever a potential difference exists, capacitive coupling can lead to phase errors. This effect is important to consider for borehole EIT measurements because of the long shielded cable with electric conductors. Figure 3.10 provides a simplified schematic drawing that illustrates the principle of capacitive coupling. The main part of the current flows from the upper electrode through the conductive medium to the lower electrode. However, uncontrolled parasitic currents that flow from the electrodes through the medium and the surface of the cable to the shield also occur because there is a potential difference between the electrodes and the grounded shield. The outer and inner surfaces of the material that

insulate the multi-core cable act like a small capacitor for these parasitic currents, which likely has a considerable impact on the accuracy of borehole EIT measurements because of the long cable that is typically lowered in the water-filled borehole.

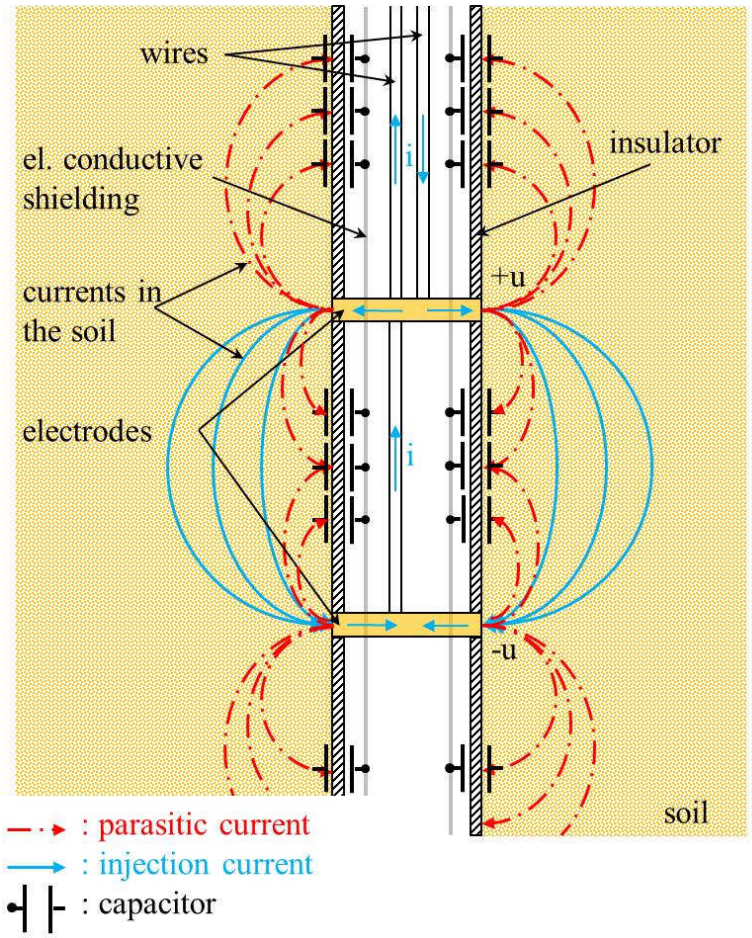

Figure 3.10: Capacitive coupling between cable and electrically conductive environment for an EIT borehole measurement.

The capacitance, *C*, of the multi-core cable can be approximated using an equation for a cylindrical capacitor (Plaßmann and Schulz 2009):

$$C = 2\pi\varepsilon_0\varepsilon_r \cdot \frac{l}{\ln\frac{R_2}{R_1}}, \tag{3.18}$$

where R_1 and R_2 are the inner and outer radii of the cylindrical capacitor, and l is the length of the cylinder. Assuming a relative permittivity of 4 for polyvinyl chloride (PVC), the calculated capacitance of the multi-core cable is 1175 pF/m (with R_1 = 7.25 mm and R_2 = 8.75 mm). The measured capacitance of the cable is about 1275 pF/m at 20 Hz (measured with the same impedance analyzer mentioned in section 3.3) and it decreases significantly with increasing frequency (figure 3.11). Therefore, the relative permittivity of the cable insulation must be frequency-dependent since all other variables in (3.18) are constant. Felger and Bassewitz (1986) also reported on such dispersion in the dielectric permittivity of

cable insulation material, and attributed this to the slow reorientation of molecule groups with permanent dipole moment within such polymer materials. Low-frequency dispersion of insulation materials in the kHz frequency range was also described by Wagner (1914).

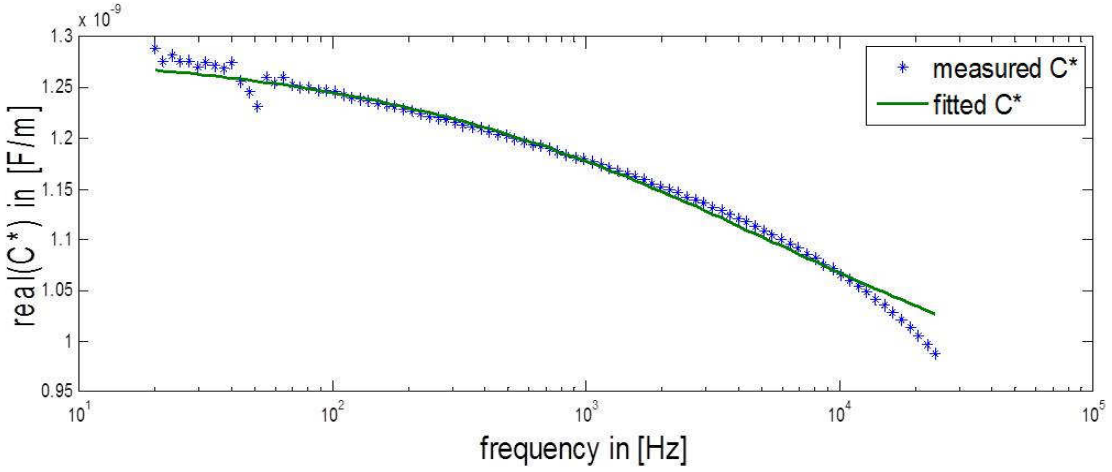

Figure 3.11: Measured and modeled real component of the complex capacitance C*, of a 0.91 m long cable.

To describe this frequency dependence, we use the complex capacitance, C^*, because it is linearly dependent on ε^*. It is given by

$$Y_C = \frac{1}{Z} = G + i\omega C = i\omega C^* \tag{3.19}$$

and

$$C^* = \frac{Y_C}{i\omega}, \tag{3.20}$$

where Y_C is the admittance and $G = 1/R$ is the electrical conductance of this "capacitor". The Cole-Cole model was used again to fit the measured complex capacitance, and figure 3.11 shows that the real part of C^* is fitted very well up to 10 kHz. The imaginary part of $C^* = -G/\omega$ is not shown because it is too small to have a significant influence on the transfer impedance. The relative permittivity ε_r associated with this C^* ranges from 4.7 to 3.8. The associated Cole-Cole parameters are $\varepsilon_0 = 4.79$, $\varepsilon_\infty = 3.36$, $\tau = 2.8\ 10^{-5}$ s, and $\alpha = 0.54$.

Capacitive coupling depends on the electrical conductivity distribution. However, this distribution is not known a priori, which means that a correction for capacitive coupling errors in the measured transfer impedances cannot be done as easily as for the errors associated with inductive coupling. We propose to consider capacitive coupling by integrating capacitances between the relevant nodes and ground in the electrical network of the forward model describing the measurement environment using the finite element method (FEM). With this enhanced electric modeling approach, we can estimate the electric potential distribution depending on the complex conductivity of the elements in the mesh

and on the capacitive coupling (figure 3.12). For more details about the relationship between the FEM modeling and the electrical network representation we refer to Zimmermann (2011).

To test this method to correct capacitive coupling, we first apply it to the rain barrel measurements presented in figure 3.8. Because the measurement set-up is axisymmetric, it is sufficient to use a 2D FEM mesh for the electrical forward model (figure 3.12). The electric field distribution does not depend on the circumferential axis, so that the 3D cylindrical coordinate system can be simplified to an r-z (radius and height) 2D coordinate system. The FEM modeling for such an axisymmetric case is a simple extension of 2D FEM modeling for a plane where the 2D electrical conductivity is multiplied by the circumference (see Kwon and Bang 1997). We modified the modeling tools presented in detail in Zimmermann (2011) to simulate such axisymmetric modeling domains.

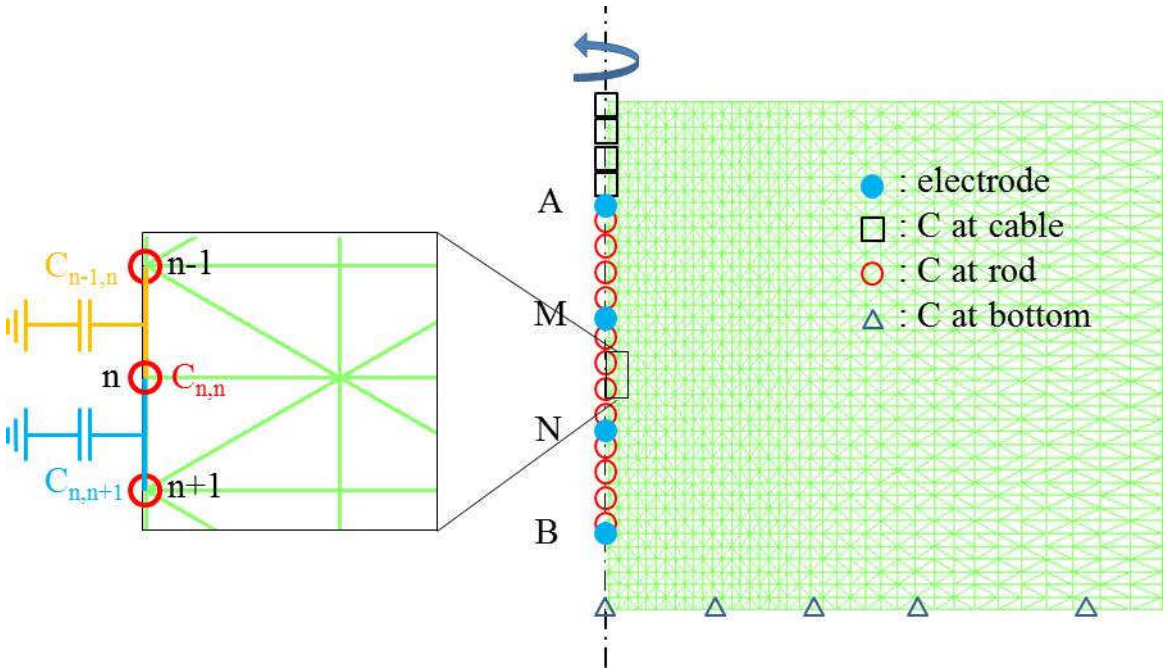

Figure 3.12: 2D-mesh of the rain barrel with integrated capacitances (dimension of the mesh: 1.37 m high, 0.35 m wide).

The challenge now is to integrate capacitances in the FEM mesh wherever capacitive coupling takes place (see figure 3.12). The most important type of capacitive coupling occurs between the cable and water, as described above. Additionally, there is capacitive coupling between the logging tool and water, between water and ground, and between electrodes and ground (due to the internal electronics). All these capacitances are connections between the nodes of the FEM mesh and ground. The FEM modeling is based on the Poisson's equation (see e.g. Pelton *et al.* 1978)

$$\nabla \cdot (\sigma \nabla \phi) = I\delta(r), \tag{3.21}$$

which should be discretized and solved numerically. σ is the complex electric conductivity, ϕ is the electric potential at each node, and $I\delta(r)$ is the punctual current injection (A and B in figure 3.12). In order to model the capacitances, a thin layer with zero-potential on one side (Dirichlet boundary condition) and with the permittivity and dimensions of the capacitances can be implemented. Since it is reasonable to assume that there is only current flow across and not along the thin layer, we can simplify the modeling of the thin capacitive layers with discrete capacitances between the concerned nodes and ground. Additionally, we assume that no electric current flows across the boundaries of the FEM mesh in figure 3.12 (Neumann boundary condition). In addition, the capacitance between cable and water is calculated with (3.18) and a frequency-dependent dielectric permittivity for PVC as described by the fitted Cole-Cole model discussed above (*C = 500 pF* at low frequency). The capacitance between the logging tool and the water is modeled as a cylindrical capacitor with three layers (rigid PVC, air, and flexible PVC as illustrated in figure 3.13). The capacitance for such a configuration can be calculated with (Plaßmann and Schulz 2009)

$$C = \frac{2\pi\varepsilon_0 l}{\frac{1}{\varepsilon_{r_1}}\ln\frac{r_2}{r_1} + \frac{1}{\varepsilon_{r_2}}\ln\frac{r_3}{r_2} + \frac{1}{\varepsilon_{r_3}}\ln\frac{r_4}{r_3}}, \tag{3.22}$$

where ε_{ri} and r_i are the relative dielectric permittivity and the radius of each layer (figure 3.13) (*C = 40 pF*). The capacitance between water and ground is calculated with the equation for the parallel plate capacitor:

$$C = \frac{\varepsilon_0 \varepsilon_r A}{d}, \tag{3.23}$$

where *A* is the area, *d* is the thickness of the rain barrel bottom, and ε_r is the permittivity of polyethylene (*C = 440 pF* with *A = 0.36 m²*, *d = 0.022 m*, ε_r *= 3*). Finally, the capacitance of the potential electrode comes from the amplifier at each electrode module. The input capacitance is about 50 pF.

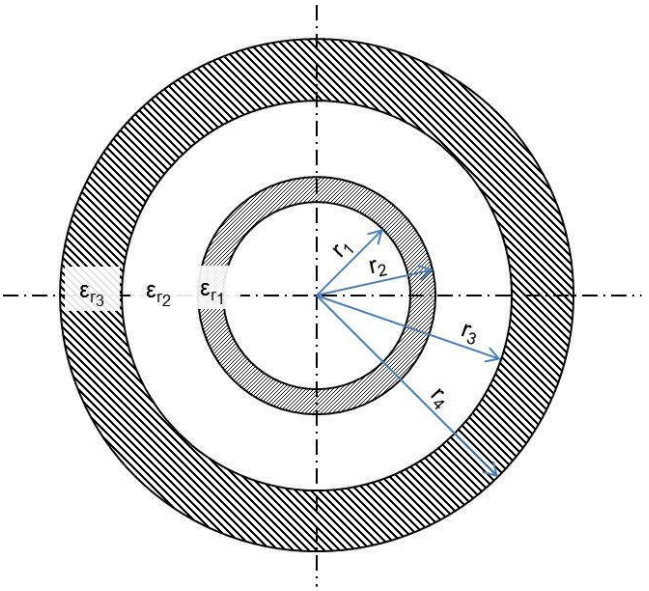

Figure 3.13: Cross-section of the electrode rod (three insulation layers from inside to outside: 1: flexible PVC, 2: air, 3: rigid PVC) with ε_{r1} = 4.5, ε_{r2} = 1.0059, ε_{r3} = 3, r_1 = 7.25 mm, r_2 = 8.75 mm, r_3 = 15 mm, r_1 = 21 mm.

The four types of capacitances were integrated into the FEM mesh as shown in figure 3.12. Three types of capacitances were integrated into the nodes along the central axis, which reflect the 43 cm of cable (capacitances of the cable insulation) and the complete borehole logging tool in water (capacitances of the housing and the input capacitances of the electrodes). The final type of capacitance associated with the bottom of the barrel was placed at all the nodes at the bottom of the mesh where the capacitive coupling was not negligible due to the small separation between water and ground (i.e. grooves in the bottom of the rain barrel).

For each node in the FEM mesh where a capacitance is considered, the admittance *Y* is calculated with

$$Y_{C_{n,n}} = i\omega C_{n,n}\,, \tag{3.24}$$

where $C_{n,n}$ is the capacitance assigned to node *n* of the mesh. In practice, $C_{n,n}$ is calculated by summing the half capacitances of the two neighboring edges (see figure 3.12):

$$C_{n,n} = \frac{1}{2}C_{n-1,n} + \frac{1}{2}C_{n.n+1} \tag{3.25}$$

and

$$C_{n-1,n} = C_{1m} \cdot l_{n-1,n}\,, \tag{3.26}$$

where $C_{n-1,n}$ is the capacitance of the edge between the nodes *n-1* and *n* (same for $C_{n,n+1}$), C_{1m} is the calculated capacitance (equations 3.18, 3.22, 3.23 and the input capacitance from the amplifiers) normalized to one meter, and $l_{n-1,n}$ is the length of the edge. For all nodes with associated capacitances, the admittances are assembled in a diagonal matrix:

$$\left[Y_{C_{n,n}}\right]=\begin{bmatrix} Y_{C_{1,1}} & \cdots & 0 \\ \vdots & Y_{C_{x,x}} & \vdots \\ 0 & \cdots & Y_{C_{n,n}} \end{bmatrix}, \tag{3.27}$$

where the subscript *n* stands for the number of the node. The admittance matrix of the whole mesh is given by

$$\left[Y_G\right]=\left[Y_S\right]+\left[Y_{C_{n,n}}\right], \tag{3.28}$$

where Y_S is the admittance matrix for the original mesh. According to Ohm's law, the potential at every node can be obtained with

$$\left[U\right]=\left[Y_G\right]^{-1}\vec{I}\ , \tag{3.29}$$

where *U* is a matrix with all node potentials, and *I* is a vector with all node currents. The voltage $U_{M,N}$ between two arbitrary nodes (e.g. *M* and *N* in figure 3.12) can be found by calculating the difference of their potentials from *U*. Thus the transfer impedance between two nodes (M and N) for a current injection at A and B can be obtained by

$$Z_{M,N} = U_{M,N}/I_{A,B}. \tag{3.30}$$

The results of this FEM model applied to the rain barrel are compared with the transfer impedance corrected for inductive coupling in figure 3.14, where the measured transfer impedance Z_{CR} after the correction of inductive coupling and the modeled transfer impedance Z_C including capacitive coupling are presented in green asterisks and blue solid curves, respectively. It can be seen that there is an excellent agreement between corrected and modeled transfer impedances both for the imaginary part and the phase angle (figure 3.14b and 3.14c). A small difference of about 0.7 Ω was observed between the real part of the modeled and corrected transfer impedance (figure 3.14a), which is most likely related to geometrical errors in the FEM modeling (e.g. inaccurate electrode positions) that are not critical for the phase accuracy. Considering all possible error sources in the measurements and the modeling, the deviation in the phase angle (0.8 mrad at 10 kHz) is very small and fully satisfactory (figure 3.14c). This high phase accuracy could only be obtained with the newly developed correction methods because of the well-known conditions in the rain barrel measurements. For field EIT measurements, it will be difficult to reach this high phase accuracy because of the less controlled conditions.

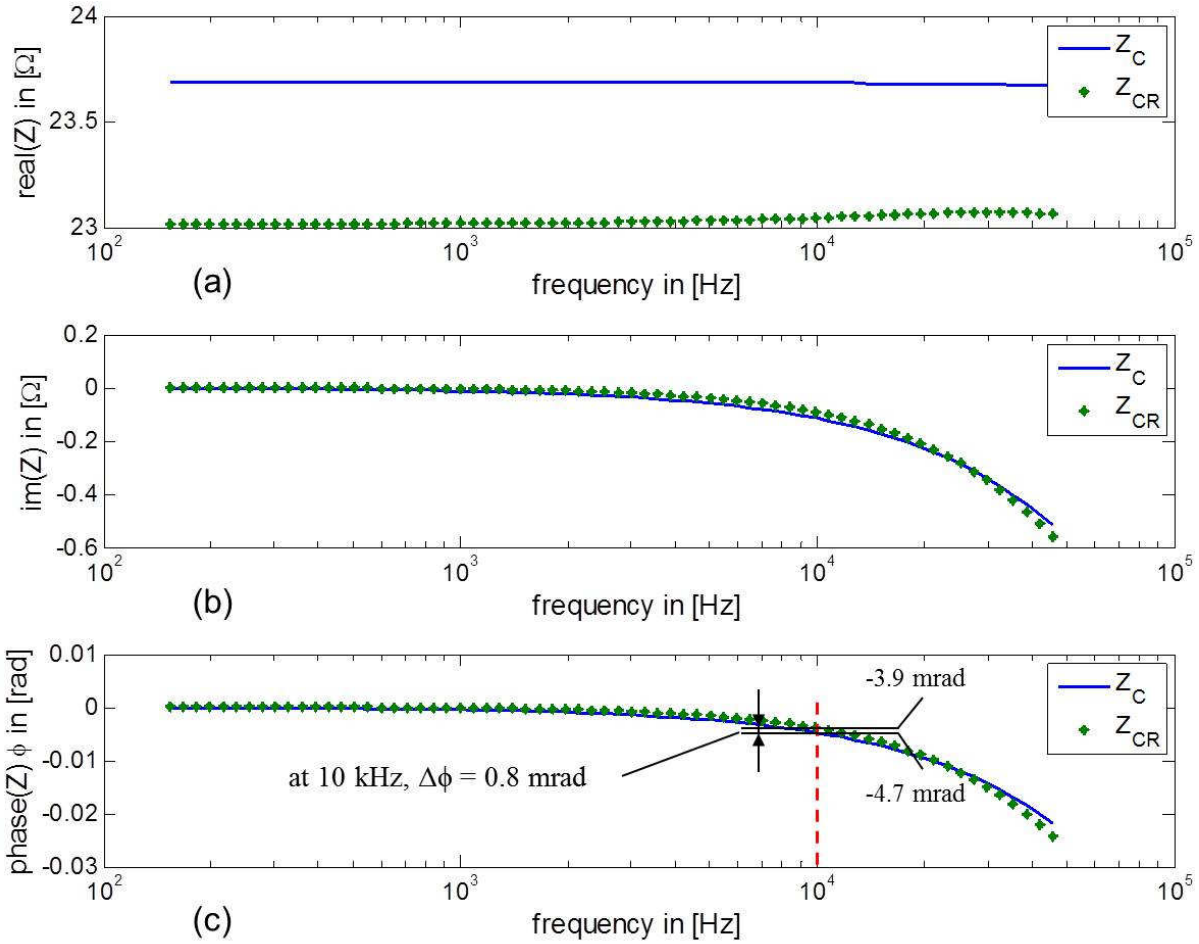

Figure 3.14: Comparison of the impedance corrected for inductive coupling, Z_{CR}, and the modeled impedance Z_C.

It is important to note here that the effect of capacitive coupling on the measured transfer impedance is relatively small in the case of the rain barrel measurements (about 3 mrad, see figure 3.14). The capacitive effect will be much stronger in field measurements because more cable will be in the water. For example, the simulated phase angle due to capacitive coupling in the field (see next section) using a Wenner measurement configuration with electrodes at 4.5 m, 5.5 m, 6.5 m and 7.5 m depth is 10.9 mrad at 10 kHz.

3.5 Application to borehole EIT measurements with an electrode chain

To illustrate the impact of the corrections for inductive and capacitive coupling for EIT field measurements, we present inversion results of borehole EIT measurements made with the electrode chain with 8 electrodes at the test site Krauthausen, Germany (Kemna *et al.* 2002; Müller *et al.* 2010). The ground water table was located at 2.5 m below the surface at the

time of the measurements (figure 3.15a). The uppermost electrode was placed 20 cm under the water table at a depth of 2.7 m and thus the lowermost electrode was placed at 9.7 m depth. The depth of the borehole was about 11 m. For current injection, we used all possible electrode configurations for skip-0 (1 2, 2 3…), skip-2 (1 4, 4 7…), skip-4 (1 6, 2 7, 3 8) and some configurations for skip-6 (1 7, 2 8) and skip-7 (1 8). For the voltage measurements we used the same electrode pairs except those including current electrodes (e.g. 1 2 4 7, 2 3 1 4, 1 7 2 3), and the corresponding reciprocal measurements (e.g. 4 7 1 2, 1 4 2 3, 2 3 1 7).

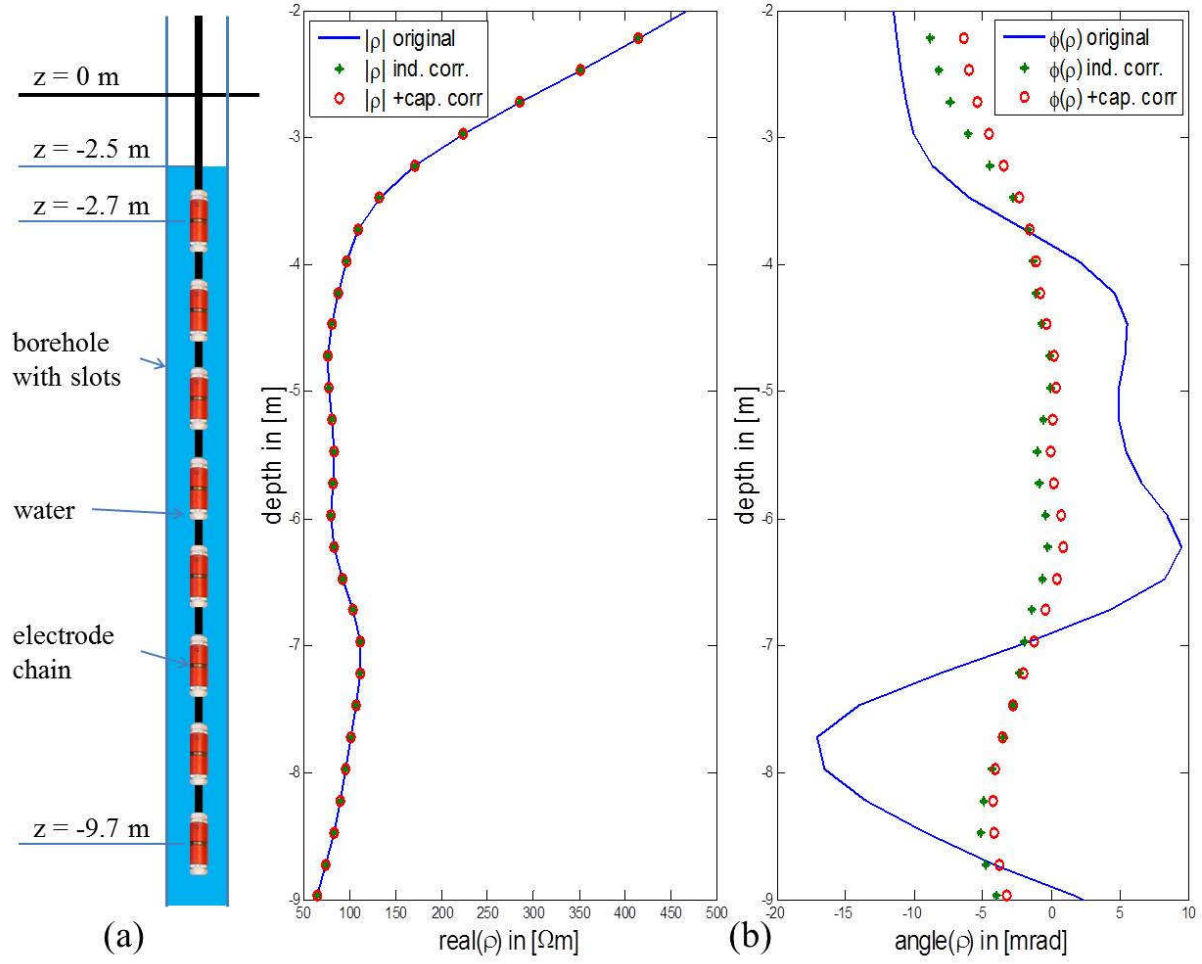

Figure 3.15: (a) Measurement setup, (b) Reconstructed real component and phase angle of the complex resistivity against depth at 1kHz for the raw EIT measurements, the EIT measurements after correction for inductive coupling, and an inversion that considers parasitic capacitances in the forward model.

Prior to the inversion, we corrected the inductive errors by determining $i\omega M$ (3.16) for all electrode configurations with the same calibration method used for the logging tool (figure 3.5). We also considered capacitive coupling in the forward modeling with a similar but larger 2D mesh (15 m by 5 m) as presented in figure 3.12. In this mesh, we integrated two

kinds of capacitances. The first one is the frequency-dependent capacitance between the cable isolation and the soil. This capacitance was obtained from (3.18) and the length of the electrode chain and amounted up to 11,000 pF in the low frequency range. The second type of capacitance is the input capacitance at the electrode amplifier, which has the same value of 40 pF as used for the logging tool. The capacitance of the PVC housing of the electrodes was neglected because it is small in comparison to the cable capacitance.

In order to see the effect of the correction procedures in the reconstructed real part and phase angle of the resistivity, three different inversions were performed using i) the original FEM forward model with raw measured data, ii) the original model with data corrected for inductive coupling, and iii) the original model with integrated capacitances and data corrected for inductive coupling. The inversion strategy was based on the Gauss-Newton method with Tikhonov regularization (see e.g. deGroot-Hedlin and Constable 1990; Kemna *et al.* 2000; and Zimmermann *et al.* 2008). The complex conductivity distribution was reconstructed in z-direction only because stratified sediment was assumed. The conductivity distribution in z-direction, starting with a homogeneous profile, was assigned to the elements of the 2D-mesh of the forward model in each inversion step. The regularization was applied to the z-direction to obtain a smooth profile and to stabilize the reconstruction.

Figure 3.15b presents inversion results for the 1D complex conductivity distribution in *z*-direction that were obtained using the inversion software presented in Zimmermann (2011). The inversion was performed for a frequency of 1 kHz because inductive and capacitive coupling are known to be strong there. In a first step, the raw EIT measurements were inverted. This resulted in relatively large phase values that even included physically implausible positive values for some depths. A similar behavior was already observed in the controlled test measurements (see figure 3.9). In a second step, the raw EIT measurements were corrected for inductive coupling and the inversion was repeated. This resulted in lower and entirely negative phase values. It can be seen that the two inversion results differ considerably, exhibiting positive and negative corrections that can be as large as 10 mrad. In the final inversion, capacitive coupling was considered by introducing the parasitic capacitances in the forward model. This resulted in a positive phase shift for the whole profile with a maximum phase increase of 3 mrad at 2 m depth. As expected, the inverted profiles for the real part of the resistivity were not affected by the corrections for inductive and capacitive coupling.

The final profile of phase values corresponds well with the profile expected from the stratigraphy at the test site (Kemna *et al.* 2002). The strong increase in resistivity magnitude and the more negative phase at the top of the profile is associated with the unsaturated zone (e.g. Jougnot *et al.* 2010; Breede *et al.* 2011; Breede *et al.* 2012). The more negative phase at the bottom of the profile is due to layers with higher clay content, whereas the smaller phase values in the middle of the profile are associated with gravel layers with less clay. At a depth of about 6 m, we obtain a small positive and, therefore, physically implausible phase of about 0.9 mrad. However, this obvious error is within the targeted accuracy of 1 mrad at 1 kHz for field measurements.

3.6 Conclusions and Outlook

We presented approaches to correct EIT measurements for inductive coupling between the current and the potential wires inside a multi-core cable and capacitive coupling between the cable and the electrically conductive environment. In order to verify these correction approaches, we performed EIT measurements in a rain barrel filled with water using a borehole EIT logging tool. For these controlled conditions, a high phase accuracy of about 0.8 mrad at 10 kHz was achieved. Additionally, we performed borehole EIT measurements at the Krauthausen test site using a borehole electrode chain to demonstrate the improvements that can be achieved with the correction approaches. Inverted resistivity magnitude and phase profiles considering both corrections matched well with the general stratigraphy of the test site.

There are three main limitations of the developed correction methods. First, the wire geometry needs to be known and stable in time. If the wire positions cannot be determined accurately or when they are not fixed, the calculation of the mutual inductances or the short-circuited calibration cannot be applied. Second, the available frequency range is constrained by all kinds of unknown noise from the environment. The third limitation is due to the wave length of the signal which should be large in relation to the cable length. Therefore, the frequency is limited to some kHz for our applications.

The proposed methods to account for inductive and capacitive coupling are not restricted to the custom-made EIT data acquisition system used in this study. They are also applicable to phase measurements with commercial EIT devices that rely on long multi-core cables. The developments in this contribution focused on current injection and potential measurements in a single borehole. In the next chapter, these methods will be extended to also consider cross-borehole EIT measurements where inductive coupling can also occur

between two cables (i.e. electrode chains with several meters separation). In such cases, the inductive coupling will be determined by the cable layout. This means that an alternative calibration strategy will be required and that the calculation of the mutual inductance will need to consider arbitrary cable geometries (e.g. using (3.7) instead of (3.8)). Finally, the impact of the secondary magnetic field from the sediment should also be considered. In contrast, the approach to account for capacitive coupling developed here is directly applicable to the cross-borehole case because there will be no capacitive coupling between two electrode chains in two different boreholes.

4 Phase correction of electromagnetic coupling effects in cross-borehole EIT measurements *

4.1 Introduction

EIT borehole field measurements in two boreholes should be discussed in this chapter and the electromagnetic coupling effect should be investigated, which cannot be calibrated as described in chapter 3, because the inductive coupling in this case is also dependent on the cable layout in the field measurement. The theoretical calculation of EM coupling between grounded wires on the surface of the earth has previously been treated in some detail (e.g. Sunde 1968, Wynn and Zonge 1977, Wait 1984 and Ward and Hohmann 1988). In these contributions, the mutual impedance that represents the total response from the earth and the wires was split into two parts. The first part describes the complex electrical resistivity of the earth and the second part describes the inductive coupling between the electrical wires, which only depends on the geometry of the wire layout. However, the main problem with the application of these theoretical approaches to borehole EIT measurements is the need to know the position of adjacent wires in borehole electrode chain with sufficient accuracy. In previous work, we solved this problem for measurements with a single borehole electrode chain using a method based on calibration measurements (Zhao *et al.* 2013). This calibration must be done only once because it does not depend on the cable layout of the field measurement.

EM coupling in cross-hole EIT measurements with multiple borehole electrode chains was not yet considered in great detail. In this case, inductive coupling cannot be corrected by only using calibration data because the coupling between different electrode chains depends on the cable layout of the field measurement. This part of the inductive coupling must be calculated for each measurement. To improve applicability of corrections of inductive coupling, there clearly is a need for an effective framework to jointly consider calibration measurements and numerical calculations based on cable geometry to correct EIT measurements with arbitrary electrode configurations using one or multiple borehole

* Adapted and modified from Zhao Y, Zimmermann E, Huisman J A, Treichel A, Wolters B, Waasen S v and Kemna A. 2015. Phase correction of electromagnetic coupling effects in cross-borehole EIT measurements. *Meas. Sci. Technol.,* **26** 015801

electrode chains. Thus, it is aimed to i) characterize inductive coupling in cross-borehole EIT measurements with multiple electrode chains and ii) develop an efficient correction procedure that combines calibration measurements and numerical modelling to obtain accurate cross-borehole EIT measurements. In order to verify the extended correction procedures, EIT measurements were performed under controlled conditions in a water-filled pool. In addition, the correction procedures were applied to actual borehole EIT measurements.

4.2 Borehole EIT measurement setup

The EIT system used in this study is an extension of the EIT laboratory system (Zimmermann *et al.* 2008; Zimmermann *et al.* 2010) that was designed to make accurate impedance measurement using two electrodes for current injection and two electrodes for potential measurement. The system has 40 channels that can be used for current injection and potential measurement at each electrode. To achieve this, each channel is connected with a multi-functional electrode module that consists of an integrated relay for current injection and an amplifier for potential measurement. In order to make borehole EIT measurements, electrode chains with 8 electrode modules and an electrode separation of 1 m were built. The electrode modules are connected to an adapter box close to the EIT data acquisition system using a 25 m long multi-core cable that consists of 16 shielded, twisted wire pairs. To ensure a good electric contact with the surrounding medium, we used brass ring electrodes with a diameter of 42 mm and a height of 10 mm (Zhao *et al.* 2013).

The system can be used for field EIT measurements with two or more borehole electrode chains and all possible electrode configurations can be measured. For the purpose of characterizing inductive coupling, electrode configurations can be divided into two general cases (figure 4.1). In the first case, the current electrodes and the potential electrodes are located in the same borehole (figure 4.1a). In the second case, one or more of the current and potential electrodes are placed in a different borehole. Electrode configurations of the second type include cross-borehole dipole-dipole configurations (figure 4.1b), unconventional electrode configurations with one electrode in a different borehole (figure 4.1c), and classic cross-borehole electrode configurations with current and potential electrodes in both boreholes (figure 4.1d). Because of the relatively long electrical wires used in borehole EIT measurements, electromagnetic coupling effects that substantially reduce the measurement accuracy are expected in both cases. In the next sections, the inductive coupling effect and the capacitive coupling effect will be addressed separately and the phase correction procedures will be shown.

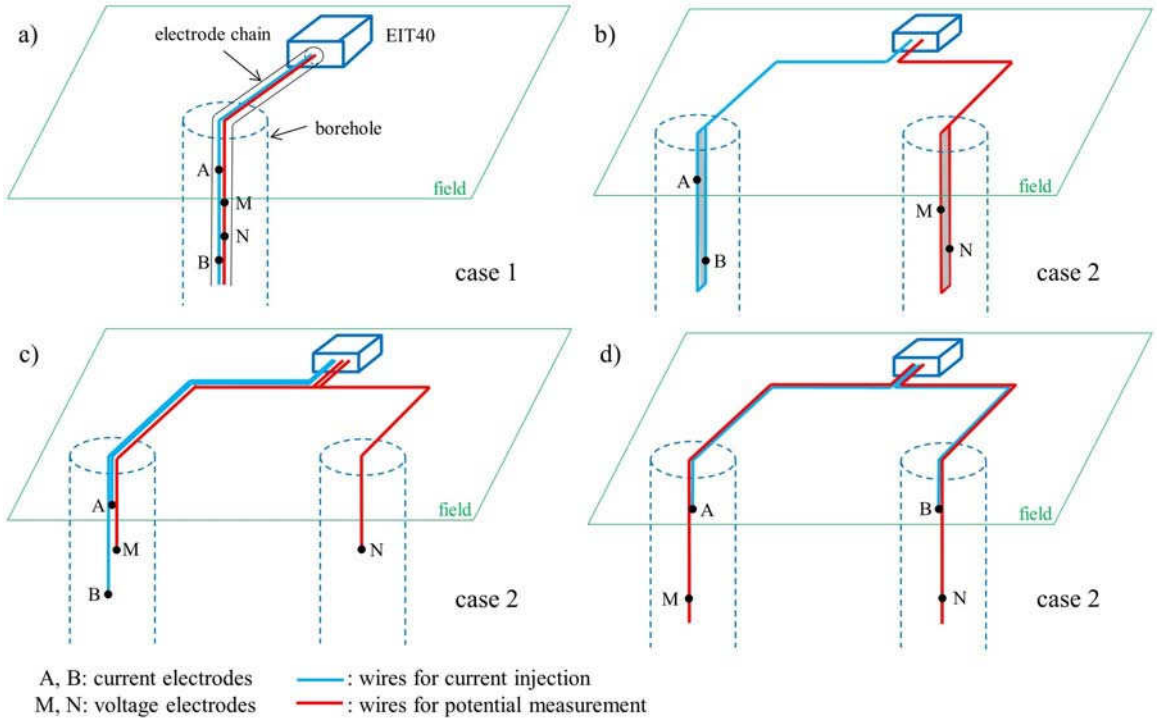

Figure 4.1: Case classification of the EIT borehole field measurements (a: single borehole measurement; b, c, d: cross-borehole measurements).

4.3 Inductive coupling in borehole EIT measurements involving two boreholes

4.3.1 Electromagnetic response from the subsurface

The inductive response from the subsurface during EIT field measurements comprises two parts. The first part consists of the electromagnetic response of the subsurface itself, which depends on the complex electrical resistivity distribution. The second part is associated with the magnetic field caused by the inductive coupling between the wire pairs for current injection and potential measurement. For a homogenous subsurface, the measured mutual impedance Z_m between the current and potential wires placed on the Earth surface is given by Sunde (1968):

$$Z_m = \frac{U}{I} = \int_{C_1}^{C_2}\int_{P_2}^{P_2}\frac{\partial^2 Q(r)}{\partial s \partial S}\,dsdS + \int_{C_1}^{C_2}\int_{P_1}^{P_2} P(r)\cos\varepsilon\,dsdS\,, \tag{4.1}$$

where $Q(r)$ is the grounding function that describes the response from the soil, C_1, C_2, P_1 and P_2 are the start and end positions of wires for current injection and potential measurement, respectively, s and S are the line elements of the wires and ε is the angle between them. The inductive contribution is described by $P(r)$ and consists of the primary and secondary magnetic field:

$$P(r) = \frac{i\mu\omega}{2\pi r}\left[\frac{1-(1+\gamma r)e^{-\gamma r}}{(\gamma r)^2}\right], \tag{4.2}$$

where *i* is the imaginary unit, μ is the permeability, ω is the angle frequency, *r* is the distance between the wires and $\gamma = (i\sigma\mu_0\omega)^{1/2}$ is the eddy current constant. The limit of (4.2) for small γ is the cable coupling

$$P^0(r) = \frac{i\mu\omega}{4\pi r}, \tag{4.3}$$

which only depends on the cable geometry and the frequency. In order to obtain a worst-case estimate for the influence of inductive coupling on the measured mutual impedance, the quotient between (4.2) and (4.3) was calculated for a frequency of 1 kHz, an electrical conductivity of σ = *0.01 Sm*$^{-1}$, and a separation between the wire segments of *r = 10 m*. The selected electrical conductivity corresponds with the highest value observed at the demonstration site Krauthausen (Vereecken *et al.* 2000; Kemna *et al.* 2002; Müller *et al.* 2010). The maximum separation of 10 m was based on the typical borehole separations considered in field EIT studies. Using these values, the quotient *P/P*^{0} is *0.9581 - i0.0399*. The imaginary part of *P* has the biggest effect on the phase of the measured resistivity of the soil, which is related to the real part of *P/P*^{0}. Because Re(*P/P*^{0}) is close to one, the influence from the subsurface is very small and it is justified to use equation (4.3) instead of the more complex equation (4.2) for typical borehole EIT applications.

Sunde (1968) also provided the two terms *Q(r)* und *P(r)* in (1) for a stratified subsurface:

$$\begin{aligned} Q(r) &= Q^0(r) + i\omega L^0(r) \\ P(r) &= P^0(r) + P_0(i\omega) \end{aligned}, \tag{4.4}$$

where $Q^0(r)$ reflects the resistivity of the soil, and $L^0(r)$ is the earth-return inductance. $L^0(r)$ can reach a maximum value of $\mu r/4\pi$, which amounts to *1e-6 H* for *r = 10 m* (Sunde 1968). This is still negligibly small compared to the primary mutual inductance of the wires $P^0(r)/i\omega$ described in (4.3), which is at least one order of magnitude larger. The correction term $P_0(i\omega)$ due to the frequency-dependent current distribution in the earth also is very small and can be neglected according to Sunde (1968). Since the inductive effects associated with the subsurface were found to be small and negligible, it will be focused on the characterization and correction of the inductive coupling between the electrical wires. This means that for the correction of inductive effect only the part $P^0(r)$ must be considered which is described in (4.3).

4.3.2 Inductive coupling between electrical wires in two boreholes

The measured transfer impedance Z_m can be calculated using (Zhao *et al.* 2013):

$$Z_m = \frac{U}{I} = Z_{soil} + i\omega M \ , \tag{4.5}$$

where Z_{soil} is the subsurface impedance of interest, and $i\omega M$ describes the inductive cable coupling that needs to be removed from the measured data. The mutual inductance for arbitrary wire geometries can be calculated with the Neumann's integral (see e.g. Henke 2011):

$$M = \frac{\mu}{4\pi} \int_{C_1}^{C_2} \int_{P_1}^{P_2} \frac{d\vec{s}\, d\vec{S}}{r} \ , \tag{4.6}$$

where *s* and *S* are the infinitesimal segments of the current and potential wires and *r* is the distance between them. The integral paths are defined by the current electrodes C_1, C_2 and the potential electrodes P_1, P_2, respectively.

In order to derive *M* using (4.6), we must know the geometry of the wire positions exactly. Because of the small distances between the wires and the parasitic eddy currents in the shield of the electrode chain, it is very difficult to calculate the inductance *M* from the geometry for borehole EIT measurements with current injection and potential measurement in a single borehole chain (figure 4.1a). However, it is possible to use calibration measurements to remove the inductive coupling for this case since the wires are fixed inside one multi-core cable (Zhao *et al.* 2013). For the second case, the inductance now also depends on the layout of the two multi-core electrode chains at the Earth's surface, which obviously varies with the measurement location and depends on the position of the EIT system relative to that of the boreholes. We propose to numerically model this additional inductance using Neumann's integral (4.6). The challenge for correcting cross-borehole EIT measurements is now to develop an effective approach that combines the calibration measurements and numerical modeling to calculate the inductive coupling for cross-borehole measurements.

4.3.3 The pole-pole matrix

In order to realize an effective correction method for the mutual inductance of different electrode configurations, we propose to decompose the mutual inductance of an arbitrary electrode configuration by assuming that the inductances are passive linear (reciprocal) elements. Using this assumption, the mutual inductance of electrode configuration [C_1 C_2 P_1 P_2] can be decomposed according to

$$M_{C_1C_2P_1P_2} = (M_{C_1P_1} - M_{C_1P_2}) - (M_{C_2P_1} - M_{C_2P_2}) \, , \tag{4.7}$$

where the inductances on the right side of (4.7) denote the mutual inductances between the corresponding wires connected with the electrodes C_1, C_2, P_1 and P_2. The minus signs are due to the direction of the current flow and voltage within the two wire loops.

The advantage of the decomposition of the mutual inductance in (4.7) is that we can now formulate a pole-pole matrix that contains all mutual inductances for one electrode chain:

$$\boldsymbol{M}_{8x8} = \begin{bmatrix} 0 & M_{1,2} & \cdots & M_{1,7} & M_{1,8} \\ M_{2,1} & 0 & & M_{2,7} & M_{2,8} \\ \vdots & & \ddots & & \vdots \\ M_{7,1} & M_{7,2} & & 0 & M_{7,8} \\ M_{8,1} & M_{8,2} & \cdots & M_{8,7} & 0 \end{bmatrix}, \tag{4.8}$$

with $M_{C,P}$ being the mutual inductance between the two wires *C* and *P*, where wire *C* is used for current injection and wire *P* is used for potential measurement. The advantage of the pole-pole matrix becomes clear when the following example is considered. For a borehole chain with eight electrodes there are a total of 840 possible electrode configurations for a four-point measurement (two current electrodes and two potential electrodes) when reciprocal measurements are considered as well. If we additionally consider 17 frequencies during borehole EIT measurements, a total of 14,280 calibration measurements would be required to correct inductive coupling effects for all possible electrode configurations. Such a calibration would be time-consuming and ineffective. In contrast, the pole-pole matrix needs only *8*x*8*x*17* = *1.088* calibration measurements.

The pole-pole matrix for two chains is defined as

$$\boldsymbol{M}_{16x16} = \begin{bmatrix} \boldsymbol{M}^1 & \boldsymbol{M}^{12} \\ \boldsymbol{M}^{21} & \boldsymbol{M}^2 \end{bmatrix}, \tag{4.9}$$

where $\boldsymbol{M}^1$ and $\boldsymbol{M}^2$ are the pole-pole matrices of the first and second chain, respectively, and $\boldsymbol{M}^{12} = (\boldsymbol{M}^{21})^T$ is the pole-pole matrix with the mutual inductances between the wires of both chains. This matrix is symmetric due to reciprocity, i.e. $M_{C,P} = M_{P,C}$. In order to consider the frequency dependency of the mutual inductance, a pole-pole matrix is defined for each frequency independently.

4.3.4 Determination of the pole-pole matrix

To obtain the pole-pole matrices $\boldsymbol{M}^1$ and $\boldsymbol{M}^2$ in (4.9), we made pole-pole calibration measurements. For this, we short-circuited all electrodes and connected them to the mass of the EIT system (figure 4.2). Next, current was injected at one electrode, which flowed directly back to the ground of the EIT system because of the short circuit. Simultaneously, the voltages were measured at the remaining 7 electrodes. This process was repeated until

all electrodes were used for current injection. The quotient of the induced voltage and the injected current is related to the mutual impedance of the two wires, but is also affected by contributions from the ground connection used for the calibration measurement and will be referred to as additive inductances in the following. These additive inductances must be removed to correctly determine the mutual inductances required in (4.9).

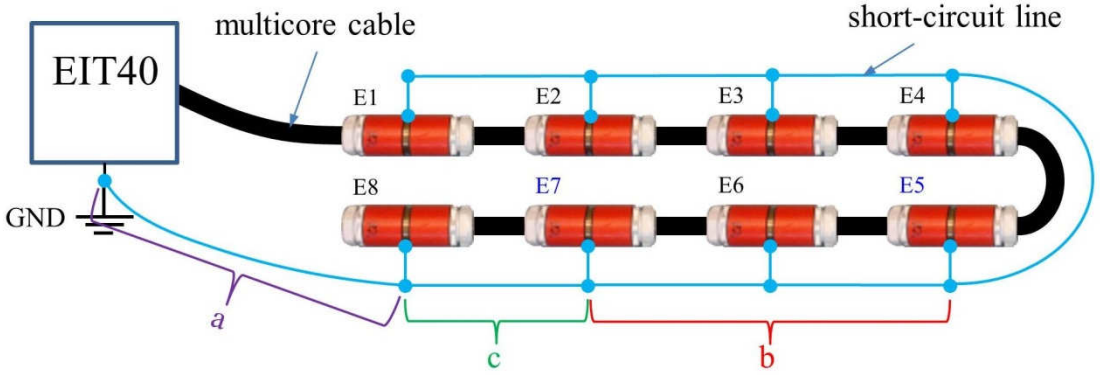

Figure 4.2: Pole-pole calibration measurement for electrode chain with 8 ring electrodes and 25 m long multi-core cable: one example for the configuration [5 7] with the segments a, b, and c of the short-circuit line related to the additive inductances.

The additive inductances consist of three components for the wire segments *a*, *b* and *c* in figure 4.2. The first inductance L_a is the self-inductance of the short-circuit line from the last electrode of the chain to the ground (segment *a*). The second inductance L_b represents the mutual inductance between the wires inside the cable and the short-circuit line for segment *b* between the used current and voltage electrode. The last term L_c represents the self-inductance of the short-circuit line for segment c between the last electrode and the next used electrode (current or potential). For measurements with one electrode chain, a large part of these additional inductances vanishes after calculation of the mutual inductance of the electrode configuration using (4.7). However, for cross-hole configurations these additional inductances cannot be neglected. Thus, to ensure universal applicability they should be determined and subtracted from the mutual inductances in the pole-pole matrix. The additive inductance for each pole-pole configuration with electrodes *m* and *n* can be determined from:

$$adL_{m,n} = L_a + |s_m - s_n| L_b + \min(s_m, s_n) L_c \,, \tag{4.10}$$

where s_m and s_n are distances from the last electrode (number 8) to the electrodes m and n normalized by the electrode separation. For the example in figure 4.2, the electrode configuration with current electrode 5 ($s_5 = 3$) and voltage electrode 7 ($s_7 = 1$) results in an additive inductance $adL_{5,7}$ equal to $L_a+2L_b+L_c$.

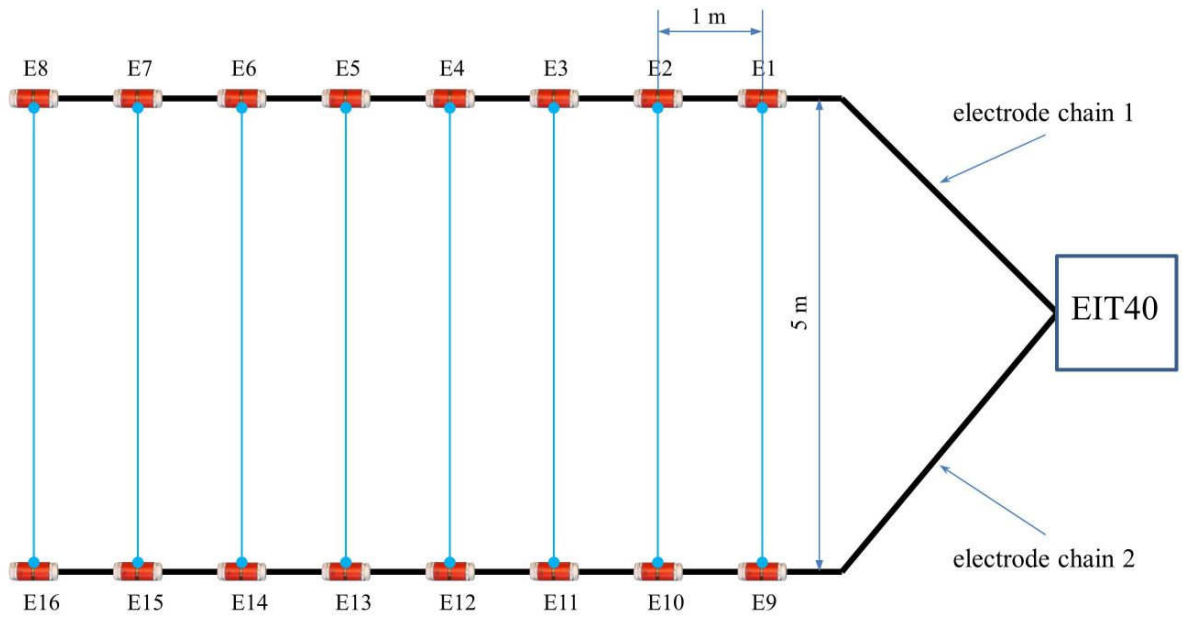

Figure 4.3: Measurement set-up for the calibration measurement with four-point configurations.

In order to separate the additive inductances from the mutual inductance of interest, a second calibration measurement was performed using two electrode chains with electrical connection between the chains (figure 4.3). In contrast to the first calibration measurement with pole-pole configurations, this second set of calibration measurements uses only four-point cross-hole configurations that are unaffected by the additive inductances in (4.10). In particular, we connected the electrode pairs [1 9], [2 10] ... [8 16] and used these pairs as current electrodes. The remaining electrode pairs were used as potential electrodes. In order to avoid leakage current into the subsurface, Styrofoam plates of 4 cm thickness were placed between the electrodes and the ground. We measured the transfer impedances in the frequency range of interest and transformed them into the measured mutual inductances using (4.7):

$$\begin{aligned} M^{m}_{C_1C_2P_1P_2} &= (M_{C_1P_1} + M_{C_2P_2}) - (M_{C_1P_2} + M_{C_2P_1}) + M_{EC} \\ &= (M^{m}_{C_1P_1} - adL_{C_1P_1}) + (M^{m}_{C_2P_2} - adL_{C_2P_2}) - (M_{C_1P_2} + M_{C_2P_1}) + M_{EC} \end{aligned}, \qquad (4.11)$$

where $M^{m}_{C_1P_1}$ and $M^{m}_{C_2P_2}$ are the inductances obtained from the first pole-pole calibration measurement. The terms $adL_{C_1P_1}$ and $adL_{C_2P_2}$ are the additive inductances described in (4.10) with the unknown parameters La, Lb, and Lc. The terms $M_{C_1P_2}$ and $M_{C_2P_1}$ are the mutual inductances between the wires of the two chains and the term MEC is the mutual inductance between the electrical connection and the wires of the electrode chains. As illustrated in figure 4.4, the terms $M_{C_1P_2}$, $M_{C_2P_1}$ and M_{EC} can be determined by solving (4.6)

using the finite segment method, where the electrode chains and the electrical connection were divided into many small segments in the longitudinal direction. With this discretization, the integral (4.6) was converted into a summation and numerically calculated using MATLAB. Equations (4.10) and (4.11) can now be used with a set of cross-hole configurations (all configurations of figure 4.5) to determine L_a, L_b and L_c, because all other terms are already obtained. Because we have three unknown parameters, at least three configurations are needed to solve the resultant system of equations. However, in practice all cross-hole configurations are used to evaluate the quality of the pole-pole matrix and the calibration measurements.

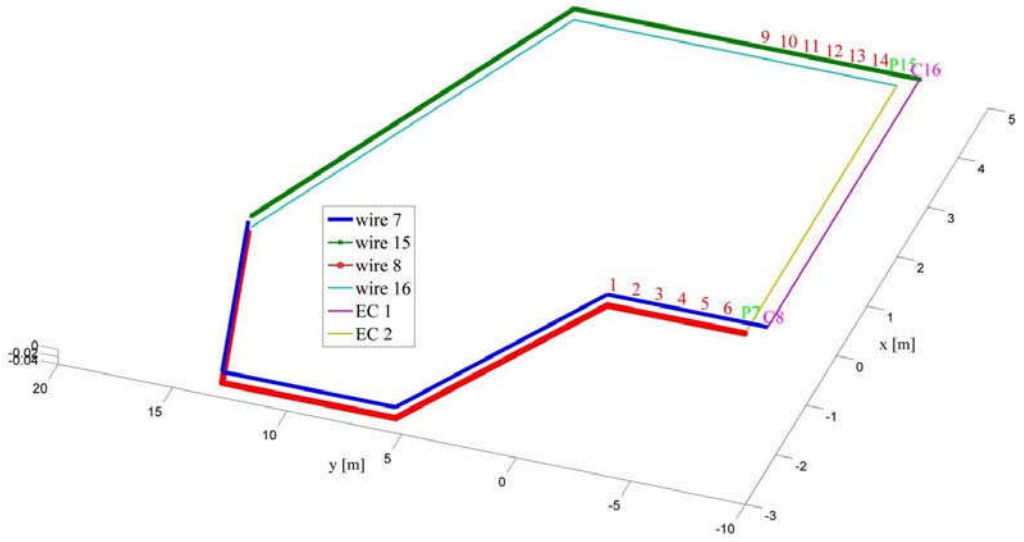

Figure 4.4: Segmented electrode chains for a sample configuration [8 16 7 15] using Matlab (1, 2, 3… 16: electrodes; C8, C16: current electrodes; P7, P15 potential electrodes; EC1, EC2: electrical connection).

After derivation of the additive inductances, all elements of the true pole-pole matrices $\boldsymbol{M}^1$ and $\boldsymbol{M}^2$ of the electrode chains can be calculated with (4.10) and

$$M = M^{m}_{m,n} - adL_{m,n} \,. \tag{4.12}$$

As long as the relative positions of the electrical wires in the multi-core cable do not vary with time, we only need to perform the calibration measurements once for each electrode chain. The cable layout geometry needs to be determined for each field EIT acquisition. In order to minimize the residual error after correction, we propose to use simple geometries for the cables from the system to the boreholes (e.g. triangles) so that accurate geometrical information can be obtained using a few positional measurements only.

To verify the pole-pole matrix of the mutual inductances, or rather the fitted inductances L_a, L_b and L_c, we compared the corrected mutual inductances for all electrode configurations

used in the second calibration with and without the consideration of the additive inductances (figure 4.5). It can be seen that the differences between the measured and calculated data M_{CR^*} without correction of the additive inductances are large. After consideration of the additive inductances, the measured and modeled mutual inductances match very well (deviation <2%). These results clearly illustrate the importance of considering the additive inductances in (4.10).

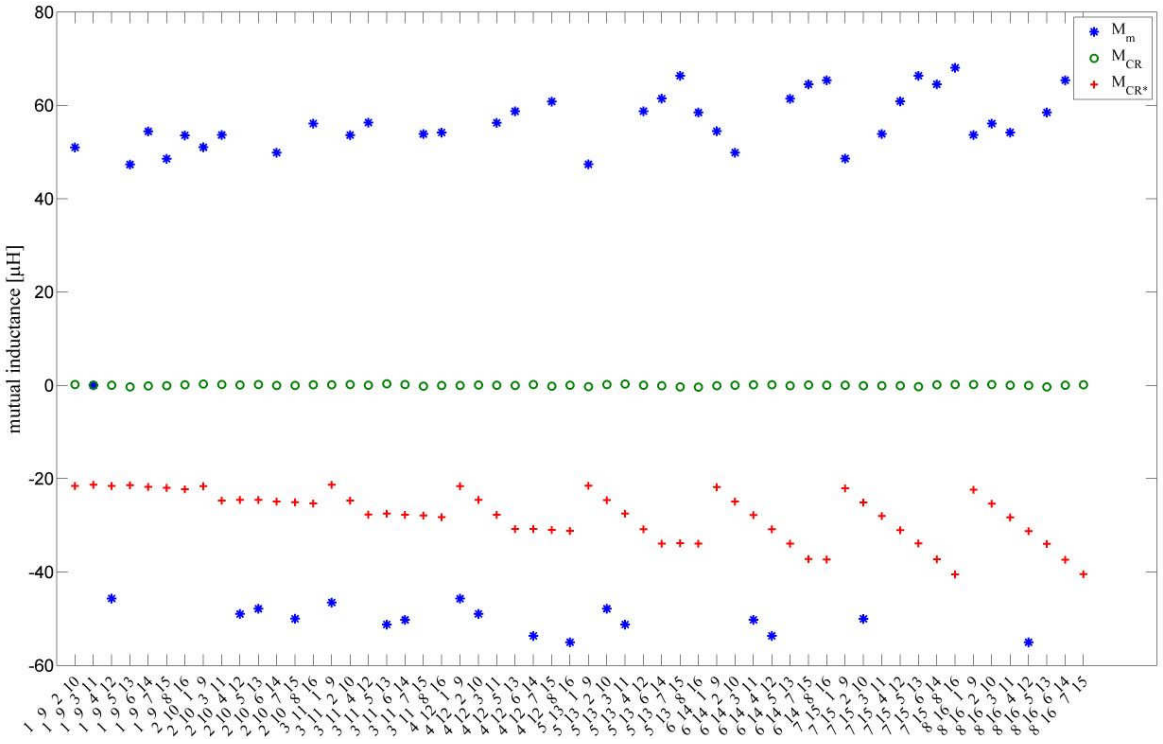

Figure 4.5: Comparison of the measured mutual inductance M_m (solid circles) and the calculated mutual inductance M_{CR} with (open circles) and M_{CR^*} without (crosses) correction of the additive inductances of the second calibration measurement.

To ensure a high accuracy of the determination of the inductances, we performed a sensitivity analysis to determine how much M changes with geometrical changes in the cable layout similar to figure 4.3 (cable length 25 m, cable separation of the parallel part 5 m, cable length of the parallel part 9 m). Table 4.1 shows that the deviation between the calculated and reference mutual inductance is about 0.74% for the configuration with the largest inductive coupling ([8 16 7 15]), if the geometrical error is 0.01 m. The error is still well below 5% for a geometrical error of 0.05 m. This sensitivity analysis clearly shows that the required positional accuracy to determine the cable layout is about 0.01 m, which is feasible in most field investigations.

Table 4.1: Comparison of the calculated mutual inductance M for the electrode configuration [8 16 7 15] by different offset of the cable geometry

Mutual inductance for configuration [8 16 7 15]		
geom. error	**calc. value**	**Deviation**
0 m	4.1445e-05 H	\
0.01 m	4.1139e-05 H	-0.74%
0.05 m	4.3123e-05 H	3.89%
0.1 m	4.7039e-05 H	11.89%
0.2 m	5.0382e-05 H	17.74%
0.5 m	5.4615e-05 H	24.11%

4.4 Capacitive coupling

Capacitive coupling occurs because of the potential difference between the conductive shield of the cable and the conductive subsurface and depends on the dielectric properties of the cable insulation. The geometry-dependent capacitance of the cable insulation was calculated using (Plaßmann and Schulz 2009):

$$C = 2\pi\varepsilon_0\varepsilon_r \frac{l}{\ln\frac{R_2}{R_1}}, \tag{4.13}$$

where ε is the vacuum permittivity, R_1 and R_2 are the inner and outer radius, and l is the length of the cable insulation. The relative permittivity ε_r of the cable insulation (PVC) was found to be frequency-dependent due to the slow reorientation of molecule groups with permanent dipole moment within such polymer materials (see e.g. Wagner 1914; Felger and Bassewitz 1986). Therefore, we used the Cole-Cole model (see. e.g. Cole and Cole 1941) to describe the complex dielectric permittivity using $\varepsilon_s = 4.79$, $\varepsilon_\infty = 3.36$, $\tau = 2.8\ 10^{-5}$ *s*, and $\alpha = 0.54$ (Zhao *et al.* 2013). This calculation is used to determine the capacitance of cable parts which are located in the water inside the borehole. Furthermore the capacitances of the integrated amplifiers inside the electrode modules are considered. For more details about the calculation of these capacitances we refer to Zhao *et al.* (2013).

These capacitances should be integrated in the forward modeling of the field EIT measurements in order to consider and remove the capacitive coupling effect. Such forward modeling can be realized using 2D or 3D meshes and the finite-element-method. The calculated capacitances C of the cables should be integrated in every node of the mesh where capacitive coupling is expected. The total admittance matrix of the forward problem (Zimmermann 2011) can be obtained by adding the capacitance matrix $\boldsymbol{Y_C} = i\omega\boldsymbol{C}$ to the original admittance matrix

$$\boldsymbol{Y}_T = \boldsymbol{Y}_S + \boldsymbol{Y}_C \,. \tag{4.14}$$

Using Ohm's law, we obtain the electric potential matrix for all nodes from

$$\boldsymbol{U} = \boldsymbol{Y}_T^{-1} \boldsymbol{I} \,, \tag{4.15}$$

The transfer impedance and its phase shift between any two nodes (M and N) for a current injection at any nodes A and B in the mesh is obtained by

$$Z_{M,N} = U_{M,N} \cdot I_{A,B} \,. \tag{4.16}$$

4.5 Verification of the correction methods

In order to verify the developed correction method for inductive coupling, we performed EIT measurements under controlled conditions in a swimming pool (figure 4.6). The pool is about 1 meter high and has a diameter of 4.5 meter. We placed the two electrode chains in the form of two overlapping rings with a diameter of 3.02 m and a chain separation of 0.5 m (figure 4.6c). The electrode chains were positioned using plastic floating bodies with linen strings (figure 4.6a and figure 4.6b). The pool was filled with tap water with an electrical resistivity of 23 Ω/m.

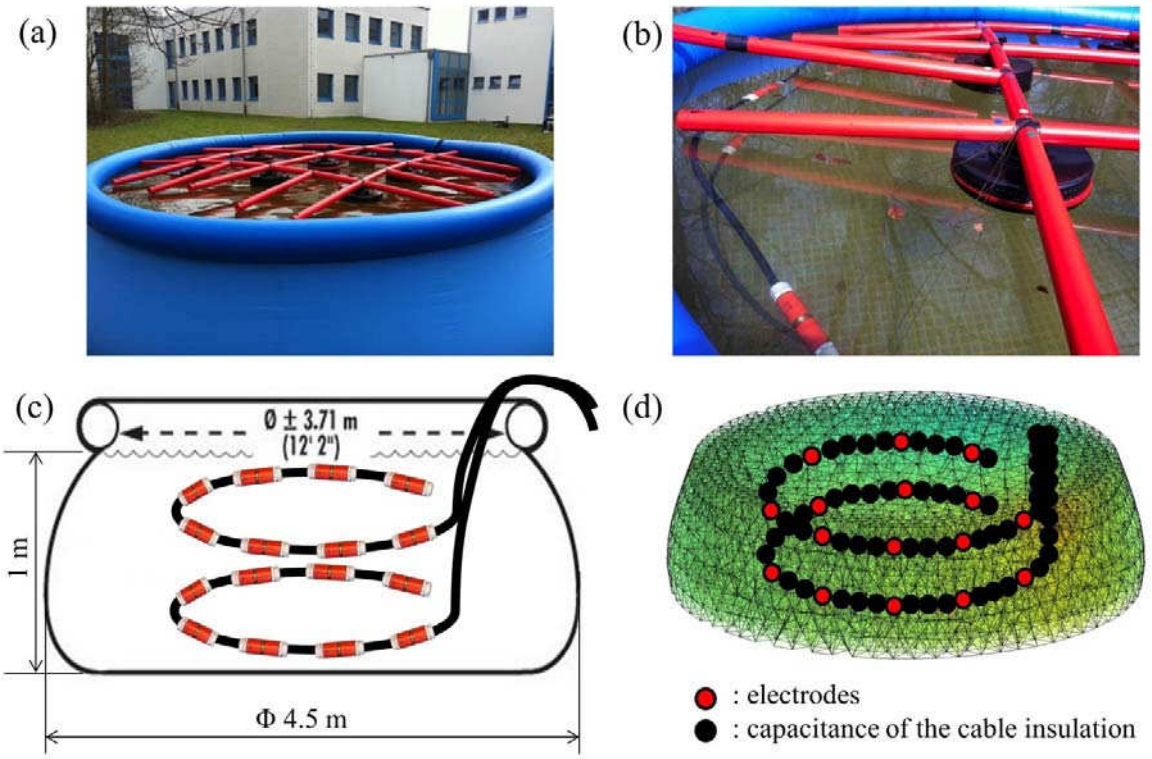

Figure 4.6: a) pool with floating body; b) fixation of the electrode chains; c) measurement set-up; d) numerical modeling with 3D finite-element mesh

The transfer impedance Z for different electrode configurations was measured using the field EIT system described above. Inductive coupling was removed from the measured impedance with the methods introduced in section 4 and the known geometry of the cables. In order to consider capacitive coupling, we generated a 3D mesh (figure 4.6d) with distmesh (Persson and Strang 2004) and calculated the admittance matrix $\boldsymbol{Y_s}$, which represents the admittances of water without capacitive effect. We determined the capacitance of the chains, the integrated amplifiers, and the water-ground interface at the bottom of the pool, and integrated them into the corresponding nodes of the 3D mesh (figure 4.6d). Using (4.14), (4.15) and (4.16), the theoretical transfer impedances Z_c was calculated for all electrode configurations used in the pool measurement.

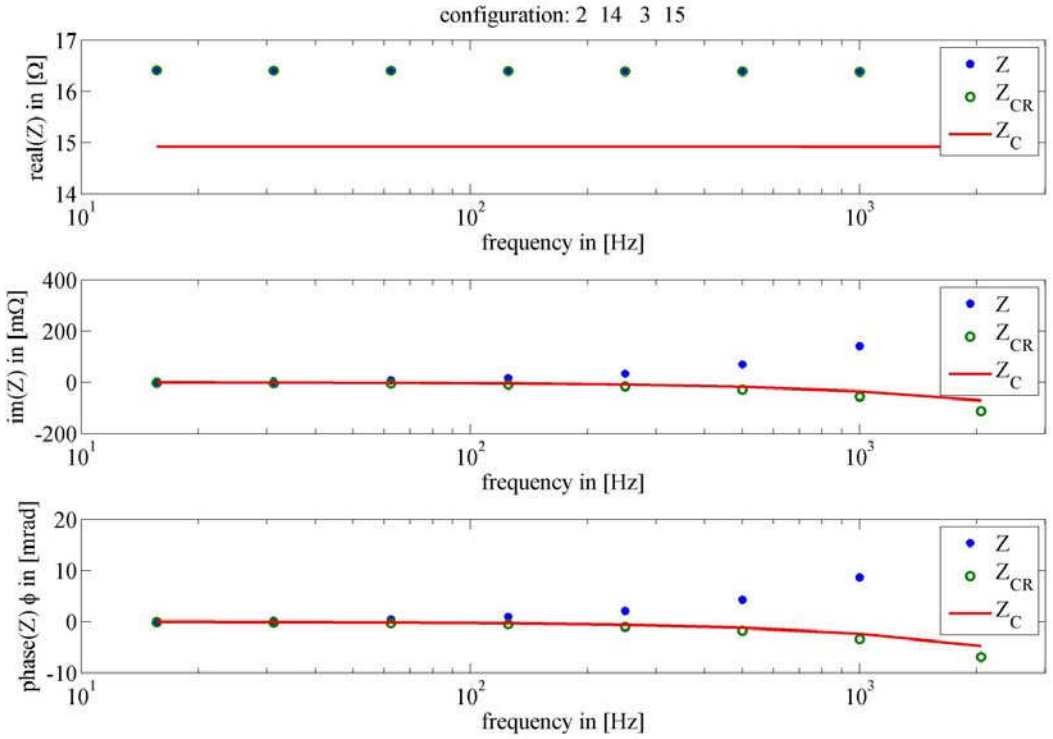

Figure 4.7: Comparison of the original measured impedance Z (solid circles) with error bars determined from the difference between reciprocal measurements, the impedance corrected for inductive coupling Z_{CR} (open circles), and the modelled impedance Z_C (curve) considering only the capacitive effects for an exemplary electrode configuration

Figure 4.7 compares the measured impedance Z, the measured impedance after correction of inductive coupling Z_{cr}, and the modeled impedance considering capacitive effects Z_c for a selected electrode configuration. The remaining phase shift after correction of inductive coupling is attributed to capacitive coupling, and therefore the corrected impedance Z_{cr} should match the modeled impedance Z_c. Figure 4.7 shows that this comparison indeed is satisfactory. For a typical cross-hole configuration, the phase error between the corrected impedances and the modeled impedances is around 1 mrad at 1 kHz ($\varphi(Z_{cr})$ = -3.4 mrad,

$\varphi(Z_c)$ = -2.4 mrad). Generally, electrode configurations with large mutual inductances showed good agreement between the corrected impedances and the modeled impedances obtained from a forward model with appropriate capacitances. It is important to note that the geometry of the cables was not easy to control in the pool measurements. Thus, the positional accuracy is not high, and this affected the accuracy of the modeling and the quality of the phase correction. Since it is easier to obtain the cable geometry in the case of borehole measurements, the obtained phase accuracy of 1 mrad at 1 kHz is expected to be realistic for field EIT measurements.

4.6 Field demonstration

Field measurements were performed at the Krauthausen test site, Germany (Vereecken *et al.* 2000; Kemna *et al.* 2002; Müller *et al.* 2010), to demonstrate the feasibility of the correction procedures. Borehole EIT measurements were made in boreholes 75 and 76, which are separated by 5 m. The water table was at about 2 m depth. The electrode chain in borehole 75 had the first electrode at a depth of 2.8 m and the last (8th) electrode at 9.8 m. The electrode chain in borehole 76 had the first electrode at a depth of 3.2 m and the last (8th) electrode at 10.2 m. We used several electrode configurations for current injection, e.g., skip-0 (1 2, 2 3, 9 10, 10 11…), skip-2 (1 4, 2 5, 9 12, 10 13…), skip-4 (1 6, 2 7, 9 14, 10 15…), skip-6 (1 8, 9 16) and cross-hole (1 9, 2 10… 8 16, 1 11, 2 12, 5 10, 6 11, 1 16, 8 9…). For potential measurements, we used the same electrode pairs except those including the current electrodes.

We reconstructed the complex resistivity of the soil at 1 kHz using three data sets, i) the original uncorrected measurement data, ii) the data after correction of the inductive coupling and iii) the data from ii) with integrated capacitances in the FEM forward model. The complex resistivity distribution was reconstructed in 1D (z-direction) using a 3D-forward model (Zimmermann *et al.* 2008) of the subsurface, as was already used in Zhao *et al.* (2013). The regularization was applied to the z-direction to obtain a smooth profile and to stabilize the reconstruction.

Figure 4.8 shows that the use of uncorrected impedance data resulted in excessively large phase angles, and also showed physically implausible positive phase values. After the correction of inductive coupling, the phase values showed much less variation with depth and ranged from −2 to −6 mrad, which is in good agreement with laboratory measurements of the complex resistivity. The consideration of capacitive coupling only had a small effect (<1 mrad) on the inverted phase angle. As expected, the real part of the resistivity is not

affected by the corrections of inductive and capacitive coupling. The retrieved resistivity profile using a 1D inversion of the cross-borehole EIT measurements are consistent with the 1D inversion results of Zhao *et al.* (2013) that were obtained from EIT measurements within a single borehole.

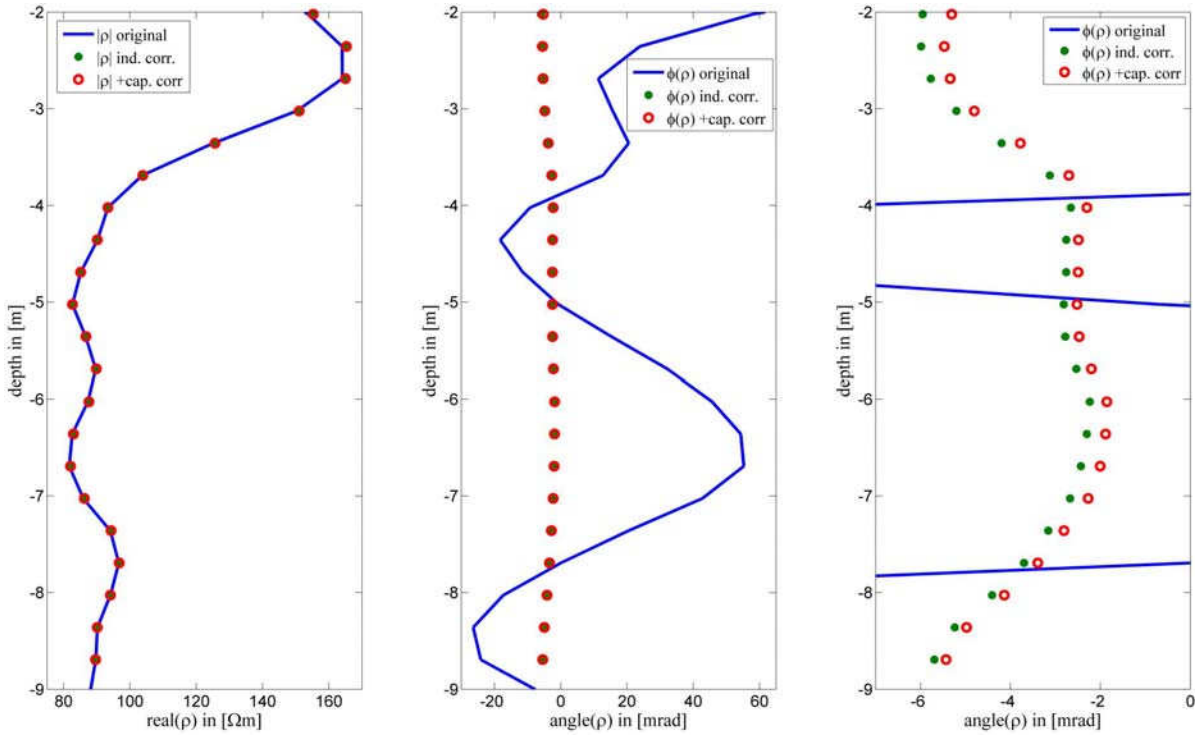

Figure 4.8: 1D inversion of original measured impedance (curve), impedance after correction of inductive coupling (solid circles) and impedance after correction of inductive and capacitive coupling (open circles) for cross-hole field measurements at 1 kHz (left: real part of the impedances; middle: phase angle of the impedances; right: zoom of impedance phase angles)

4.7 Conclusions

An effective approach was presented to correct inductive coupling in borehole EIT measurements for all possible electrode configurations using one or more borehole electrode chains. This approach considers both the mutual inductance associated with inductive coupling inside each borehole chain, which is determined with calibration measurements, and the mutual inductance associated with inductive coupling between two borehole chains, which is calculated from the geometry of the cable layout. These mutual inductances were assembled in a convenient pole-pole matrix that allows a simple and straightforward estimation of inductive coupling for arbitrary electrode configurations. We found that it is important to consider parasitic additive inductances of additional cables used

for the calibration measurements of each chain, and developed an adapted calibration method to estimate these inductances and remove them from the mutual inductances in the pole-pole matrix. This adapted calibration method relies on a special cable layout. It was also found that the inductive response from the subsurface was negligible for typical borehole EIT configurations as compared with the inductive effects of the cables. Thus, only the geometry-dependent inductive coupling of the cables was considered. The capacitive coupling between the subsurface and the cable shield is the second source of phase errors. Since this coupling depends on the (unknown) resistivity distribution of the subsurface, the effective capacitances were integrated in the forward model used in the inversion of the soil resistivity profile.

Pool measurements were performed to verify the developed correction approach for inductive coupling. Electrode configurations with strong inductive coupling showed good agreement between the corrected impedances and the calculated impedances obtained from a forward model with appropriate capacitances. The achieved phase accuracy was about 1 mrad at 1 kHz. Since positional accuracy was not optimal in these pool measurements, this accuracy is considered to be a conservative estimate of what is achievable in borehole EIT measurements. Finally, borehole EIT measurements were performed using electrode chains in two boreholes. After correction of inductive and capacitive coupling, 1D inversion results that considered cross-hole configurations were plausible and consistent with independent laboratory impedance measurements and previous 1D inversion results obtained from borehole EIT measurements using a single electrode chain (Zhao *et al.* 2013). The field EIT measurements clearly showed that the largest phase errors were associated with inductive coupling, and that consideration of capacitive coupling was of secondary importance. Overall, the results showed that the developed correction methods are effective and applicable for field measurements in two or more boreholes. The obtained high phase accuracy considerably improves the in-situ characterization of the frequency-dependent complex resistivity of weakly polarizable soils and sediments.

5 Application of correction methods to passive unshielded and shielded electrode chains

5.1 Introduction

In the previous chapters, the inductive and capacitive coupling effects of the developed borehole electrode chains were investigated and the induced phase errors were successfully corrected for different measurement configurations in borehole EIT measurements. All the measurements were performed with the custom-made active electrode chains with sophisticated integrated relays and amplifiers, which provide accurate and distortion-minimized measurements. However, the complex design of these active electrode chains also brings some disadvantages, such as the large diameter of the electrode chain, the difficulty of achieving a completely water-tight electrode chain, and the inflexibility with regard to the length of the chain once it has been fabricated. In contrast, commercially available or custom-made passive electrode chains with shielded or unshielded multi-core cables are thin, robust, watertight, and flexible in their design. Furthermore, such passive electrode chains are used for a wide range of commercial applications and typically have standard connectors that can easily be connected to another measurement system with or without adapter. In geophysics alone, there are many manufacturers that rely on such passive multi-core cables for ERT and EIT measurements, such as IRIS Instruments, Multi-Phase Technologies LLC, DMT GmbH & Co.KG, ABEM Instrument AB, amongst others. One example of the successful use of custom-made passive shielded multi-core electrode chains was described in Flores Orozco (2012).

In this chapter, the aim is to evaluate whether passive electrode chains can also be used to obtain accurate EIT field measurements in the high frequency range (up to 1 kHz) by using the correction methods introduced in previous chapters. In this evaluation, it is assumed that the measurement system itself does not induce much phase errors (e.g. EIT40 system) due to its inner electronics, e.g. capacitive load (e.g. see Zimmermann *et al.* 2008). This may not be the case for all commercially available measurement systems, which possibly induce already too much phase errors themselves so that the phase errors induced by the electrode chains cannot even be seen in EIT measurements with an excitation frequency

above 100 Hz. In particular, two types of passive electrode chains will be considered: commercially available unshielded multi-core electrode chains (hereafter referred to as *unshielded chain*) and custom-made shielded electrode chains (hereafter referred to as *shielded chain*). Uncorrected and corrected borehole EIT measurements obtained with these two types of passive electrode chains will be presented and compared to borehole EIT measurements obtained with the custom-made active borehole electrode chains (hereafter referred to as *active electrode chain*) used in the previous chapters.

5.2 Estimation of the phase errors for passive electrode chains

5.2.1 Unshielded passive multi-core electrode chains

In a first step, the unshielded chains (borehole chain for RESECS system with the multi-core cable: LAPP-PUR/TPE ZE 26x0.34 YE, DMT GmbH & Co. KG) were investigated for their applicability for EIT field measurements with high phase accuracy. The unshielded chain consists of 16 unshielded wires which are connected to 16 electrodes (diameter of 2.5 cm, length of 8 cm) with an electrode separation of 0.5 m. At the end of the chain, a multi-pin connector with 16 pins is used to connect the chain to the RESECS system. In order to connect this cable to the EIT system, electrode modules for laboratory measurements (Zimmermann *et al.* 2010) were connected to the pins of the multi-pin connector using custom-made adaptors with appropriate dimensions (figure 5.1). For convenience, only the 8 electrodes with even numbering (2, 4, 6… 16) were used so that the electrode separation is 1 m, which is the same as the electrode separation of the active electrode chain. This provides a good comparability between these two chain types. The main difference between the passive unshielded electrode chain and the active electrode chain (figure 3.1) is that there is no active electronics inside the chain, so that the potential measurement is performed not directly at the electrodes, but at the electrode modules at the end of the chain.

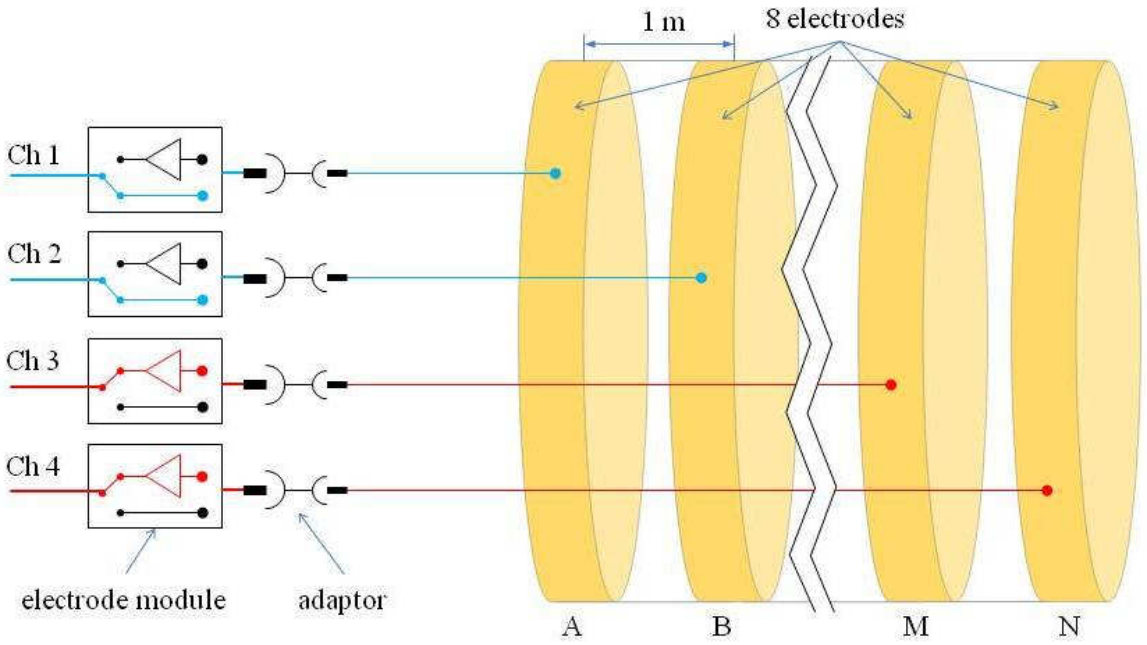

Figure 5.1: Simplified block diagram of unshielded chains connected to the electrode modules (compare to figure 3.1).

A simplified circuit diagram of EIT field measurement is shown in figure 5.2. Electric current I_s is injected into the soil at two electrodes A, B and the voltage U_{MN} is measured at another two electrodes M, N. The contact impedances Z_g between the electrodes and the measured object Z_o (soil) can produce measurement errors due to the phase errors in combination with capacitive loads (Zimmermann 2011). The contact impedances can be determined with extra voltage measurements between the current electrodes A and B (Zimmermann 2011).

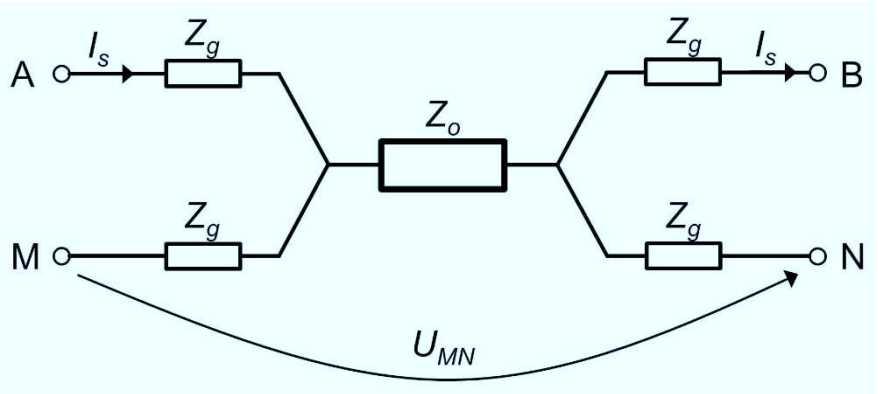

Figure 5.2: Four-point field measurement with consideration of contact impedances

As shown in chapter 3, inductive and capacitive coupling will occur in field EIT measurements. The inductive coupling between the current loop and the potential loop can be determined with the methods introduced in chapter 4. There exist two kinds of capacitive coupling in EIT measurements with unshielded chains. The first type of capacitive coupling occurs between each wire and the conductive environment, and the second type occurs

between neighboring wires. The equivalent circuit diagram of an EIT measurement with an unshielded chain is shown in figure 5.3 without consideration of inductive coupling. There are four wires in the circuit diagram which represent the four wires connected to four electrodes of the unshielded chains. Wire 1 and 2 of figure 5.3 are used for current injection, while wire 3 and 4 are used for voltage measurements. The excitation is represented with two AC voltage sources (V1 and V2 in figure 5.3) to ensure a symmetric current injection. R_{s1} and R_{s2} (100 Ω) are the shunt resistors for measuring the true injection current (section 2.2). Z_{g1}, Z_{g2}, Z_{g3} and Z_{g4} are the contact impedances at the electrodes, which are assumed to be 350 Ω in this case. This value for the contact impedance was obtained from field measurements in saturated soil with an electrical resistivity between 80 and 100 Ωm. However, in practice the value of Z_g can vary in the Ω to kΩ range in EIT measurements depending on the electrode geometry (Cardu *et al.* 2012) and the electrical properties of the measurement object (Vilhunen *et al.* 2002). The large resistors R_5 and R_6 (500 GΩ) represent the input impedances of the amplifiers in the electrode modules for voltage measurements at the ends of wire 3 and 4 (Zimmermann 2011). The capacitive load of the amplifiers is small (< 10 pF) in relation to the other capacities and therefore neglected. In this example, the impedance of the soil, Z_o, is set to 30 Ω, a typical value for measured transfer impedances.

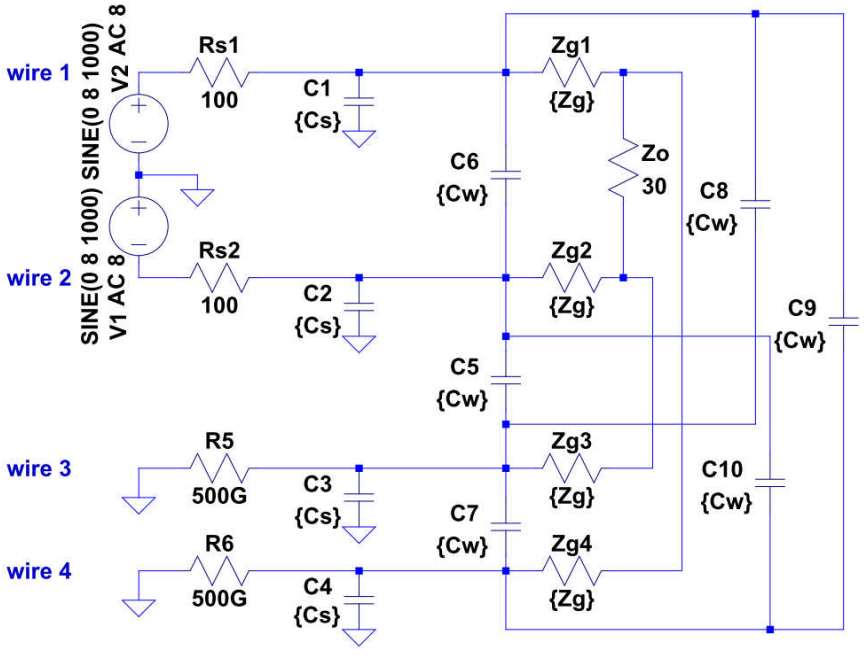

Figure 5.3: The equivalent circuit diagram for a borehole EIT measurement with unshielded chains.

The capacitive coupling between the wire and the soil, Cs, and the capacitive coupling between wires, Cw, depends on the borehole EIT measurement setup, which differs

according to the four cases shown in figure 4.1a-d. To simplify the analysis, only the capacitive effects of the four wires used for a single electrode configuration were considered. For the first case with one chain (figure 4.1a), the capacitive coupling occurs between all possible pairs of active wires inside the chain (Cw), which results in six different capacitances (C_5 to C_{10} in figure 5.3). Furthermore, the capacitances C_1 to C_4 between the four wires and the conductive soil (Cs) are also different from each other because there is no common shield for the chain so that each wire has a different geometrical relation to the soil. It is impossible to calculate all these geometry-dependent capacitances, because the exact geometries of the wires inside the chain are not known a priori. This means that the phase errors introduced by the capacitive coupling cannot be calculated accurately. However, it is possible to obtain a rough approximation of how these capacitive couplings affect phase measurements with EIT. Measurements on the unshielded electrode chain in the laboratory (as described in section 3.4) have shown that the capacitances C_5 to C_{10} can reach a value of Cw = 1160 pF (46.3 pF/m, 25 m long cable). The capacitances C_1 to C_4 were approximated using:

$$C = 2\pi\varepsilon_0\varepsilon_r \frac{L}{\ln\left(\frac{h}{r} + \sqrt{\left(\frac{h}{r}\right)^2 - 1}\right)}, \tag{5.1}$$

which describes the capacitance C between a wire and a parallel wall (Plaßmann and Schulz PU (polyurethane) and TPE (thermoplastic elastomers) at 1 kHz, which is 3.5. Using (5.1) the capacitance C_1 to C_4 was estimated to be 1180 pF (147.8 pF/m*)*. The circuit model shown in figure 5.3 with the properties presented above was implemented in LTspice (circuit simulation tool from Linear Technology Corporation) to simulate a borehole EIT measurements in a single borehole. The simulation results showed that the phase error produced by these capacitive loads reached a value of 13 mrad at 1 kHz for this first case.

For the second case (figure 4.1b), the two chains are placed in two separate boreholes (wire 1 and 2 in the first chain, wire 3 and 4 in the second chain). In figure 5.3, only C_6 and C_7 will remain and C_5, C_8, C_9, C_{10} can be neglected due to the big separation between these wires (several meters). The capacitive coupling between the wires and the soil remains unchanged. Using this slightly simplified electrical circuit model, the phase error due to the capacitive loads was reduced to 8 mrad at 1 kHz. In the third case (see figure 4.1c), only C_5, C_6, C_8 and all the Cs remain. In this case, the simulation results indicate a phase error of 5 mrad at 1 kHz. In the fourth and final case (figure 4.1d; wire 1 and 3 in one borehole, wire 2 and 4 in another) only C_8, C_{10} and all the Cs remain. An estimated phase error of 68 mrad at 1 kHz is obtained, which is much larger than the other three cases because the capacitances can impact the phase in both directions according to their circuit manner. In

the fourth case the two remaining capacitances coincidentally influence the phase in the same direction and other opposite capacitances vanished. The estimated phase error further increased to 120 mrad at 1 kHz when the transfer impedance Z_o was lowered to 16 Ω as obtained in the cross-hole EIT measurement shown in figure 4.7. These approximate model simulations have shown that the large capacitances in case of unshielded cables can have a strong influence on the measured phase, and can lead to very substantial measurement errors. It is evident that accurate determination of all participating capacitances is required to obtain reliable phase measurements.

Field measurements with unshielded chains were performed for comparison with the estimated phase errors. Figure 4.4 shows the measured transfer impedances Z_m and the impedances Z_{CR} after correction of inductive coupling effect with the correction method introduced in chapter 3 for a typical cross-hole configuration [1 9 2 10] (see correction procedure in section 4.3). It can be seen that the resistance measurement is not strongly affected by inductive or capacitive coupling. However, the phase measurement is strongly affected from a frequency of 50 Hz upwards. The phase angle of the impedance after correction of inductive coupling effect is about 100 mrad at 1 kHz. Above about 100 Hz the influence of the capacitive coupling is already enormous and no more reliable data can be provided. Such large phase angles have not been seen in the reference EIT measurements with the active electrode chains (e.g. figure 4.8).

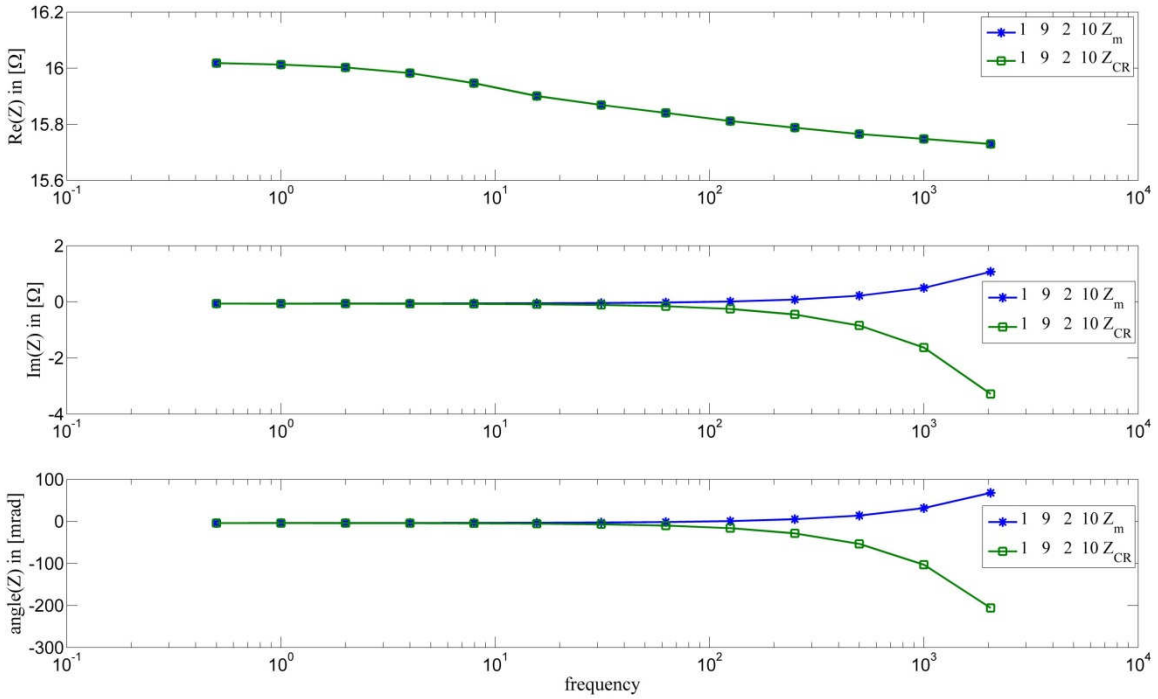

Figure 5.4: The measured and corrected transfer impedances for the configuration [1 9 2 10] of the cross-hole measurement with unshielded chains: Z_m: original measured transfer impedance; Z_{CR}: impedance after correction of inductive coupling (compare to figure 5.10)

It is important to emphasize here that the estimated phase error was obtained using approximate values only because the exact values of these capacitive couplings cannot be obtained accurately. Although the estimated (120 mrad at 1 kHz) and the measured phase errors (100 mrad at 1 kHz) are reasonably similar, the modeling approach clearly is not accurate enough to remove the capacitive coupling from field EIT measurements. Therefore, it was concluded that unshielded electrode chains are not suitable for broadband borehole EIT measurements due to the strong but inaccurately known capacitive couplings.

5.2.2 Shielded passive multi-core electrode chains

There are a lot of shielded multi-core cables on the market, but none of them has been used to build commercially available shielded electrode chains for geophysical surveying. Using custom-made shielded electrode chains, Flores Orozco (2012) successfully increased the accuracy of his EIT measurements. Therefore, a shielded passive electrode chain was built for this study too. For this, an isolated and shielded multi-core cable consisting of six coaxial cables (MC6/75, Guntermann & Drunck GmbH) with an overall diameter of 13 mm and a length of 12.5 m was used. Six copper electrodes (diameter = 15 mm, length = 25 mm) with an electrode separation of 1m (figure 5.5a and figure 5.5b) were soldered directly to the wires inside the shielded chain without any active parts inside the electrodes (figure 5.5c).

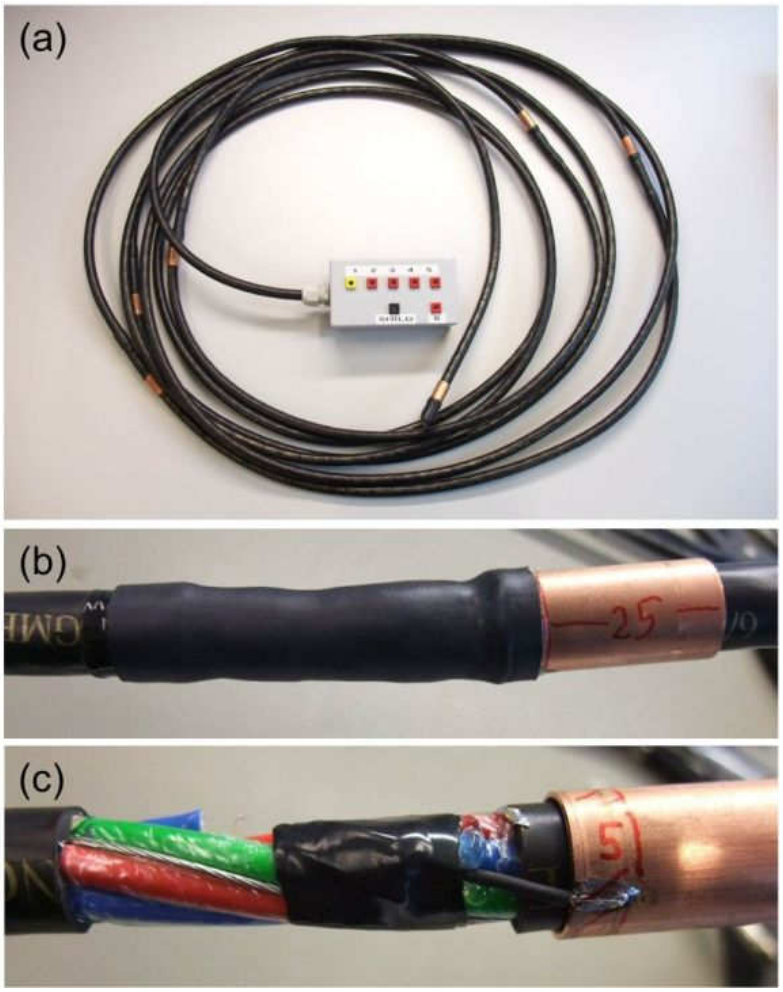

Figure 5.5: a) the custom-made shielded passive electrode chain; b) copper electrode; c) soldering of the wire on the electrode.

All wires of the shielded chain are assembled into an adaptor box for the connection to the EIT system. The shields of all wires and the shield of the chain are connected together with the EIT system ground. Adaptors connect the 6 wires of the chain with 6 electrode modules, which are used to switch between current injection and voltage measurements (figure 5.6). As for the unshielded chain, the potential measurement is not performed directly at the electrodes, but at the electrode modules at the end of the chain. The main difference to the unshielded chain is that all wires and the entire cable are shielded, which reduces the amount of capacitances that need to be considered.

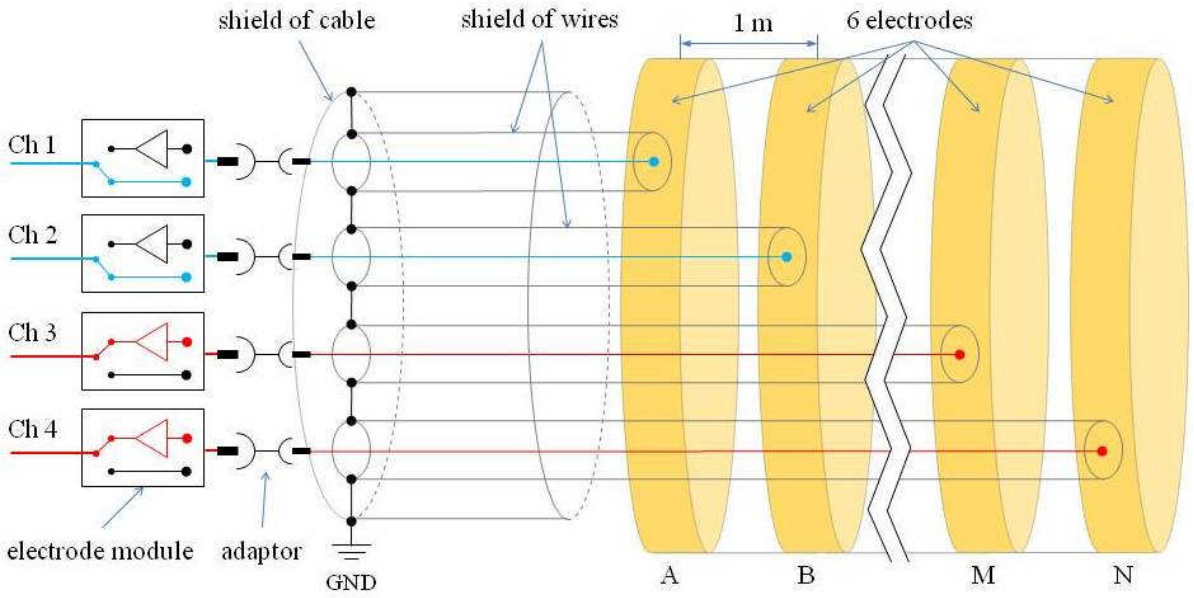

Figure 5.6: Simplified block diagram of shielded chain connected to the electrode modules (compare to figure 3.1c and figure 5.1).

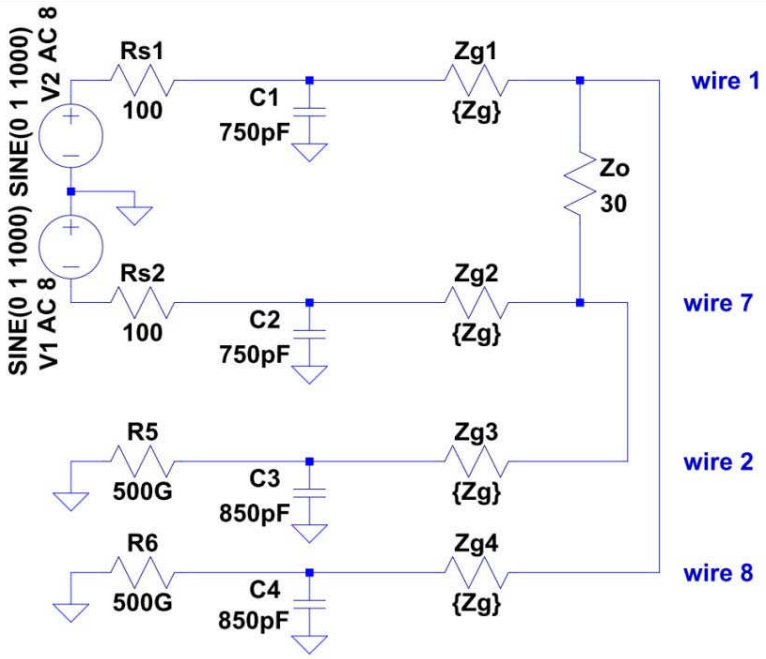

Figure 5.7: The equivalent circuit diagram of the field measurement with shielded chains (compare to figure 5.3).

An equivalent circuit diagram (figure 5.7) was also developed for the shielded electrode chain for one electrode configuration [1 7 2 8]. This is a typical cross-hole configuration (with the strongest inductive coupling effect) where 1 and 2 are the first two electrodes of the first shielded chain in one borehole, while 7 and 8 are the first two electrodes of the second shielded chain in another borehole. Wire 1 and 7 are used for current injection, while wire 2 and 8 are used for voltage measurements. The AC voltage sources, the shunt

resistors, the contact impedances, the input impedance of the amplifiers, and the soil impedance is assumed to be identical to those specified before for the unshielded electrode chain.

The capacitances C_1, C_2, C_3 and C_4 are the capacitances of the coaxial cables (100 pF/m, according to the manufacturer) between the wires and the shields, which are connected with the system ground. The length of the cable part from the front end of the chain to the first electrode is 7.5 m and the cable length to the second electrode is 8.5 m. Therefore, $C_1 = 7.5m \times 100pF/m = 750\ pF$ and $C_3 = 8.5m \times 100pF/m = 850\ pF$. The values for $C_2 = 750\ pF$ and $C_4 = 850\ pF$ are obtained in the same way for the second chain. There is no capacitive coupling occurring between the two chains because of the large separation between two boreholes (several meters). The capacitive coupling between the cable shield and the environment is neglected in this model. It is expected to be smaller than for the active electrode chains (1 mrad at 1 kHz, see section 3.4) due to the smaller diameter of the cable.

It is interesting to note here that the equivalent circuit diagram in figure 4.7 can also represent borehole EIT measurements with active electrode chains. The only difference is the higher capacity of C_3 and C_4 in case of passive shielded chains. In case of the active electrode chains, the values of C_3 and C_4 at the potential electrodes are the input capacitances of the active electrode modules (50 pF) that are used to directly measure the potentials at the electrodes with the integrated amplifiers (i.e. the capacitances of the coaxial cables are not involved in the measurement any more). Assuming that the inductive couplings in both measurements (one with shielded chains, one with active electrode chains) are the same, the phase difference between these two types of electrode chains should only come from the different values of the two capacitances C_3 and C_4 because the impact of C_1 and C_2 is minimized by the correction of the injection current (Zimmermann *et al.* 2008). The expected phase difference can then simply be calculated by

$$\varphi_{diff} = angle\left(\frac{1}{1 + j\omega R_C C_{PSC}}\right) - angle\left(\frac{1}{1 + j\omega R_C C_{AC}}\right), \tag{5.2}$$

where C_{PSC} (C_3 or C_4) is the capacitance of the passive shielded chain and C_{AC} (C_3 or C_4) is the capacitance of the active electrode chain, $R_C = 300\ \Omega$ is the contact impedance between the electrode and the soil (Z_{g3} and Z_{g4} in figure 5.7). At 1 kHz, this equation suggests that the phase difference between active and passive shielded electrode chains is 1.5 mrad, which was also verified with SPICE simulations. It is important to note that this phase difference is obtained for relatively short passive shielded chains (12 m) as compared with the active electrode chains (25 m). If longer cables are used, the expected phase difference

will increase accordingly. This phase difference is related to the different design of both electrode chains and will remain in the EIT measurement data after correction for inductive coupling. This will be verified with actual borehole EIT measurements in the next sections.

5.3 Borehole EIT measurements with active and passive shielded electrode chains

Borehole EIT measurements were performed with both active electrode chains and passive shielded chains on the test site Krauthausen in the same two boreholes used in the previous chapter. The borehole separation was 5 m and the water table was about 3.2 m below surface at the time of the measurements. The top electrodes of both chain types were placed at the same depth of 4.2 m, so that the bottom electrodes were at a depth of 11.2 m for the active electrode chain and at 9.2 m for the shielded passive electrode chain (figure 5.8). With this setup, electrodes are at the same depths and identical measurements can be found for both chain types. For example, the configuration [1 9 2 10] of the passive shielded chains corresponds to the configuration [1 7 2 8] of the active electrode chains. For convenience, only electrode configurations of the active electrode chains will be mentioned in the remainder. The cable parts on the surface were arranged in a triangle so that the geometry could be determined easily (see e.g. section 4.3).

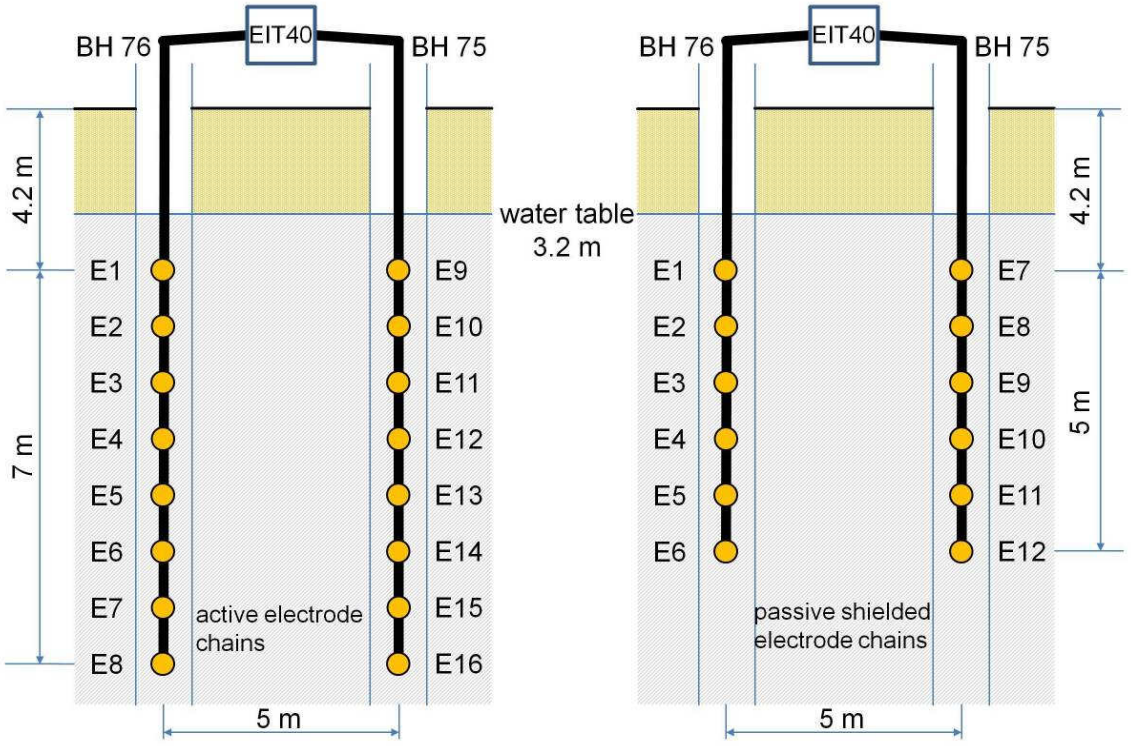

Figure 5.8: EIT borehole field measurements with active electrode chains and passive shielded chains in borehole 75 and 76 of the test site Krauthausen.

Typical cross-hole configurations were used in the measurements, e.g.: [1 9 2 10], [1 9 3 11] …, [1 9 6 14], [2 10 1 9], [3 11 2 10], etc. In a first step, the real part of the measured transfer impedances of selected electrode configurations were compared to obtain an overview of the measurement quality. As shown in figure 5.9, the measured resistances matched well for most configurations. However, the deviation is considerably larger for configurations where the lower electrodes were used (E5, E6, E13, E14). This was attributed to a flooded lower electrode for the passive shielded chain that resulted in a short circuit through the cable shield. Secondly, it can be seen that most reciprocal measurements were in good agreement for both chain types (e.g. compare [1 9 2 10] and [2 10 1 9] in figure 5.9). In the remainder of this chapter, it will be focused on the top electrodes for further comparison between the two chain types.

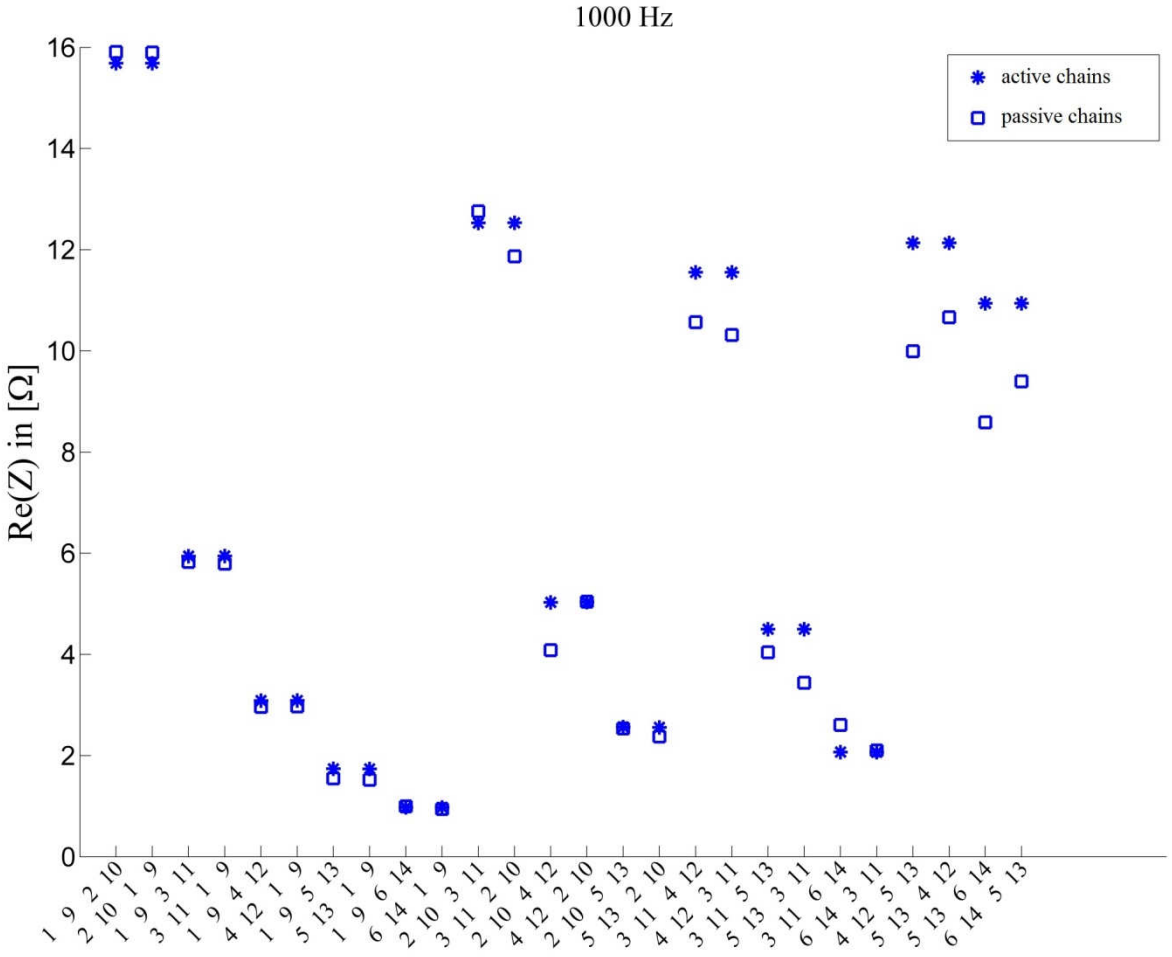

Figure 5.9: Comparison of the measured resistances obtained with active chains and passive shielded chains at 1 kHz

In a second step, the measured transfer impedances were corrected for inductive coupling using the methods introduced in the previous chapters in order to obtain corrected transfer impedances Z_{CR}. This required calibration measurements for each electrode chain as

introduced in the previous chapters. In particular, the calibration measurements for a single electrode chain were performed as shown in figure 4.2, and the pole-pole matrix was built for each shielded chain (4.9). The pole-pole matrix of the passive shielded chain has a dimension of 6x6, and contains the additive terms produced by the grounding wires which must be determined with the calibration measurement with two chains (similar to figure 4.3).

Using (4.10) and (4.11), the three parameters for the additive inductances for the passive shielded chains were obtained and used to assemble the two matrices $\boldsymbol{M}^1$ and $\boldsymbol{M}^2$ in (4.9) using (4.12), which reflect the properties of the shielded chains themselves. The geometry-dependent matrices $\boldsymbol{M}^{12}$ and $\boldsymbol{M}^{21}$ were numerically calculated from the known cable layout (section 4.3). This then provides the true pole-pole matrix for the two shielded chains, which can be used together with (4.7) to calculate the mutual inductance or rather the mutual impedance for any electrode configuration used for EIT measurements. The calculated mutual impedance Z_{ind} due to the inductive coupling was subtracted from the measured transfer impedance Z_m for each electrode configuration to obtain the corrected transfer impedance Z_{CR} according to:

$$Z_{CR} = Z_m - Z_{ind} = Z_m - i\omega M \ . \tag{5.3}$$

As in the previous chapters, it is important to note that the capacitive coupling between the cable and the soil is not removed from the measured transfer impedance Z_m and thus included in Z_{CR}. For both field measurements with passive shielded chains and active electrode chains, the corrected transfer impedances will be determined and compared with each other without considering the capacitive coupling between the cable and the environment because these capacitive coupling are relatively similar and small (see e.g. section 3.4).

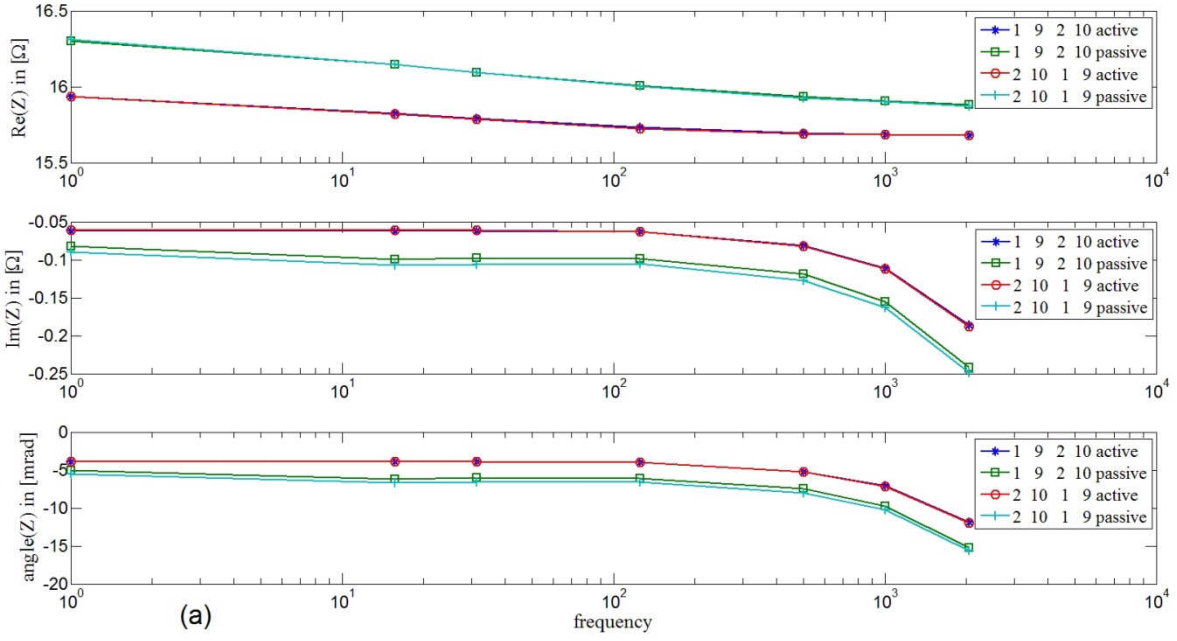

(a)

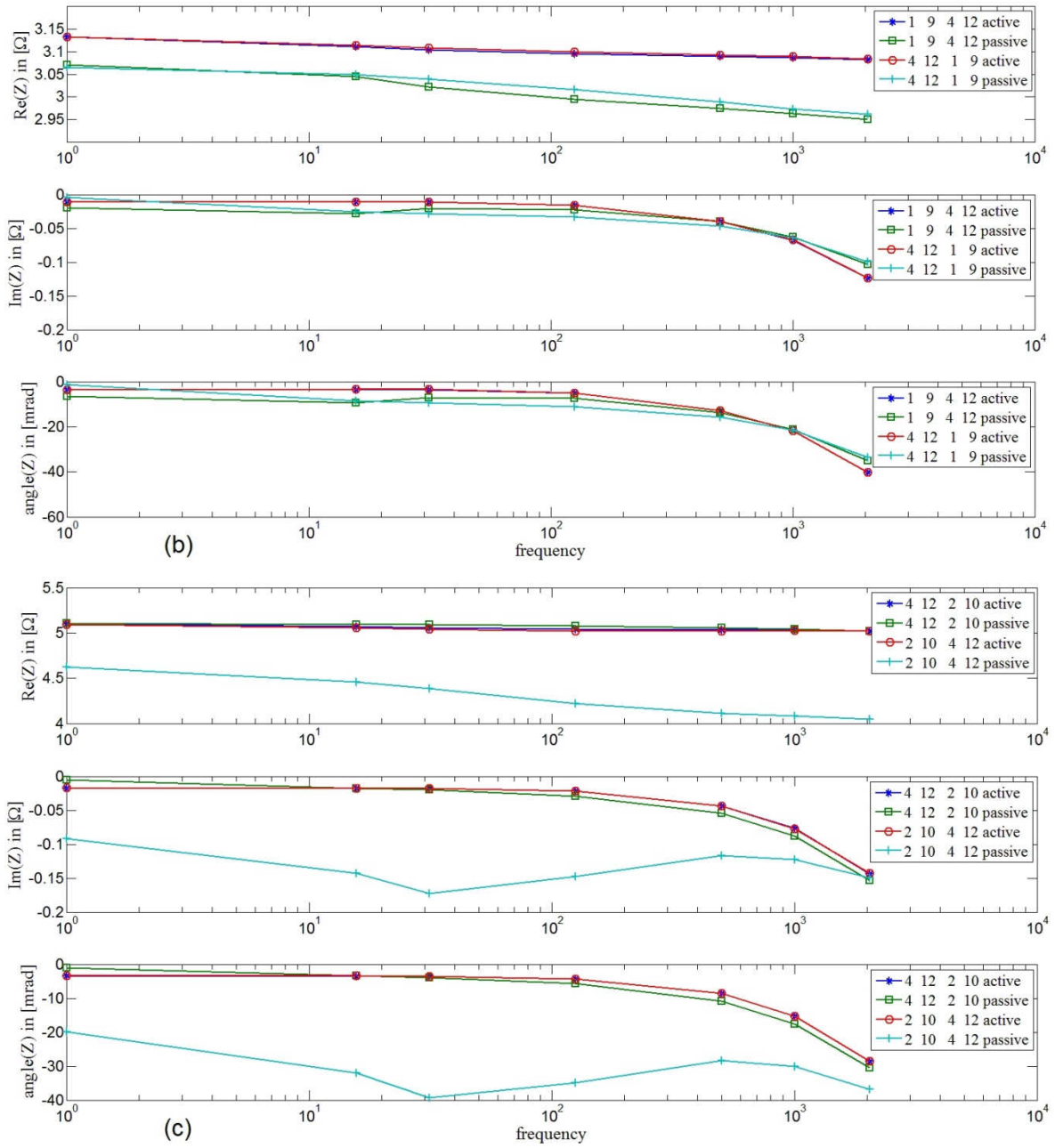

Figure 5.10: Comparison of transfer impedances Z_{CR} after correction of inductive coupling for several configurations with active electrode chains and passive shielded chains.

The comparison of Z_{CR} for several normal and reciprocal electrode configurations obtained using active and passive shielded chains is shown in figure 5.10. The first three configurations (figure 5.10a, b and c) show good agreement in resistance and phase measurements with active electrode chains and shielded chains. The corrected phase angles of the two chain types are relatively similar. The deviations lie between 2 and 4 mrad at 1 kHz, which is a little higher than the estimated phase difference in section 5.2 (1.5 mrad). Possible explanations for this are: i) different electrode coupling inside the borehole due to differences in diameter of the cable and size of the electrodes, ii) different

polarization behavior of the electrodes due to different materials (brass electrodes on the active electrode chain, copper electrodes on the shielded chains), or iii) the assumption that the capacitive coupling between the cable shield and the environment is identical for both electrode chain types, which requires the same geometry of the cable (same surface and same thickness of the cable insulation) and the same material, which is in fact not the case. Considering all these points above and the error sources due to the cable structure mentioned in section 5.2, a phase deviation less than 3 mrad at 1 kHz was nevertheless achieved. In general, the passive shielded chains showed a similar behavior as the active electrode chains. Therefore, it was concluded that it is also possible to perform borehole EIT measurements with short passive shielded chains with good phase accuracy. When the prototype passive electrode chain is improved with respect to water tightness and electrode dimensions, a phase difference considerably less than 3 mrad is expected between passive and active electrode chains.

5.4 Summary and outlook

In this chapter, it was evaluated whether the correction methods for inductive and capacitive coupling effects developed for active electrodes in chapter 3 and 4 can also be used to improve phase measurements with simple passive electrode chains. In contrast to the active borehole electrode chains, the shielded and unshielded passive electrode chains are more robust, easy to build, and their widespread application testifies the high adaptability of this cable type to a range of commercial ERT and EIT systems. When using passive electrode chains, the main challenge is that both the capacitive load of the wires inside the cables and the inductive coupling between the wires in the cables affect the phase measurements. A detailed analysis of these capacitive loads was presented for both passive shielded and unshielded electrode chains. In the case of unshielded chains, it was concluded that accurate calculation of the possible phase errors is not possible because there are too many indeterminable capacities involved in such an electrode chain design. Nevertheless, a rough first estimate of possible phase errors due to capacitive coupling in unshielded electrode chains was obtained from LTSpice simulation and field measurements. Here, it was found that the remaining phase angles after correction of the inductive coupling at 1 kHz are still high (> 100 mrad) due to the indeterminable capacitive coupling of the chains.

In the case of passive shielded electrode chains, the possible phase error due to the additional capacitive load of the cable was also evaluated. It was found that the expected difference between the phase angles measured with active and passive shielded chains is

about 1.5 mrad at 1 kHz for a cable length of 7-8 m and a contact impedance of 300 Ω. In this analysis, it was assumed that the inductive coupling in both measurements can be removed completely and that the capacitive coupling between the cable shield and the environment is similar for both chain types. This relatively low error in the estimated phase difference clearly shows that shielded chains are much better suited for accurate phase measurements with EIT. To further substantiate this, borehole EIT measurements were made with both active and passive shielded electrode chains. After correcting the measured transfer impedances for inductive coupling between the wires, the magnitude and phase of the measured impedance matched well for both chain types with deviations between 2 - 4 mrad at 1 kHz. These remaining differences were somewhat higher than expected, which was attributed to different diameters of the electrodes and the cables.

The results presented in this chapter inspire confidence that it is possible to obtain accurate phase measurement with passive shielded electrode chains instead of custom-made active electrode chains. This requires appropriate corrections for inductive coupling and the capacitive loads of the cable in addition to improvements in the design of the prototype passive electrode chains with respect to water tightness and electrode dimensions.

6 Conclusions and Outlook

6.1 Conclusions

The objective of this work was to improve the phase measurement accuracy for borehole EIT measurements in order to obtain an on-site and field-scale characterization of subsurface structures and processes that extends the traditional way of characterization using small soil samples to the field scale. To do this, the main interference source of field EIT measurements, electromagnetic coupling, was investigated and procedures were proposed to remove phase errors associated with inductive and capacitive coupling from the measured data.

Chapter 3 addressed the development of correction procedures to remove phase errors from EIT borehole field measurements in one borehole with a single custom-made active electrode chain. The inductive coupling between the current and the potential wires inside the multi-core cable was determined using a first calibration measurement and verified using calculations based on internal wire geometry. A frequency-dependent behavior of the inductive coupling was observed, which is related to the eddy currents in the conductive shielding of the multi-core cable at high frequencies. This effect was ignored because its impact on inductive coupling within the applied frequency range (<1 kHz) was negligibly small. The capacitive coupling between the cable and the electrically conductive environment was also found to be frequency-dependent and could be described with a Cole-Cole model because the electrical cable can be considered as a linear time-invariant system. The developed phase correction methods were verified by a test measurement performed in a water-filled rain barrel using a borehole EIT logging tool. The capacitive coupling was modeled in 3D by using a 2D finite-element mesh, which is sufficient, because the measurement set-up is axis-symmetric and the electric field distribution does not depend on the circumferential axis. The difference between the modeled transfer impedance and the measured transfer impedance after the correction of inductive coupling was 0.8 mrad at 10 kHz, which suggests good measurement accuracy after correction. Additionally, borehole EIT measurements were performed at the Krauthausen test site using a borehole electrode chain to demonstrate the improvements that can be achieved in field conditions with the correction approaches. Inverted resistivity magnitude and phase profiles

considering both corrections matched well with the general stratigraphy of the test site. This first step of phase measurement correction proved that it is possible to estimate the induced phase errors when the internal cable geometry is fixed and the dielectric permittivity of the cable material is well known.

In chapter 4, an effective approach is developed to correct inductive coupling for EIT measurements in two or more boreholes and all possible electrode configurations. As in the case of measurements in a single borehole, the measured impedance is affected by the complex electrical resistivity of the earth and additional possible inductances due to inductive coupling between the electrical wires. The inductive effects associated with the subsurface were found to be small and negligible under the used measurement conditions in one or two boreholes (excitation frequency <1 kHz, borehole distance <10 m). Thus, the correction approach for inductive coupling focused on inductive coupling between the electrical wires, which is dependent not only on the internal geometry of the wires inside the electrode chain but also on the cable layout when more than one borehole chain is used. Therefore, the related mutual inductances of the inductive couplings are divided into two parts. The first part is associated with inductive coupling inside each electrode chain, which is dependent on the internal wire geometry and was determined using calibration measurements. The second part is associated with inductive coupling between two electrode chains, which is calculated based on the geometrical layout of the used electrode chains. These two kinds of mutual inductances were assembled in a convenient pole-pole matrix that allows a simple and straightforward estimation of inductive coupling for arbitrary electrode configurations. The undesirable parasitic additive terms contributed by the ground connection used for the calibration measurement were also integrated into the matrix. This required an adapted calibration method to estimate these additive inductances and remove them from the mutual inductances in the pole-pole matrix. This adapted calibration method relies on a special cable layout during calibration. A comparison between the measured transfer impedances with and without the consideration of these additive inductances in the calibration measurement clearly illustrated the importance of this issue.

The correction of inductive coupling and the capacitive coupling between the environment and the cable shield was verified under controlled conditions with measurements in well-defined conditions. It was found that electrode configurations with strong inductive coupling showed good agreement between the corrected impedances and the calculated impedances obtained from a 3D finite element model with appropriate capacitances. The achieved phase accuracy was about 1 mrad at 1 kHz. Finally, borehole EIT measurements were performed at the test site Krauthausen with typical cross-hole electrode configurations.

After correction for inductive and capacitive coupling, 1D inversion results that considered cross-hole configurations were plausible and consistent with independent laboratory SIP measurements and 1D inversion results obtained using borehole EIT measurements with a single electrode chain. The obtained high phase accuracy considerably improved the in situ characterization of the frequency-dependent complex electrical resistivity of weakly polarizable soils and sediments.

In the final part of the thesis, it was explored whether the developed correction methods for inductive and capacitive coupling effects can also improve phase accuracy of borehole EIT measurements using passive shielded or unshielded electrode chains. Such passive electrode chains are more robust, easy to build, and widely available. However, the additional capacitive load associated with these passive electrode chains leads to additional errors in the phase measurements. An analysis of the additional capacitances highlighted that an accurate correction of these additional phase errors is not possible for unshielded electrode chains because there are too many indeterminable capacitive couplings. For shielded electrode chains, reliable estimation of these additional phase errors was found to be feasible. If it is assumed that inductive coupling can be removed completely and that the capacitive coupling between the cable shield and the environment introduced the same phase error, the deviation between the measured phase obtained using passive shielded chains and active electrode chains was predicted to be 1.5 mrad at 1 kHz with a cable length of 7-8 m and a contact impedance of 300 Ω at the electrodes. Borehole EIT measurements with passive and active electrode chains at the Krauthausen test site showed good reciprocity and agreed well in terms of measured resistance and phase angle. The measured phase difference between measurements with both chains was about 2-4 mrad at 1kHz. The results in this chapter clearly suggest that it is also possible to obtain accurate borehole EIT measurements with shielded passive electrode chains.

The correction procedures to improve the phase accuracy of borehole EIT measurements presented in this thesis open up the possibility for a field-scale characterization of broadband spectral electrical properties of weakly polarizable soils and rocks that only show a phase angle between 1 and 20 mrad in the frequency range up to 1 kHz. A framework has been provided to apply the correction procedures for inductive and capacitive coupling for typical borehole EIT electrode configurations so that a high phase accuracy of 1 mrad at 1 kHz can be achieved when the EIT field measurement system is used in combination with custom-made active electrode chains. The developed correction procedures can also be applied to passive shielded multi-core electrode chains. Although the achieved phase accuracy was not as high as in the measurements with active electrode chains, the

measured data after phase error correction are clearly superior to uncorrected phase measurements.

6.2 Outlook

The presented correction methods are currently limited to a frequency range up to 1 kHz and a maximum electrode distance of 10 m because of several remaining error sources in field measurements that have not been treated in this thesis. The first remaining error source relevant for larger separations is the electromagnetic response from the subsurface itself, which depends on the complex electrical resistivity distribution. This effect was evaluated and considered to be of secondary importance because of its negligibly small magnitude for frequencies below 1 kHz and short separation between electrode cables. However, this effect should be considered and estimated explicitly in future research when higher phase measurement accuracy or measurements at higher frequencies are required since the strength of this secondary magnetic field increases with frequency and separation. In contrast to the inductive coupling considered in this thesis, the consideration of this error source will require advanced numerical modeling because of the dependence on the electrical resistivity distribution in the underground.

The consideration of capacitive coupling can also be improved. In particular, the used 3D finite element modeling approach relied on a mesh with a relative coarse spatial resolution because of the high computational demands associated with finer 3D meshes. In addition, the integrated capacities were partly estimated in this thesis because the dielectric permittivity of the cable material was not always known. In order to achieve higher phase accuracy, both problems need to be addressed. Furthermore, for the correction of capacitive coupling 2.5D forward model (3D source in 2D space) could be used, which is not straightforward to implement due to the inherent Fourier transform with respect to the strike direction of the assumed 2D spatial distribution. For the case of passive electrode chains, the capacitive coupling can be described more accurately when the geometry and the material of the cable insulation are accurately determined.

Some technical improvements can also be made to the design and use of the borehole EIT measurement system used in this thesis. For example, the calibration procedure for one active electrode chain should be improved so that it is performed automatically before each measurement. This should provide an even better phase accuracy for borehole EIT measurements because the internal cable geometry of the electrical wires likely is not fully rigid and may thus change with time or movement of the cable. The second calibration

measurement required for cross-hole measurements should also be improved because the assumption that two independent electrode chains are exactly the same is strong.

In this thesis, borehole EIT measurements in one or two boreholes were considered. In fact, the borehole EIT system allows to measure in multiple boreholes too. In this case, the developed correction methods for electromagnetic coupling can be applied almost without modifications. Only the formulation of the pole-pole matrix should be adapted, and this is straightforward. For example, when using five borehole electrode chains with eight electrodes each, the pole-pole matrix should be extended to a 40x40 matrix instead of 16x16 matrix used for two electrode chains.

Overall, the phase correction procedures presented in this thesis provide a wide range of application possibilities. Whenever long electrical cables are used and complex impedances are measured, the correction method developed for inductive coupling can be applied, which will improve the measurement accuracy considerably because the pure inductive coupling between the electrical cables is normally the main reason for decreased accuracy of the phase measurements. The 2- and 3-dimensional forward modeling of the capacitive coupling effect can also be used for measurements where strong capacitive load exists. In near future, this research should make an important contribution to near-surface geophysical research where complex impedance and phase measurement accuracy are of importance.

References

Archie G E. 1942. The electrical resistivity log as an aid in determining some reservoir characteristics. *Trans. AIME,* **146** 54-62

Bertin J and Loeb J. 1976. *Experimental and theoretical aspects of induced polarization,* (Berlin: Gebrüder Borntraeger)

Binley A, Slater L D, Fukes M and Cassiani G. 2005. Relationship between spectral induced polarization and hydraulic properties of saturated and unsaturated sandstone. *Water Resour. Res.,* **41** W12417

Börner F, Schopper J and Weller A. 1996. Evaluation of transport and storage properties in the soil and groundwater zone from induced polarization measurements. *Geophys. Prospect.,* **44** 583-601

Börner F D and Schön J H. 1991. A Relation between the Quadrature Component of Electrical Conductivity and the Specific Surface Area of Sedimentary Rocks. *The Log Analyst,* **32** 612-3

Breede K, Kemna A, Esser O, Zimmermann E, Vereecken H and Huisman J A. 2011. Joint Measurement Setup for Determining Spectral Induced Polarization and Soil Hydraulic Properties. *Vadose Zone J.,* **10** 716-26

Breede K, Kemna A, Esser O, Zimmermann E, Vereecken H and Huisman J A. 2012. Spectral induced polarization measurements on variably saturated sand-clay mixtures. *Near Surf. Geophys.,* **10** 479-89

Broding R A and Rummerfield B F. 1955. Simultaneous Gamma Ray and Resistance Logging as Applied to Uranium Exploration. *Geophysics,* **20** 841-59

Cardu R, Leong P H W, Jin C T and McEwan A. 2012. Electrode contact impedance sensitivity to variations in geometry. *Physiological Measurement,* **33** 817

Cole K S and Cole R H. 1941. Dispersion and Absorption in Dielectrics I. Alternating Current Characteristics. *J. Chem. Phys.,* **9** 341-51

deGroot-Hedlin C and Constable S. 1990. Occam's inversion to generate smooth, two-dimensional models from magnetotelluric data. *Geophysics,* **55** 1613-24

Felger H K and Bassewitz A. 1986. *Polyvinylchlorid,* (München: Hanser)

Flores Orozco A. 2012. Characterization of contaminated sites and monitoring of processes accompanying bioremediation using spectral induced polarization imaging. *PhD thesis*. *Rheinischen Friedrich-Wilhems-Universität Bonn*

Henke H. 2011. *Elektromagnetische Felder,* (Berlin/Heidelberg: Springer)

Hördt A, Blaschek R, Kemna A and Zisser N. 2007. Hydraulic conductivity estimation from induced polarisation data at the field scale — the Krauthausen case history. *J. Appl. Geophys.,* **62** 33-46

Jougnot D, Ghorbani A, Revil A, Leroy P and Cosenza P. 2010. Spectral induced polarization of partially saturated clay-rocks: a mechanistic approach. *Geophys. J. Int.,* **180** 210-24

Kaden H. 1959. *Wirbelströme und Schirmung in der Nachrichtentechnik,* (Berlin: Springer)

Karaoulis M, Revil A, Werkema D D, Minsley B J, Woodruff W F and Kemna A. 2011. Time-lapse three-dimensional inversion of complex conductivity data using an active time constrained (ATC) approach. *Geophys. J. Int.,* **187** 237-51

Kelter M, Huisman J A, Zimmermann E, Kemna A and Vereecken H. 2015. Quantitative imaging of spectral electrical properties of variably saturated soil columns. *J. Appl. Geophys.,* **123** 333-44

Kemna A. 2000. Tomographic inversion of complex resistivity. *PhD thesis*. *Ruhr-Universität Bochum*

Kemna A, Binley A, Cassiani G, Niederleithinger E, Revil A, Slater L, Williams K H, Orozco A F, Haegel F-H and Hoerdt A. 2012. An overview of the spectral induced polarization method for near-surface applications. *Near Surf. Geophys.,* **10** 453-68

Kemna A, Binley A, Ramirez A and Daily W. 2000. Complex resistivity tomography for environmental applications. *Chem. Eng. J.,* **77** 11 - 8

Kemna A, Binley A and Slater L. 2004. Crosshole IP imaging for engineering and environmental applications. *Geophysics,* **69** 97-107

Kemna A, Huisman J A, Zimmermann E and Fechner T. 2011. 4D Spectral Electrical Impedance Tomography. In: *GEOTECHNOLOGIEN Science Report,* (Potsdam: GEOTECHNOLOGIEN) pp 57-64

Kemna A, Kulessa B and Vereecken H. 2002. Imaging and characterisation of subsurface solute transport using electrical resistivity tomography (ERT) and equivalent transport models. *J. Hydrol.,* **267** 125-46

Kemna A, Münch H-M, Titov K, Zimmermann E and Vereecken H. 2005. Relation of SIP relaxation time of sands to salinity, grain size and hydraulic conductivity. *11th European Meeting of Environmental and Engineering Geophysics,*

Knödel K, Krummel H and Lange G. 2002. *Handbuch zur Erkundung des Untergrundes von Deponien und Altlasten,* (Berlin/Heidelberg: Springer)

Küpfmüller K E h, Mathis W and Reibiger A. 2008. *Theoretische Elektrotechnik,* (Berlin/Heidelberg: Springer)

Kwon Y W and Bang H. 1997. *The finite element method using MATLAB,* (Boca Raton: CRC Press)

Leroy P, Revil A, Kemna A, Cosenza P and Ghorbani A. 2008. Complex conductivity of water-saturated packs of glass beads. *J. Colloid Interface Sci.,* **321** 103-17

Lesmes D P and Frye K M. 2001. Influence of pore fluid chemistry on the complex conductivity and induced polarization responses of Berea sandstone. *Journal of Geophysical Research: Solid Earth (1978–2012),* **106** 4079-90

Macdonald D D and Urquidi-Macdonald M. 1990. Kramers-Kronig Transformation of Constant Phase Impedances. *J. Electrochem. Soc.,* **137** 515-7

Madden T R and Cantwell T. 1967. *Mining Geophysics,* (Tulsa, OK: Soc. Expl. Geophys.) pp 373-400

Müller K, Vanderborght J, Englert A, Kemna A, Huisman J A, Rings J and Vereecken H. 2010. Imaging and characterization of solute transport during two tracer tests in a shallow aquifer using electrical resistivity tomography and multilevel groundwater samplers. *Water Resour. Res.,* **46** W03502

Pelton W, Rijo L and Swift C. 1978. Inversion of two-dimensional resistivity and induced-polarization data. *Geophysics,* **43** 788-803

Persson P-O and Strang G. 2004. A Simple Mesh Generator in MATLAB. *SIAM Review,* **46** 329-45

Plaßmann W and Schulz D. 2009. *Handbuch Elektrotechnik,* (Wiesbaden: Vieweg Teubner GWV Fachverlage GmbH)

Schön J H. 1996. *Physical properties of rocks: fundamentals and principles of petrophysics*: Oxford, UK: Pergamon)

Slater L D. 2007. Near surface electrical characterization of hydraulic conductivity: From petrophysical properties to aquifer geometries—A review. *Surveys in Geophysics,* **28** 169-97

Slater L D and Lesmes D. 2002. IP interpretation in environmental investigations. *Geophysics,* **67** 77-88

Sunde E D. 1968. *Earth conduction effects in transmission systems,* (New York: Dover Publications)

Ulrich C and Slater L. 2004. Induced polarization measurements on unsaturated, unconsolidated sands. *Geophysics,* **69** 762-71

Vanhala H. 1997. Mapping oil-contaminated sand and till with the spectral induced polarization (SIP) method. *Geophys. Prospect.,* **45** 303-26

Vereecken H, Döring U, Hardelauf H, Jaekel U, Hashagen U, Neuendorf O, Schwarze H and Seidemann R. 2000. Analysis of solute transport in a heterogeneous aquifer: the Krauthausen field experiment. *J. Contam. Hydrol.,* **45** 329-58

Vilhunen T, Kaipio J, Vauhkonen P, Savolainen T and Vauhkonen M. 2002. Simultaneous reconstruction of electrode contact impedances and internal electrical properties: I. Theory. *Meas. Sci. Technol.,* **13** 1848

Vogel P. 2011. *Systemtheorie ohne Ballast Zeitdiskrete LTI-Systeme,* (Berlin/Heidelberg: Springer)

Wagner K. 1914. Dielektrische Eigenschaften von verschiedenen Isolierstoffen. *Archiv f. Elektrotechnik,* **3** 67-106

Wait J R. 1984. Electromagnetic response of a discretely grounded circuit. *Geophysics,* **49** 577-80

Ward S H and Fraser D C. 1963. *Conduction of electricity in rocks*: Institute of Engineering Research, University of California)

Ward S H and Hohmann G W. 1988. *Electromagnetic Methods in Applied Geophysics,* ed M N Nabighian (Tulsa: Society of Exploration Geophysicists) pp 131-311

Waxman M and Smits L. 1968. Electrical conductivities in oil-bearing shaly sands. *SPE,* 107-22

Wolfsperger H A. 2008. *Elektromagnetische Schirmung,* (Berlin/Heidelberg: Springer)

Wynn J C and Zonge K L. 1975. EM coupling, its intrinsic value, its removal and the cultural coupling problem. *Geophysics,* **40** 831-50

Wynn J C and Zonge K L. 1977. Electromagnetic coupling. *Geophys. Prospect.,* **25** 29-51

Zhao Y, Zimmermann E, Huisman J A, Treichel A, Wolters B, Waasen S v and Kemna A. 2013. Broadband EIT borehole measurements with high phase accuracy using numerical corrections of electromagnetic coupling effects. *Meas. Sci. Technol.,* **24** 085005

Zimmermann E. 2011. Phasengenaue Impedanzspektroskopie und -tomographie für geophysikalische Anwendungen. *PhD thesis*. *Rheinische Friedrich-Wilhelms-Universität Bonn*

Zimmermann E, Huisman J A, Kemna A, Berwix J, Glaas W, Meier H, Wolters B and Esser O. 2010. Advanced electrical impedance tomography system with high phase accuracy. *6th World Congress on Industrial Process Tomography (WCIPT6), Beijing,* 583-91

Zimmermann E, Kemna A, Berwix J, Glaas W, Münch H M and Huisman J A. 2008b. A high-accuracy impedance spectrometer for measuring sediments with low polarizability. *Meas. Sci. Technol.,* **19** 105603

Zimmermann E, Kemna A, Berwix J, Glaas W and Vereecken H. 2008. EIT measurement system with high phase accuracy for the imaging of spectral induced polarization properties of soils and sediments. *Meas. Sci. Technol.,* **19** 094010

Zonge K L and Wynn J C. 1975. Recent advances and applications in complex resistivity measurements. *Geophysics,* **40** 851-64